



Available online at www.sciencedirect.com



Progress in Aerospace Sciences 43 (2007) 65–137

PROGRESS IN
AEROSPACE
SCIENCES

www.elsevier.com/locate/paerosci

Non-linear aeroelastic prediction for aircraft applications

M.J. de C. Henshaw^{a,*}, K.J. Badcock^b, G.A. Vio^c, C.B. Allen^d,
J. Chamberlain^e, I. Kaynes^f, G. Dimitriadis^c, J.E. Cooper^c, M.A. Woodgate^b,
A.M. Rampurawala^b, D. Jones^d, C. Fenwick^d, A.L. Gaitonde^d, N.V. Taylor^d,
D.S. Amor^a, T.A. Eccles^a, C.J. Denley^a

^aBAE SYSTEMS, Saltgounds Rd, Brough, E. Yorks HU15 1EQ, UK

^bCFD Laboratory, FST Group, Department of Engineering, Liverpool University, Liverpool L69 3GH, UK

^cSchool of Mechanical, Aerospace and Civil Engineering, The University of Manchester, Oxford Road, Manchester M13 9PL, UK

^dDepartment of Aerospace Engineering, University of Bristol, Bristol, BS8 1TR, UK

^eAIRBUS UK, Filton, Bristol, BS99 7AR, UK

^fQinetiQ, Cody Technology Park, Ively Road, Farnborough, Hampshire, GU14 0LX, UK

Available online 14 August 2007

Abstract

Current industrial practice for the prediction and analysis of flutter relies heavily on linear methods and this has led to overly conservative design and envelope restrictions for aircraft. Although the methods have served the industry well, it is clear that for a number of reasons the inclusion of non-linearity in the mathematical and computational aeroelastic prediction tools is highly desirable. The increase in available and affordable computational resources, together with major advances in algorithms, mean that non-linear aeroelastic tools are now viable within the aircraft design and qualification environment. The Partnership for Unsteady Methods in Aerodynamics (PUMA) Defence and Aerospace Research Partnership (DARP) was sponsored in 2002 to conduct research into non-linear aeroelastic prediction methods and an academic, industry, and government consortium collaborated to address the following objectives:

- (1) To develop useable methodologies to model and predict non-linear aeroelastic behaviour of complete aircraft.
- (2) To evaluate the methodologies on real aircraft problems.
- (3) To investigate the effect of non-linearities on aeroelastic behaviour and to determine which have the greatest effect on the flutter qualification process.

These aims have been very effectively met during the course of the programme and the research outputs include:

- (a) New methods available to industry for use in the flutter prediction process, together with the appropriate coaching of industry engineers.
- (b) Interesting results in both linear and non-linear aeroelastics, with comprehensive comparison of methods and approaches for challenging problems.
- (c) Additional embryonic techniques that, with further research, will further improve aeroelastics capability.

*Corresponding author. Department of Aeronautical and Automotive Engineering, Loughborough University, LE11 3TU, UK.
Tel.: +44 1509227214; fax: +44 1509227275.

E-mail address: M.J.d.Henshaw@lboro.ac.uk (M.J. de C. Henshaw).

This paper describes the methods that have been developed and how they are deployable within the industrial environment. We present a thorough review of the PUMA aeroelastics programme together with a comprehensive review of the relevant research in this domain. This is set within the context of a generic industrial process and the requirements of UK and US aeroelastic qualification. A range of test cases, from simple small DOF cases to full aircraft, have been used to evaluate and validate the non-linear methods developed and to make comparison with the linear methods in everyday use. These have focused mainly on aerodynamic non-linearity, although some results for structural non-linearity are also presented. The challenges associated with time domain (coupled computational fluid dynamics–computational structural model (CFD–CSM)) methods have been addressed through the development of grid movement, fluid–structure coupling, and control surface movement technologies. Conclusions regarding the accuracy and computational cost of these are presented. The computational cost of time-domain methods, despite substantial improvements in efficiency, remains high. However, significant advances have been made in reduced order methods, that allow non-linear behaviour to be modelled, but at a cost comparable with that of the regular linear methods. Of particular note is a method based on Hopf bifurcation that has reached an appropriate maturity for deployment on real aircraft configurations, though only limited results are presented herein. Results are also presented for dynamically linearised CFD approaches that hold out the possibility of non-linear results at a fraction of the cost of time coupled CFD–CSM methods. Local linearisation approaches (higher order harmonic balance and continuation method) are also presented; these have the advantage that no prior assumption of the nature of the aeroelastic instability is required, but currently these methods are limited to low DOF problems and it is thought that these will not reach a level of maturity appropriate to real aircraft problems for some years to come. Nevertheless, guidance on the most likely approaches has been derived and this forms the basis for ongoing research. It is important to recognise that the aeroelastic design and qualification requires a variety of methods applicable at different stages of the process. The methods reported herein are mapped to the process, so that their applicability and complementarity may be understood. Overall, the programme has provided a suite of methods that allow realistic consideration of non-linearity in the aeroelastic design and qualification of aircraft. Deployment of these methods is underway in the industrial environment, but full realisation of the benefit of these approaches will require appropriate engagement with the standards community so that safety standards may take proper account of the inclusion of non-linearity.

© 2007 Elsevier Ltd. All rights reserved.

Contents

1. Introduction	67
1.1. Overview	67
1.2. The need for non-linear aeroelastic methods	69
1.3. Programme logic diagram and plan of paper	71
2. Review of aeroelastic prediction and qualification.	73
2.1. Current status of industrial aeroelastic prediction	74
2.1.1. Stage 1	74
2.1.2. Stage 2	75
2.1.3. Stage 3	75
2.2. Aeroelastic qualification	75
2.3. Review of current research into aeroelastics and aeroservoelastic prediction	77
2.3.1. Brief historical overview of linear flutter analysis	77
2.3.2. Building blocks for linear analysis	77
2.3.3. Non-linear mechanisms	78
2.3.4. Examples of sources of nonlinearities	78
2.3.5. Examples of observed non-linear behaviour	78
2.3.6. Store induced LCO	79
2.3.7. Computational aerodynamics	79
2.3.8. Model reduction	80
3. Test cases	81
4. Time-domain CFD based methods	82
4.1. Overview	82
4.1.1. Physical coupling	83
4.2. Fluid–structure coupling for aeroelastic modelling	85
4.3. Moving grid methods for unsteady CFD.	88
4.3.1. Introduction	88

4.4.	Initial validation: AGARD 445.6 flutter boundary	89
4.4.1.	Comparison with commercial linear/non-linear methods	89
4.5.	Treatment of control surfaces	91
4.5.1.	Introduction	91
4.5.2.	Blended treatment	91
4.5.3.	SST	92
4.5.4.	Sliding mesh treatment	95
4.5.5.	BACT wing	98
4.5.6.	Conclusions	99
5.	Fast flutter prediction—prediction methods for non-linear aeroelasticity	101
5.1.	Overview	101
5.2.	Dynamically linearised CFD approaches—ROMSI	101
5.2.1.	Introduction	101
5.2.2.	State-space models of the CFD code	102
5.2.3.	System reduction	103
5.2.4.	Practical procedure for generating ROMSI for aeroelastic applications	103
5.2.5.	Three-dimensional test case: the AGARD 445.6 wing	103
5.3.	Hopf bifurcation based methods	104
5.3.1.	Hopf bifurcation calculation for symmetric problems	105
5.3.2.	Shifted inverse power method	106
5.3.3.	Response from reduced order method	106
5.3.4.	AGARD 445.6 wing	107
5.4.	Local linearisation approaches	107
5.4.1.	Higher order harmonic balance	109
5.4.2.	Numerical continuation	109
5.4.3.	The BAH aeroelastic wing model	110
5.4.4.	Results	112
6.	Application of technologies	115
6.1.	Goland wing	115
6.1.1.	Introduction	115
6.1.2.	Time-domain results	115
6.1.3.	Signal processing and parameter estimation	116
6.2.	Hawk	119
6.2.1.	Overview	119
6.2.2.	Linear analysis	120
6.2.3.	CFD grids	121
6.2.4.	Wing and wing–body–tail configurations	121
6.2.5.	Combat flap	122
6.2.6.	Rudder buzz	126
6.2.7.	Perspective	127
6.3.	MDO analysis	127
6.3.1.	Time-domain methods	127
6.3.2.	Fast flutter methods for the MDO civil aircraft wing	129
7.	Summary and general conclusions	130
	Acknowledgments	132
	References	132

1. Introduction

1.1. Overview

Dynamic aeroelastic effects result from the interaction of the aerodynamic, elastic, and inertial forces to which aircraft are subject; their careful

consideration is required throughout the design activity and as a safety-critical factor in the qualification of aircraft into service. In general, the interaction of the control system with aeroelasticity (termed aeroservoelasticity) must also be considered. Accurate prediction of this phenomenon is complex, but the undesirable effects of aeroelasticity

Nomenclature	
<i>Abbreviations</i>	
BACT wing	Benchmark Active Controls Technology wing (test case)
BAH wing	Bisplinghoff, Ashley and Halfman wing (test case)
CFD	computational fluid dynamics
CSM	computational structural model
CVT	constant volume tetrahedra
DARP	Defence and Aerospace Research Partnership
DES	detached eddy simulation
DTI	Department of Trade and Industry
EPSRC	Engineering and Physical Sciences Research Council
ERA	Eigensystem Realisation Algorithm
FCS	flight control system
FE	finite element
FEM	finite element model
GLA	Generic Large Aircraft (test case)
GVT	ground vibration test
HOHB	higher order harmonic balance
HOPF	the name of a computer code that uses Hopf bifurcation approach
MDO wing	multi-disciplinary optimisation wing (test case)
MoD	Ministry of Defence
PMB	Parallel MultiBlock (the name of an Euler/Navier–Stokes CFD code)
POD	proper orthogonal decomposition
PUMA	Partnership for Unsteady Methods in Aerodynamics
RANSMB	Reynolds averaged Navier–Stokes MultiBlock (the name of a CFD code)
ROM	reduced order model
ROMSI	reduced order model system identification (name of a computer code)
SST	supersonic transport (test case)
STFT	short time Fourier transform
TFI	transfinite interpolation
TPS	thin plate spline
TSD	transonic small disturbance
UKAA	United Kingdom Applied Aerodynamics

include airframe fatigue, loss of control, unacceptable vibration (for passengers or crew, and for weapon aiming in the case of military aircraft), or even complete destruction of the aircraft itself. From the earliest reports of flutter [1], during World War I, there was significant effort to understand and predict aeroelastic effects and the number of incidents has steadily declined over the years. For instance, the number of incidents declined from 146 in the period 1933–1945 to seven between 1960 and 1972 [2]. Flutter incidents are now rare, but this should not be understood to mean that the problem of flutter has been solved, and certainly the general problems of aeroelasticity place unwanted constraints on aircraft design. Indeed, with recent advances in materials and structures, engineers are now endeavouring to use aeroelasticity in a positive way to achieve more capable designs.

The fidelity, accuracy, and range of applicability of everyday computational prediction methods for aeroelasticity are significantly limited because they assume a linear system. Linearity has been imposed by affordability constraints (financial cost and time) that preclude the use of more sophisticated models from the general aeroelastics design and qualification process. To some extent, appropriate mathe-

matical techniques to achieve solutions of greater integrity have also been lacking.

During the 1990s advances in computational methods and available computational power raised expectations that more ambitious aeroelastic calculations would be feasible and a number of projects sought to develop methods to take advantage of these possibilities [3,4]. The work reported herein builds on those efforts to provide realisable non-linear aeroelastic techniques for routine use.

The Partnership for Unsteady Methods in Aerodynamics (PUMA) Defence and Aerospace Research Partnership (DARP) was formed in 1999 and is a collaboration led by industry with academia and government to engage in industrially focused research in the defence and aerospace domain. DARP grew out of the UK Department of Trade and Industry (DTI) foresight activities and PUMA was accredited in the first round to cover research in unsteady aerodynamics for fixed wing aircraft and turbomachinery applications. In 2002, with sponsorship from Ministry of Defence (MoD), DTI, Engineering and Physical Sciences Research Council (EPSRC) and industry, a collaborative research programme was launched with academics from seven universities. There were two focus groups, one working on large eddy simulation (LES)

methods for turbomachinery applications and another on non-linear aeroelastics for fixed wing aircraft. This latter group comprised BAE Systems, Airbus, and QinetiQ, with the Universities of Bristol, Glasgow, and Manchester. Six fulltime academic researchers were assigned to this group to carry out research into the modelling and prediction of non-linear aeroelastic phenomena, with the following aims:

- (1) To develop useable methodologies to model and predict non-linear aeroelastic behaviour of complete aircraft.
- (2) To evaluate the methodologies on real aircraft problems.
- (3) To investigate the effect of non-linearities on aeroelastic behaviour and to determine which have the greatest effect on the flutter qualification process.

These aims have been very effectively met during the course of the programme and the research outputs include:

- (1) New methods available to industry for use in the flutter prediction process, together with the appropriate coaching of industry engineers.
- (2) Interesting results in both linear and non-linear aeroelastics, with comprehensive comparison of methods and approaches for challenging problems.
- (3) Additional embryonic techniques that, with further research, will further improve aeroelastics capability.

Although the work began with the challenge of non-linear flutter prediction, it has expanded (according to plan) to include other aeroelastic phenomena such as limit cycle oscillation (LCO), flutter suppression through control laws, forced large amplitude pitching and rolling, and initial results on buffeting prediction. Furthermore, a variety of methods of varying fidelity and commensurate affordability have been developed, which range from fully coupled fluid–structure calculations (based on sophisticated computational fluid dynamics (CFD) with moving control surfaces) to ROMs for rapid prediction. An important output has been the construction of a database of relevant test cases that includes real aircraft cases, and a set of studies that compare approaches for accurate and affordable predictions thereof. Access to high

performance computers through the United Kingdom Applied Aerodynamics (UKAA) consortium, sponsored by EPSRC, has been a vital component in the success of this project. Several of the results are first achievements of such calculations, these are described and the more detailed landmark papers are, of course, referenced.

This paper provides a summary of the entire aeroelastics project that includes the essential details of the methods and approaches that have been used, a selection of important results, and information about the exploitation of the methods for practical industrial application. We begin by setting the scene in terms of the status of industrial practice at the beginning of this decade, and the industrial imperative for affordable non-linear aeroelastics capabilities. The background includes a description of the current qualification requirements and those that are anticipated in the future. Following a review of the current status of aeroelastic and aeroservoelastic research, the test case database and computational methods are described. The validation and comparisons of these methods for both linear and non-linear cases are reported and the application of certain of these to full aircraft problems is detailed. Finally, the manner in which the research outputs are being exploited by industry is recorded.

1.2. The need for non-linear aeroelastic methods

Aeroelasticity is the science that concerns the interaction of aerodynamic, elastic and inertial forces [5,6] and the resulting phenomena. Static aeroelasticity effects result from the interaction of aerodynamic and inertial forces, however, all three forces are required to interact in order for dynamic aeroelastic effects to occur.

As the most important aeroelastic phenomena, e.g. flutter and divergence, can potentially lead to structural failure, aircraft structural designs have had to be made heavier (the so-called aeroelastic penalty) in order to ensure that structural integrity has been maintained via changes in the structural stiffness or position of the mass and flexural axes. Excellent histories about the development of aeroelasticity and its influence on aircraft design can be found in the review articles [7,8], with surveys of more recent applications given by Friedmann [9], Bhatia [10] and Livne [11].

Bisplinghoff et al. [5] classically define the range of aeroelastic phenomena through their aeroelastic

triangle of forces [5, Fig. 1]. Although these are amenable to linear analysis and empirical prediction methods, the phenomena are all subject to non-linearity to a greater or lesser extent. Non-linearity may arise through a variety of mechanisms, associated with aerodynamic, structural, or control system causes. In transonic flow conditions, aerodynamic non-linearity can occur due to the movement of shockwaves. Structural non-linearity can be caused by cubic stiffness, such as in engine pylon/wing interface; freeplay, of hinged surfaces such as wing and flap; and geometric non-linearities that are a result of large deflections. Control systems are also possible causes of aeroelastic non-linearities due to time delays, rate limits, or non-linear control laws. It is generally true that non-linearity has been accommodated within linear analysis methods by using conservative safety margins in design; this implies heavier and stiffer aircraft designed to ensure against aeroelastic failure and in some cases places limits on the flight envelope to avoid potentially dangerous conditions. The latter is especially true of combat aircraft susceptible to buffet.

This programme has been mainly concerned with the prediction of flutter and LCO, which are related phenomena. Flutter is usually considered to be a violent unstable vibration, the origin of which is usually traceable to the coupling of two vibration modes in the aeroelastic system. LCO is then described as a bounded flutter. For many, but not all, conditions then, the onset of flutter can be predicted using linear techniques, but the prediction of LCO—and indeed the assessment of whether a flutter occurrence will stabilise as an LCO—always requires consideration of non-linearity. It is worth noting that another school of thought (e.g. [12]) considers all LCO and flutters to be bifurcations and that flutter is, in fact, an unstable LCO. Some non-linear prediction methods make *a priori* assumptions about the cause—i.e. one of the mechanisms noted above—and are constructed to search for those particular instability mechanisms, whereas other methods make no prior assumptions about the cause. The methods described herein are classified in this way, and some interesting contrasts can be drawn. Unsurprisingly, at this time, the methods that make a prior assumption are at a much high level of readiness for industrial deployment.

The general decline in flutter incidents, over the last 25 year, has been taken, in some quarters, to imply that flutter has been solved. This view is over-

optimistic and dangerously complacent for a number of reasons [13].

- (1) Flutter calculations are not highly accurate. Adequacy currently implies that calculations plus the regulatory margin have resulted in a safe aircraft; there is no indication of the true accuracy achieved.
- (2) Lighter and more structurally efficient designs are now being achieved through structural optimisation; the reduced stiffness that results increases the likelihood of encountering flutter limitations.
- (3) Increased authority and bandwidth of flight control system (FCS) increases the risk of undesirable aeroservoelastic effects. Active flight controls, with variable or adaptive gains will disperse critical cases more widely over the flight envelope, instead of them being concentrated in the classic high dynamic pressure, or transonic Mach number, parts of the envelope.
- (4) In-service enhancements for FCS may change the flutter clearance or loading actions during the life of the aircraft. It should be noted that this is likely and represents a significant through-life cost for aircraft that are expected to remain in-service for many years.
- (5) Partly driven by low-observability requirements, future vehicles may have novel configurations for which read-across data are non-existent.
- (6) Other forward-looking reasons for improving aeroelastic prediction include:
 - (a) Dynamic loads may become more significant because structural optimisation tends to spread the range of critical loading actions.
 - (b) More integrated approaches to design will require greater fidelity and accuracy of structural models.
 - (c) Anticipated use of aeroelastics in positive ways (for control, drag reduction, etc.) will require significantly improved prediction capabilities.

There are, thus, many reasons why more sophisticated aeroelastic modelling and prediction will be required for future applications. However, it is also worthwhile considering the risks and compromises enforced by the present use of linear methods.

The linear approximation for flutter prediction holds good in subsonic and supersonic flow and appropriate linear methods may be used to predict the aerodynamic forces to couple with the structural

model and hence derive the aeroelastic behaviour. In the transonic region, the highly non-linear behaviour causes small changes in aerodynamic configuration to generate large changes in the forces and moments. Linear prediction is, then, entirely inadequate. But this inadequacy is compounded by the relative increase in likelihood of flutter occurring in this region. Ashley [14] has noted that the phase lag in the shock motion for this type of flow causes a lowering of the flutter speed; the so-called transonic dip. Thus, the region of the envelope at which there is greatest risk of flutter occurrence is also that in which our predictive capability is weakest. This leads to expensive flight test programmes, in which risks must be minimised by taking very small parameter steps in the expansion of the envelope through the transonic regime. Development of an affordable method for predicting transonic flutter was the initial motivation for this research activity (and for several similar initiatives). Other phenomena, such as LCO, backlash and buffet are intrinsically non-linear (aerodynamic, structural, or both) in their nature and linear methods are clearly inadequate.

It is clear, then, that inability to predict or model non-linear aeroelastic (or aeroservoelastic) behaviour is resolved by extensive flight test programmes, informed through experimental, empirical, or simplified modelling, techniques. This is an expensive approach to qualification and has the major disadvantage that should an aeroelastic susceptibility be identified, redesign must take place late in the development cycle; again this can be (and usually is) extremely costly. New approaches to aeroelastic modelling and prediction that account accurately for non-linearity are needed to reduce the costs and risks of current processes. This is true, not just for new designs, but also for existing aircraft that may go through several major upgrades (and in the case of military aircraft be fitted with new weapons) when re-certification is required. Furthermore, advances in other technologies mean that in the future, non-linearity may be more prevalent in designs. The need for non-linear aeroelastics is clearly established.

1.3. Programme logic diagram and plan of paper

Fig. 1 is a logic diagram for the aeroelastics research programme and also provides a map for this paper. Reading from left to right, the diagram shows the causes of non-linearity that have been

considered and the test cases that exhibit such phenomena. The methods developed within PUMA are then listed and the cases to which they have been applied are identified. The methods are classified by type. Section numbers make the layout of the paper clear. The aeroelastic phenomena considered here are flutter and LCO (see Section 4); ‘other*’ refers to aeroelastic phenomena where no *a priori* assumption is made about the instability type, or simply to other types of aeroelastic events (e.g. buffet, gust, etc.) that may or may not be amenable to the techniques reported herein (see Section 1.2), but are not discussed further in this paper.

As noted in Section 1.2, non-linearity may occur due to the aerodynamics, structural, or control systems causes. In fact, this programme has focused predominantly on aerodynamic non-linearity, but the importance of structural and control systems non-linearity should not be underestimated and further work remains to build these considerations into the methods presented. At the end of the paper, we shall consider the extent to which the requirements implied by the six reasons, given in Section 1.2, for needing non-linear capability have been met by this research.

The three aims of the programme stated in Section 1.1 can be paraphrased as a need for usable methods to predict non-linear phenomena, which in turn implies that evaluation of appropriateness (i.e. for realistic aircraft problems) must be conducted, and the capability to investigate and understand non-linearity when it arises.

A set of test cases exhibiting the phenomena against which the methods must be evaluated, and of varying levels of complexity up to full aircraft has been assembled (Section 3).

Against the challenges identified in the sections referred to above a number of solution methods or approaches are proposed. Existing methods or tools in industrial use (Section 2.1) are either linear, or linear with a non-linear correction applied in some way. The performance of these methods for non-linear problems is of interest both for comparison with new methods and to understand the risks that arise with their use. The three tools considered here (MSC.NASTRAN, ZAERO, and ZTAIC) are briefly described in Section 4.4.1. New approaches we have termed ‘research methods’ or the building blocks thereof; these are reviewed in Section 2.3, together with approaches to analysis that are necessary to identify and understand non-linear phenomena. The review of research methods is not intended to be

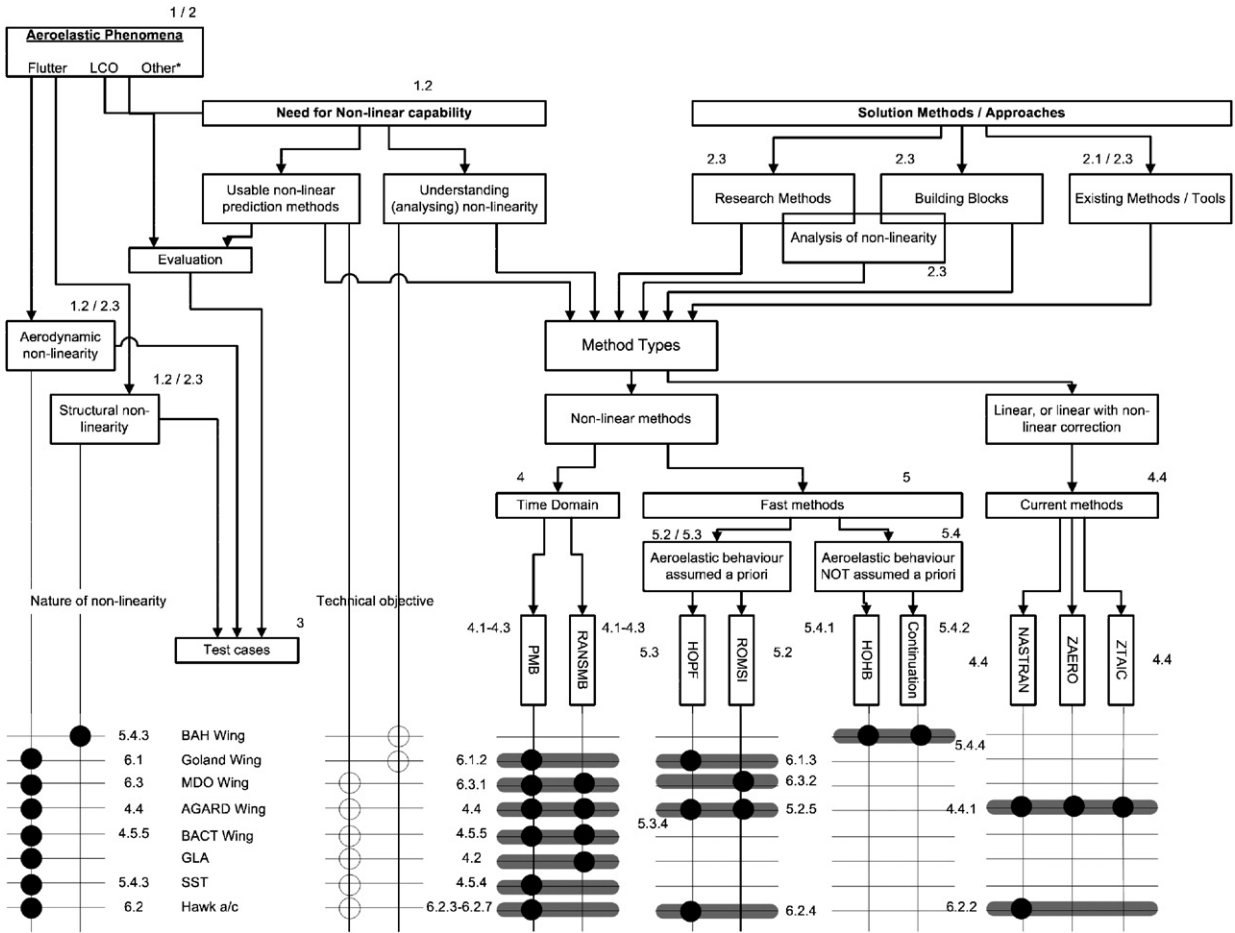


Fig. 1. Programme logic diagram.

exhaustive, but rather to set this research programme within the context of activity in this field.

Two broad approaches to non-linear prediction are considered. The first is modelling in the time domain, which is based on the coupling of CFD to a computational structural model (CSM); this is covered in Section 4. The approach uses the fluid dynamics model to calculate the aerodynamic loads, and then uses the structural model to determine the mechanical response of the vehicle. Through an iterative procedure the aeroelastic response can be determined over time. There are four principal technical challenges associated with these methods:

(1) Adequate coupling between the CFD and CSM.

The transformation method must maintain an accurate shape during aeroelastic deformation; the difficulties in achieving this, and the PUMA

solution methods that address these are discussed in Section 4.2.

- (2) As the aircraft deforms, the CFD field grid, in which the flow is calculated, must be moved in such a way that the grid quality is maintained and the movement is achieved in a computationally efficient manner. Section 4.3 presents grid movement methods for the structured, multiblock grids used in this work.
- (3) Of particular concern is the management of the grid for cases involving control surface movement; various grid strategies have been formulated and tested and these are presented in Section 4.4.
- (4) Finally, it is important to understand the practicalities of implementing an effective time-domain method. The work in this programme has employed structured, multiblock grids but the generalisability of the techniques to unstructured

or hybrid grids is discussed in Section 6.2.7, as this impacts the ability to profit from the most recent advances in grid generation [15], and hence exploitability.

Despite the significant advances in time-domain methods in PUMA and elsewhere, these methods are still at least two orders of magnitude too slow for routine use for flutter qualification purposes. They do, however, provide cost-effective tools for examination of critical or unexpected cases at conditions identified by other means.

The essential features of the two coupled codes (Parallel MultiBlock (PMB) and Reynolds averaged Navier–Stokes MultiBlock (RANSMB)) that have been used in this work are outlined in Section 4.1. Both codes have been extensively reported elsewhere as referenced in the relevant sections. To address the need for rapid non-linear aeroelastic prediction, so-called fast flutter methods (Section 5) have been developed. These are generally based on some process of model reduction. The challenge is to develop methods that work at a comparable calculation speed to industry standard methods (e.g. doublet lattice), but are capable of predicting transonic, and other non-linear, aeroelastics. We have divided these fast methods into two classes:

- those in which assumptions about the type of aeroelastic behaviour are made in advance and where a single bifurcation is expected (Section 5.2 and (27)), and
- those in which no prior knowledge of the instability is assumed (Section 5.4).

In principle, the first class is more akin to current working practice, where a specific aeroelastic event is sought, whereas the second class should be more generalisable.

For the methods in which the aeroelastic behaviour is assumed in advance, a steady flow CFD solution provides the starting point for a more rapidly executed stability analysis. A system reduction method has been applied to the Euler equations to provide a reduced order model (ROM) from which the stability behaviour is deduced; this is the reduced order model system identification (ROMSI) code (Section 5.2). The HOPF code (27) uses a steady CFD solution from which a Hopf bifurcation is identified to generate the stability boundary; from this a model reduction procedure allows the nature of the instability to be explored.

These approaches have been tested on realistic problems and, in the case of the Hopf method an industrial wing geometry has been calculated. Relatively large systems can be calculated with these methods, so that they could be deployed for full aircraft configurations. The methods for which no prior assumption of instability type is made are at a much lower level of maturity. So far only relatively simple systems (i.e. a small number of degrees of freedom) have been possible, and there remains a significant challenge in developing them for complex systems of industrial relevance.

For convenience, Fig. 1 indicates which test cases have been used for each method and the sections in which the results appear. The nature of the non-linearity (aerodynamic or structural) and the technical objective (prediction method or analysis of non-linearity) that has been addressed in this paper are indicated.

The selection of results provided in Sections 4 and 5 are ‘method development’ evaluations supporting the development and maturation of the tools. Section 6 considers the application of technologies and provides an indication of the usability of the methods for the industrial context. The conclusions of Section 7, thus, include an analysis of the industrial exploitation, a summary of the major advances made during the programme, and a perspective of future work and anticipated advances. It is a mark of the effectiveness of the industry-academic collaboration that some of the research outputs have been rapidly deployed within industry.

In summary, Section 1 provides the research challenge and Section 2 sets the industrial and research context. Section 3 summarises the test cases that have been used to exercise research responses to the challenge. Section 4 covers time-domain methods, and Section 5 the fast flutter/LCO prediction methods. Section 6 considers the applicability of the more mature non-linear methods to real industrial requirements and Section 7 draws some conclusions.

2. Review of aeroelastic prediction and qualification

In this section we first review current industrial practice and the requirements and processes for aeroelastic qualification and then briefly review current research in order to establish the context for the PUMA research and how it will enhance industrial aeroelastic prediction capability.

2.1. Current status of industrial aeroelastic prediction

The major challenge faced by industry in aeroelastic design and qualification of aircraft is the sheer number of load cases that must be considered [3]. Thousands of cases must be calculated, and for combat aircraft this number is multiplied by the number of possible store configurations. The specific processes used by industry to qualify an aircraft against flutter vary from one organisation to another, often because of differences in the specific toolsets that are employed. It is, however, helpful to consider a generic flutter qualification process (Fig. 2) to indicate the constraints, costs and bottlenecks that may be encountered and the opportunities to improve certain features. In the conclusions we shall refer to the process again to show where the tools developed within PUMA may be deployed.

There are three basic stages to the process, representing improved data at each stage and a commensurate increase in confidence of the predicted flutter solution.

2.1.1. Stage 1

From the initial design an aerodynamic model of the aircraft is available; for flutter calculations this

will generally be a vortex lattice model (or similar) [11]; whilst these have restricted range of applicability (subsonic flow), they allow rapid computation of many flight conditions. For supersonic flow, methods such as Mach box [5] might be employed. From the aerodynamic model a set of aerodynamic influence coefficients (AICs) are obtained [13]. The design process will have included some aerodynamic modelling (CFD or wind tunnel) and so aerodynamic data are available. The design will also provide mass data and this will be combined with an appropriately constructed finite element model (FEM) to provide a set of structural vibration modes that describe the structural behaviour of the airframe. The aerodynamics and the structural models are integrated through a computational procedure to provide a flutter solution, which is basically a stability boundary of aircraft speed as a function of either Mach number or altitude. Stability is determined as the point at which the amplitude of a structural vibration mode (more usually two or more modes) diverges. Clearly the generation of such a stability boundary requires a significant number of individual calculations (a Mach number sweep) and it is this volume of computation that has mainly driven the limitation of the techniques to simple methods in order to meet design process timescales. In this first stage, the

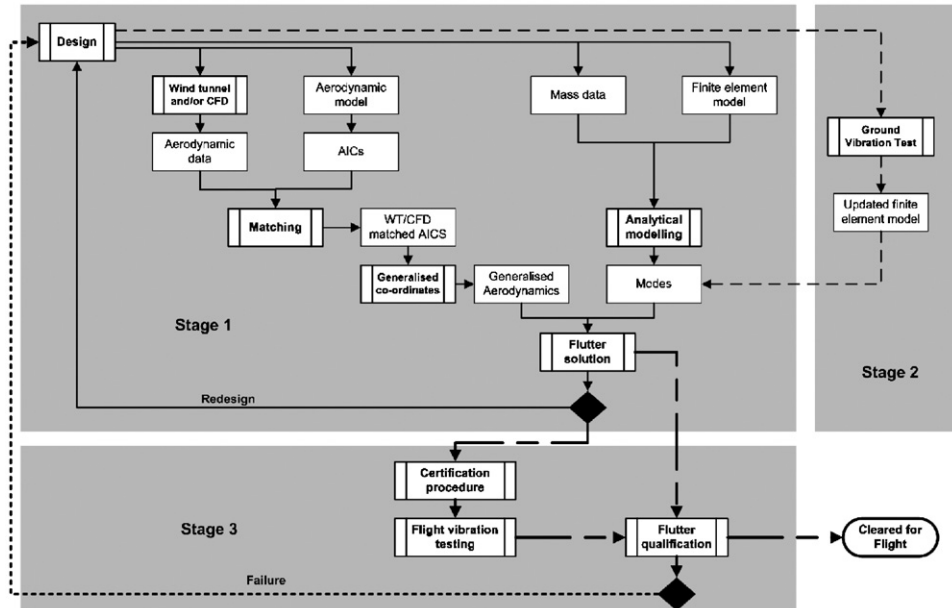


Fig. 2. Generic flutter qualification process.

results may lead to redesign (as shown) and the generation of the flutter solution occurs within an iterative design cycle, although clearly the cost of subsequent cycles is much less than the first, as most data are reusable. To be clear: the objective of the design exercise, from a flutter perspective, is to ensure that the critical speed at which flutter occurs lies outside of the operational flight envelope for the aircraft. In fact, as explained below, a safety margin of 15% is allowed to accommodate possible errors in the computed predictions.

At one time the flutter solution would be derived at unmatched conditions; for example, the Mach sweep might be conducted at a single air density condition (usually sea level), so that the Mach number and air speed at which the boundary was predicted would not necessarily correspond to a physically realisable condition. Nevertheless, if the flutter speed were sufficiently distant from operational speeds this inaccuracy was not considered very important. The cost of improving the accuracy, given the limitations of computer power, was too great to make more accurate reckoning worthwhile. Nowadays, the availability of cheap, fast computers makes it feasible to carry out matching, in which the conditions are matched using a larger data set, so that the flutter speed may be calculated more accurately. It is also common to match against frequency as well (see Sections 2.3.1 and 2.3.2 for further details).

2.1.2. Stage 2

Once the design has reached the point that a vehicle can be built, then the structural model is improved through more accurate definition of the modes from ground vibration test (GVT) data. A soft-support system is used to simulate the aircraft in flight and actuators of some type provide defined structural excitation. The structural response is measured, usually with accelerometers, and from this the models may be validated and improved. Thus an improved flutter solution may be obtained, though it is recognised that the models are still relatively simple and that there will always be some disparity between the structural behaviour in flight and the GVT. Design changes in response to the new calculations are still possible, but the scope for change is much more limited. GVT is also used to investigate unexpected events that may arise during flight testing.

2.1.3. Stage 3

In the certification procedure a flight test plan is drawn up that is informed by the flutter predictions of the previous stage. The aircraft must be flown throughout its envelope in all possible configurations (for instance, military aircraft must be cleared for flight for each new stores configuration that is introduced). In practice, this means incrementally exploring the flight envelope and the strategy for doing so, including the size of the increments and how the most risky conditions are approached, are determined from the data from stage 2. Any unexpected results at this stage, requiring design modification, can be very costly indeed.

2.2. Aeroelastic qualification

Any military or civil aircraft must meet the aeroelastic elements of the requirements against which the aircraft is qualified. UK military aircraft are designed to meet DEF STAN 00-970 requirements [16], while American military specifications Mil-Spec [17] are often used for international collaborative military projects. Civil aircraft are designed to meet JAA/EASA [18] and/or FAA requirements [19]. These requirements have a common top level objective: to ensure that the aircraft shall be free from flutter and other aeroelastic instabilities throughout the flight envelope.

For aeroelastic clearance the flight envelope is bounded by the design dive speed V_D and Mach number M_D . To ensure freedom from flutter within the flight envelope, the concept of the flutter margin has been introduced; the usual requirement of this being that no flutter must exist within the flight envelope expanded by 15% on V_D and on M_D . Dynamic pressure is often the key variable in linear flutter characteristics and it should be noted that the 15% margin on airspeed corresponds to a 32% margin on dynamic pressure.

The concept of the flutter margin has served the community well in providing a reasonable margin of flutter safety. The factors which are addressed within the concept of the flutter margin include:

- (a) Variability between individual aircraft build standard, specifically differences between the aircraft on which flutter testing was carried out and other aircraft. This may include small design differences, build variations resulting in structural differences such as mass, stiffness, or

- damping variations, control surface backlash variation, or even geometrical differences.
- (b) Mass differences from the test conditions, in particular the possibility that there exists a mass distribution which was not tested but which has worse flutter characteristics.
 - (c) Variation of structural properties with aircraft age. This may include reductions in stiffness of the structure or control systems, increased backlash, reduction of structural damping, or increased non-linearity on older airframes.
 - (d) Other inaccuracies or inconsistencies of modelling or testing which may have resulted in the flight flutter test missing the most critical flutter condition.

One factor which is not addressed directly by the flutter margin is the possibility of excessively high speed during flight, such as might result from pilot error, gusts, or instrument or control system failure. These possibilities should be covered by the imposition of the service limiting speed, V_L , in DEFSTAN, or the design cruise speed V_C in civil requirements. These limits on normal operation should be set such that exceeding these speeds by the amount necessary to reach V_D should be a remote probability.

There is some similarity between flutter margins and the structural load qualification levels. Limit load is set at a level which is expected to be experienced as a remote probability, maybe of the order of once in an aircraft lifetime. Ultimate load is a factor of 1.4 or 1.5 times limit load and the structure must be capable of withstanding this load without failure, although distortion and damage are allowed. Thus ultimate load is greater than any foreseen loading action in the same way that the flutter margin results in speeds greater than any expected to be experienced in flight. Both concepts have a degree of assumption of linearity in the expansion of properties outside the regular flight envelope.

The overall qualification process starts with the need for the clearance authorities to be satisfied with the analysis and ground testing which have been undertaken in stages 1 and 2 described in Section 1.1. Additional relevant qualification testing must also be conducted which has a bearing on aero-servoelastic clearance, including such tests as control circuit stiffness measurements and the structural coupling test. All authorities then require flight demonstration of the flutter characteristics of

the aircraft in flight. In fact the exploration of flutter is usually a key element in the envelope expansion phase of a flight test programme.

The clearance for first flight is usually within a limited flight envelope. For a derivative design the initial envelope will be based on considerations of the differences from the original aircraft, with particular regard to the aeroelastic sensitivities of the original aircraft and the likelihood of different aeroelastic characteristics. For a completely new design, the initial flight speed is normally specified as half the design dive speed or half the calculated flutter speed, whichever is the lowest.

The envelope will then be expanded during the flight test phase by an incremental process on an instrumented aircraft. A higher speed will be explored for flutter and measurements of the responses analysed to extract the frequency and damping in significant modes. The flutter model will be revised as necessary to reflect the measured responses and used to predict the flutter characteristics at a further increment of speed or Mach number above the flight test point. If this shows adequate aeroelastic stability margins then other aspects such as handling, FCS and loads will be explored up to the flutter test point. When these are cleared the next increment of speed can be made and a new test point explored for flutter.

It is obvious that setting the initial flight envelope has a direct impact on the time and cost of the flight flutter testing. The conservatism of the initial half-speed starting point is emphasised by the fact that a factor of one-half on speed corresponds to a factor of one quarter on dynamic pressure. Improvements in aeroelastic methods and confidence in flutter predictions can lead to a direct saving in the flight test programme if the first flight envelope can be allowed to be less conservative. This must always be tempered by the high likelihood that if flutter is encountered it will be catastrophic.

At the conclusion of the flight test programme, the final clearance will be either to the required full V_D or, in the event of a flutter limitation, to a maximum permitted speed based on the flutter speed and which will then take the place of V_D in operational airspeed clearances. The imposition of a more restrictive limit than had been the target represents one cost of a failure in the earlier aeroelastic analyses; had it been predicted earlier it may have been possible to avoid by redesign. However, this circumstance sometimes arises unavoidably for particular store combinations for

which redesign would not have been a feasible solution.

In addition to flutter, Section 4.8 of DEF STAN 00-970 also defines that aeroelasticity should be included in other analyses:

Effect of structural distortion on the loads on the aeroplane: In all design calculations associated with the requirements of Section 3, allowance shall be made for the flexibility of the aeroplane structure.

Effect of structural distortion on the stability and control of the aeroplane: In all design calculations associated with the requirements of Sections 2 and 6.5 allowance shall be made for the flexibility of the aeroplane structure.

The relevant subjects in Section 3 include: static strength and deformation, fatigue, symmetric manoeuvres, asymmetric manoeuvres, gust loads, control systems, and active control systems. The referenced Sections 2 and 6.5 cover handling, performance, and automatic control systems. Thus any aeroelastic analysis methods must have broad application to these fields, or at least compatibility with the methods used in the other analyses.

2.3. Review of current research into aeroelastics and aeroservoelastic prediction

This section is not intended to give an exhaustive review of the state of the art of aeroelastic prediction, but to place the work undertaken during the PUMA–DARP project in context with research that has been undertaken elsewhere and, in particular, the issues that have been identified as being of major interest to the aerospace industry.

2.3.1. Brief historical overview of linear flutter analysis

It can be presumed that many early aircraft suffered catastrophic structural failure due to a lack of understanding of interactions between the aerodynamic forces and the structure. The first recognised flutter problem that was solved [1] by providing a stiff connector between the left and right elevators was the Handley Page 0/400 bomber that contained an instability between the elevators and the fuselage torsion. The mathematical solution [20] was based upon the analysis of a two degree-of-freedom mathematical model using the Routh's stability criterion and a rudimentary aerodynamic model.

As the understanding of two-dimensional unsteady aerodynamics improved, the modelling capability of aeroelastic systems and flutter did as well. The seminal works by Frazer and Duncan (the “Flutter Bible”) and Theordorsen provided the mathematical background to predict flutter and provide design rules for two-dimensional aerofoils and, by implication, high aspect rectangular wings flown at low speeds. Classically by the 1950s [5,6] aerodynamic strip theory was used for flutter predictions, with corrections included for loss of lift at the wing tip, compressibility and aspect ratio effects, combined with an assumed modes structural model. The methodology could be applied to include control surfaces and also swept wings.

Aerodynamic strip theory contains the major assumption that the various strips have no influence aerodynamically upon each other, which is valid if wings can be considered as being slender and beam-like. The theory can be modified [21] to enable the reduction in lift at the tip to be modelled. However, configurations such as T-tails require a more sophisticated aerodynamic analysis, and this was provided by panel methods which were initially developed for a steady aerodynamic analysis, the vortex lattice approach is the best known [22], in the 1960s. Unsteady panel methods soon followed, with the doublet-lattice method [23] being by far the most widely used, see [24] for a discussion for current implementations. This approach, combined with the structural finite element method developed at a similar time, provides the fundamental elements that have been used for aeroelastic analysis for the past 30 years. The flutter solutions are based upon the use of modal harmonic oscillations, and the so-called frequency matching problem has to be solved to ensure that the aerodynamic forces and the structural motion match-up. The k and $p-k$ methods [25] are the most widely used examples of this type of method.

2.3.2. Building blocks for linear analysis

The doublet lattice [23,26] method is the most widely used approach for aeroelastic analysis and appears in the commercial software codes that are available. It is implemented in the form of a classical three-dimensional linear panel method such that the lifting surface is divided up into panels that are uniform in the streamwise direction. The aerodynamic forces are modelled as a continuous distribution of acceleration doublets along the quarter chord of each, and the influence of all the lines of

doublets is accounted for at a control point at the $\frac{3}{4}$ chord, mid span of each panel. The key output from the method is the AICs which determine for any given reduced frequency, the lift on each element (calculated from the doublet strength) due to the dynamic pressure and the motion of the other elements. It is usual to formulate the problem into modal space so that the AICs give the lift acting on each element due to each mode of vibration. Note that as the solution is posed as a harmonic solution, then the AICs are complex.

The structural model is determined using the finite element method using a combination of beam and shell type elements. The aerodynamic loads for each reduced frequency need to be coupled to the structural model through the determination of the equivalent forces and moments at all of the structural nodes that give the same effect as the distributed aerodynamic forces acting on the quarter chord of each panel. Having determined the model inertia and stiffness matrices from the FEM (it is feasible to include structural damping as well although it is usual to ignore this as the flutter solution will then be conservative) and the aerodynamic damping and stiffness matrices from the AICs, it is then possible to proceed to the characterisation of the aeroelastic behaviour.

For each flight condition and mode of interest, the aerodynamics and the modal frequencies need to be *matched*, often using either the k or $p-k$ methods [25]. V and Vg plots are then used to determine where flutter occurs. It should be noted that the analysis assumes a harmonic solution and that each mode is considered individually. Consequently, whereas all of the matching methods give the same solution for the flutter speed, they differ in the frequencies and damping ratios that they predict at sub-critical and super-critical solutions.

Wind tunnel tests are often performed to measure the unsteady aerodynamic forces at transonic conditions and these measurements can be used to correct the AICs in the transonic region. Once the AICs have been computed, the calculation process is relatively quick.

2.3.3. Non-linear mechanisms

Non-linearities can be present in an aeroelastic system due to a number of different phenomena that occur in the structure, aerodynamics, and control systems. These non-linearities affect the aeroelastic behaviour in a manner that cannot be predicted using linear analysis methods. The main non-linear

aeroelastic response phenomena are LCOs which can be considered as bounded flutter, sometimes this is referred to as non-linear flutter. Note that in some cases the LCOs can be made up of multiple sinusoids.

There are a number of review papers that should be consulted to provide an excellent background to the effect of non-linearities on aeroelastic systems [27,28].

2.3.4. Examples of sources of nonlinearities

Structural non-linearities manifest themselves primarily as non-uniform stiffness effects, including cubic stiffening root attachments of engine pylons, bi-linear stiffness of structural joints, and freeplay of control surface attachments. Some very flexible, or large, aircraft exhibit geometric stiffness non-linearities due to the large deflections that can occur in flight.

Aerodynamic non-linearities occur primarily in the transonic flight regime, where shock waves are present upon the wing or control surfaces, and the position of the shock waves can change in response to motion of the wings; the interaction of control surfaces with shock waves is sometimes referred to as *buzz*. Further examples of an aerodynamic non-linearity are when stall occurs at the wing-tips and lift is lost on the outer part of the wing, or when buffet occurs at large angles of attack and the tail surfaces are excited by the separated flows from the wings.

Control non-linearities can have a large influence on the behaviour of an aircraft that includes a FCS and they can manifest themselves in many ways. For instance, the control surfaces have deflection and rate limits whereby the control surfaces cannot respond in the manner that is required by control laws. Also, the control surface actuation mechanism tends to be non-linear as well as the control laws that are used. The use of non-linear, or multiple, control laws with time delays in their application, also leads to non-linear aeroelastic behaviour.

2.3.5. Examples of observed non-linear behaviour

There have been a number of laboratory based experiments that have demonstrated LCOs in aeroelastic systems, although these have been devoted to demonstrating the effects of structural nonlinearities such as cubic stiffening and freeplay on binary systems [29,30].

The most documented examples of LCOs occurring on full size aircraft have been on the F-16 [31,32] and F-18 [33] aircraft where they have been observed for a wide range of different store combinations.

2.3.6. Store induced LCO

There has been a fair amount of recent interest in the LCO behaviour of wing/store combinations and these studies have consisted of both numerical and experimental investigations.

Tang [34] tested a delta wing wind tunnel model with a store for variations in the store attachment stiffness and location. Although the critical LCO velocity and frequency were well predicted the LCO amplitude calculations differed somewhat from the experiment. Dawson [35] developed a neural network approach building for previous work [36,37] to predict LCO amplitude and frequency trends for different combinations of external stores on a fighter aircraft. Flight tests had previously been performed upon various asymmetric store configurations [38]. The results were reasonably successful and also were able to predict the “non-classical” LCO whereby the amplitude levels decrease after a certain airspeed.

Parker [39] performed a numerical investigation where underwing and tip stores were added to the Goland⁺ wing to determine how they affect LCOs. It was found that the aerodynamic forces on the store transferred additional energy into the structure, increasing the LCO amplitude, however, the underwing store also interfered with the airflow on the bottom of the wing, which limited the LCO amplitude. Janardhan [40] investigated the effect of store parameters on LCO behaviour in the transonic region using the CAP-transonic small disturbance (TSD) approach. It was found that the effects of the store mass, particularly the LCO onset speed, had a much greater influence than the change in the aerodynamics due to the store.

Beran [41] undertook numerical studies on LCOs occurring on numerical models of wings with stores using TSD theory including an interactive boundary layer model. It was found that the presence of stores caused LCOs to occur at lower speeds than for the clean wing using non-linear aerodynamics and also for the store case using linear aerodynamics. Kim and Strganac [42,43] investigated the effects on the numerical model of a wing with external stores. Non-linearities included the aerodynamics, geometric non-linearities and also kinematic non-linearities for the store. A range of different parameters were varied and the LCO characteristics described.

2.3.7. Computational aerodynamics

The advance of CFD has been well documented. Usable models have increased in fidelity through

TSD and full potential in the 1970s, Euler equations in the 1980s, Reynolds averaged Navier–Stokes (RANS) in the 1990s and more recently turbulence simulation through detached eddy simulation (DES) and LES. In terms of flow phenomena these models all allow the prediction of shocks, and the more advanced ones allow prediction of separation and massively separated flow. There are numerous examples of the application in a research environment of this capability to aircraft problems.

The exploitation of CFD for aeroelastic simulation has been called computational aeroelasticity. A typical approach is to generate surface forces from the CFD, pass these forces to a structural model, advance the structural calculation, change the surface shape for the CFD and so on. This sequence can be used to either advance towards an aerostatic solution, or to calculate the dynamic response. The following four considerations provide challenges to the development of such a simulation

- (a) How to sequence in time between the fluid and structural models.
- (b) Passing of information between the fluid and structural grids.
- (c) Movement of the CFD grid.
- (d) The computational cost of the unsteady CFD solution.

These steps have been addressed within PUMA and can be illustrated with reference to examples. Melville [44] computed an LCO response of the F-16. This calculation was done on an overlapping structured grid. The mapping of modes from the structural grid onto the CFD surface grid was done component by component using tailored basis functions. The mesh movement was achieved by exploiting an algebraic expression which drives the displacement of a point in the fluid volume domain by weighting displacements from the nearest surfaces.

Farhat [4] also showed simulations of the F-16 on unstructured grids with a detailed structural model. A three field formulation was used, which regards the moving mesh as a field alongside the fluid and structural fields. A spring analogy was used to move the grid. The detailed structural model means that the transfer problem is simplified, and the structural basis functions are used. Finally, a staggered scheme is proposed to eliminate the reduction in temporal accuracy that can result from the sequencing between the fluid and structural solvers.

Pranata [45] generated results for the F-16 LCO response using the NLR Enflow system. The multi-block structured grids were deformed by using a volume spline method on the blocks, and transfinite interpolation (TFI) within blocks. Sub-iterations within each time step were used to sequence the fluid and structural solvers correctly in time. A volume spline is used to effect the transfer between the fluid and structural grids.

Issue (a) has been tackled satisfactorily in a number of ways that seem satisfactory. Farhat [4] analysed and applied a staggered scheme which avoids subiteration. Goura [46] incorporated the structural solver within the pseudo-time stepping loop of the CFD solver. The incorporation of the structural solver into the pseudo-time loop did not increase the number of iterations needed to convergence, and so had little impact on the computational cost.

Issue (b) is of particular concern where the aircraft structural model has used a simplified representation (e.g. using a beam to model the fuselage) of the geometry. Since a key step in a production aeroelastic analysis is the careful matching of normal modes with ground resonance test measurements, such simplified models can be attractive, both to ensure a set of clearly defined modes, and to facilitate model tuning to achieve matching. A mismatch between the surfaces on which grids are defined makes the transfer problem more difficult. This problem is considered in Section 4.1.1.

An important consideration related to grid treatment is the incorporation of control surfaces. The difficulty lies in the changes of topology throughout the motion. This makes grid deformation a difficult option. Sliding grids have been used in turbomachinery with success and have potential for control surface edges. A second interesting option is to blend the control surface edge into the wing. This problem is considered in Section 4.5.

There are several approaches available for issue (c). For unstructured grids a spring analogy is often used to deform the mesh [4]. A parameterisation of the space in which the grid is defined is suitable for structured or unstructured meshes [44]. In the current work, block structured grids are used with the aim of the deformation being to preserve high quality grids throughout the simulation.

Finally, the issue of reduction in computational cost (issue (d)) is reviewed in the next section, and then considered in Section 6.2.

In the current research effort the aim was to advance the use of computational aeroelasticity as a

usable tool within the partner companies. A good unsteady flow solver for block structured grids around complex geometries was the starting point. The key points to be considered were grid movement, information transfer for production structural models and the grid treatment for control surfaces.

2.3.8. Model reduction

A ROM approach is essentially any method that produces a model that is of a much smaller size than the full order CFD/FE model. In order to be accurate and useful, however, it must still contain the important linear and non-linear characteristics of the full size system.

In Dowell and Hall [12] a review of all the classical methods to predict stability boundaries is given. This includes harmonic balance (HB), non-linear ROM of the CFD, eigenmode method, and proper orthogonal decomposition (POD).

Reduced systems have then been found by a number of techniques when the flow is assumed to be harmonic with a discrete frequency, most prominently via eigenmode summation and POD as in Romanowski [47]. Eigenmode summation has been used to reduce the Euler equations [48]. However, the application of POD is increasingly investigated with models constructed for the Euler equations by Hall et al. [49,50]. Further improvements via balanced POD by Willcox [51] and Schmidt and Glauser [52] have also been obtained.

Another study by Lieu and Farhat [53] built upon previous work on the global POD to employ the POD on a 170k CFD finite element (FE) model at different speeds. They used the subspace angle interpolation method to interpolate between different speeds and obtained a reasonable agreement, but only of the damping prediction.

There has been quite a lot of interest in the use of higher order spectral methods to curve-fit output only data from a wind tunnel [54] and flight test data [55]. Although these methods extract non-linear information, they require a vast amount of data and it is not possible to link the models between different flight conditions.

Researchers at Duke University have put a lot of effort [56] into modelling the LCO behaviour of the F-16 using variations of the HB applied to the CFD/FE time simulations. Reasonable results were found compared to the flight test data, including the prediction of LCO frequency and amplitude vs Mach number, and the work of Liu et al. [57] has

extended the higher order harmonic balance (HOHB) method.

This problem may be approached in several ways. Either some form of non-linear identification algorithm can be used to determine a non-linear model at each flight condition, or a more aero-elastically aligned approach can be made that directly identifies terms in the non-linear model.

Examples of the direct use of non-linear identification methods include Mamerstein modelling [58] on classical pitch–plunge models and the non-linear frequency domain reverse path spectral method [59], which was used to curve-fit structural non-linearities on AAW data. Popescu et al. [60] have developed an approach that can determine whether there is freeplay, hysteresis or polynomial stiffness non-linearities using the Naadaraya–Watson non-parametric approach. This method has only been used on a three degree-of-freedom system.

Lind et al. [61] have developed a methodology that builds upon the μ method for flutter prediction and determine a Volterra based method for identifying the effect of parameter variations. They have demonstrated how this can be included in a model to predict the flutter boundary on a two-dimensional aerofoil model. Chabalko et al. [62] applied the continuous wavelet transform to data from HSCT wind tunnel tests. This time–frequency approach cannot be used to predict ahead in speed.

There is a body of work that curve fits a discrete-time pulse from the CFD/FE models. This is a discrete-time implementation of the continuous-time CFD equations to identify the discrete-time pulse responses of the system, which characterise all solutions of the dynamically linear system Raveh [63] and Silva [64].

Munteanu et al. [65] used a Volterra based ROM using the derivative of the aerodynamic step response and included first and second order terms. ERA was used to transform from ROM unsteady aerodynamics to the LTI state-space model. The method was tested on two-dimensional and three-dimensional models but only up to $M = 0.6$ and no structural non-linearities were included. In [66] Munteanu uses a ROM derived from CFD data to compare with a full CFD solution; this time both structural and aerodynamic non-linearities are present and the method was applied to a pitch–plunge aeroelastic model.

Prazenica et al. [67] curvefitted a 2D pitch–plunge model and F/A-18 AAW data using Volterra kernels obtained via wavelets to model the aero-

elastic behaviour. They attempted to extrapolate between the different flight speeds but found difficulties in this approach.

Probabilistic methods have been used in gust analysis for several decades, but it is only recently that they have been applied to the study of aeroelastic stability analysis. Pettit and Beran [68,69] use the polynomial chaos expansion (PCE) to obtain a spectral representation of the stochastic responses. The LCO boundary was determined via a probabilistic method rather than a simulation at each test point. Some of these issues, like the long term energy issues associated with the PCE, have been addressed by Pettit and Beran [70] by using Wiener–Haar wavelet transform. A lot of work is still required before a set of practical tools are available. All of the methods have been applied to a typical two-dimensional airfoil section with pitch/plunge degree-of-freedoms.

Attar and Dowell [71] analyse parametric uncertainty of the response of aeroelastic systems using the response surface method by mapping the input to the output via a two region regression algorithm. The method has proved itself more computationally efficient than a full Monte-Carlo simulation.

Finally, work is also progressing [72–74] into the use of aerodynamic indicial functions obtained from the CFD results that can be used to simplify the aerodynamic models in all flight regimes. So far this has only been applied to simple 2D pitch–plunge models.

In general, model reduction offers the prospect of an efficient means of obtaining CFD/FE model accuracy for aeroelastic problems at an affordable cost. A variety of techniques and approaches have been successfully applied, as described above. As yet, however, these approaches have only been applied to comparatively simple systems and it is clear that substantial advances are required to enable cases of realistic complexity to be attempted.

3. Test cases

The test cases used in this programme are indicated in Fig. 1 and their reason for inclusion (purpose) and schedule for use (which methods) are indicated. Tables 1–8 provide a brief summary of each case; the reader is referred to the references therein for full details.

Table 1

Test case	BAH wing
Configuration	Wing with aileron
General description	A typical jet transport wing devised by Bisplinghoff et al. [5] to illustrate aeroelastic techniques, and adapted for use as a demonstrator for the MSC.NASTRAN software by Rodden et al. [75]
Model	Mathematical model, as used in [76], comprising aerodynamic influence coefficients and a finite element model. Bilinear stiffness has been added by the researchers to control surface rotation to introduce non-linearity.
Motion	Flutter and LCO (with additional bilinear stiffness)
Data	Case is used to provide validation by comparison with results obtained through numerical integration
Use	To explore structural non-linearity using HOHB and continuation methods
Conditions	Airspeeds 400–620 ft/s at sea level

Table 2

Test case	Goland wing
Configuration	Wing + effect of tip store
General description	A heavy unswept wing with 4% parabolic section [77]. A tip store has small aerodynamic effect, but significant dynamic (inertia) effect. The configuration exhibits a narrow range of aerodynamic-driven LCO in the transonic region
Model	CFD model of the clean wing (i.e. no store) structural model includes the effect of a tip store
Motion	LCO driven by non-linear aerodynamics
Data	There is no experimental data, but a good number of calculation results from a variety of methods
Use	Provides a narrow region of shock induced limit cycle oscillation to test the methods
Conditions	Mach number between 0.7 and 0.95

4. Time-domain CFD based methods

Aeroelastic methods generally combine an aerodynamic model with a structural model into a single simulation, but the degree to which these component parts are integrated varies. In many cases, the models have been developed entirely independently and are then *bolted* together through some coupling procedure.

4.1. Overview

The effects of thickness are not included in the linear aerodynamics models, and so a spline method

Table 3

Test case	MDO wing
Configuration	Large transport wing
General description	The MDO wing [78,79] is a large transport wing developed in a BRITE Euram project on multi-disciplinary optimisation and used as an aeroelastic test case in the Framework IV UNSI programme [80,81]. A number of results have been presented. Three test points at different altitudes providing stable, marginally stable, and unstable conditions. It provides a case with a good degree of aerodynamic non-linearity and, as such, represents a more difficult test case than the AGARD 445.6; for this case clear differences between the solution from linear and non-linear methods are evident
Model	CFD model of the wing. MSC.NASTRAN modes for structural model
Motion	Appropriate for flutter prediction
Data	There is no experimental data, but a wealth of computational results
Use	Test case for coupled CFD-CSM methods
Conditions	Economic cruise ($M = 0.85$, Alt. = 11.2 km), stable; heavy cruise ($M = 0.88$, Alt. = 7 km), marginally stable; heavy cruise ($M = 0.88$, Alt. = 2 km), flutter

has generally been used to transfer data between the models which are both defined on a plate. When the aerodynamic model is an Euler or Navier–Stokes CFD code, thickness becomes significant and exact shape representation is required for the aerodynamic solver. This has a number of implications for development of these coupled methods.

- A coupling method is required that ensures conservation, consistency and shape preservation between the structural and aerodynamic models. This must be achieved despite the aerodynamic and structural grids being non-coincident; indeed the structural grid could even lie outside the aerodynamic shape due to the lower geometric resolution associated with structural modelling (see, for example, Figs. 5 and 6).
- Aerodynamic grid points must be moved in a way that maintains grid quality. It should be noted that this must include the movement of control surfaces, where the topology may change and where discontinuities appear in the surface geometry.
- The coupling scheme must ensure that temporal stability is maintained and is consistent between the two models.

Table 4

Test case	AGARD 445.6 Wing No. 3
Configuration	NACA 65A004 constant section, 45° quarter-chord sweep, 0.66 taper ratio
General description	The model [82] was tested in the NASA Langley wind tunnel in 1963 and has remained a popular test case ever since, being one of the few publicly available flutter test cases. The data have a non-linear flutter and exhibits the transonic dip, however, because the wing is thin and has no camber, the transonic flow and shock formation are delayed until a relatively high Mach number, with the transonic dip occurring at about $M = 0.9$. Thus, linear methods also perform comparatively well for this test case, due to a lack of thickness and camber.
Model	The AGARD 445.6 wing was made of mahogany with a 45° quarter chord sweep, a root chord of 22.96 in and a constant NACA64A004 symmetric profile [82]. Stability characteristics were determined through a series of experiments carried out at the NASA Langley transonic dynamics tunnel, and reported in 1963. Various wing models were tested (and indeed broken). Most published results have appeared for the weakened wing (wing 3). This wing was deliberately weakened (by drilling holes subsequently filled with plastic to maintain the aerodynamic shape). The aerodynamic shape can be easily derived from the specification and the structural characteristics of the wing were documented in the form of measured natural frequencies and mode shapes derived from a finite element model.
Motion	Appropriate for flutter prediction
Data	Experimental data at zero incidence for Mach numbers in the range 0.338–1.141. There are a wealth of computational results available in the literature; all show a significant differences with experiment at the highest Mach number (supersonic condition) tested [9].
Use	Used across the range of methods investigated, including current linear methods, to compare flutter prediction capability
Conditions	As per experimental conditions

4.1.1. Physical coupling

Aeroelastic tools generally work by combining an aerodynamic model with a model of the aircraft structure; some relationship between the two must be established in order that the interaction between fluid and structural elasticity can be predicted. Fig. 2 indicates that these models are generally derived individually and that some sort of coupling between them is needed. For a traditional linear model the aerodynamics is derived from potential theory and transformed into a set of AICs and the

Table 5

Test case	BACT Wing
Configuration	Rectangular wing with hinged part-span flap
General description	The Benchmark Active Controls Technology (BACT) wing is a test case specifically designed for validation of aerodynamic, aeroelastic, and active aeroelastic control simulation codes [83]. Extensive test results were obtained by NASA, in the NASA Langley transonic wind tunnel, at transonic conditions for self-excited or control surface-driven flutter. The model is particularly useful for investigating aeroelastic effects in which control surfaces play a role
Model	A rectangular wing with a NACA0012 section and a trailing edge control surface between 45% and 75% span and hinged at 75% chord. Spoilers were placed on the upper and lower surfaces ahead of the flap. Nominal structural dynamics parameters were measured and a representative structural modal has been created from these
Motion	Oscillations about the control surface hinge line and dynamic response including flutter measured on pitch/plunge apparatus
Data	Steady and unsteady pressures measured together with actual motion for a range of Mach numbers between 0.65 and 0.85 [84,85]
Use	Used to test flap motion for coupled CFD-CSM methods
Conditions	$M = 0.75, 0.77; \alpha = 0^\circ, 2.5^\circ; \beta = 5^\circ, 10^\circ$

Table 6

Test case	Generic Large Aircraft (GLA)
Configuration	Large passenger aircraft configuration, including pylons and nacelles
General description	There are two variations of the (ATTACH) Generic Large Aircraft: clean wing/body (WB) and wing/body/nacelle + pylon (WBNP)
Model	CFD grids are provided for both WB and WBNP models and a FEM is available for the WB model
Motion	The only motion tested in this programme is forced oscillation of the nacelle
Data	High Reynolds number wind tunnel pressure measurements and deflection predictions have been made for the WB model (tested in the European wind tunnel)
Use	This model has been used to check the grid movement of coupled fluid–structure methods for complex configurations
Conditions	N/a

structural model is expressed as a set of vibration modes. It is helpful to consider the different types of model that may be derived in order to understand the challenges associated with developing

Table 7

Test case	NAL SST arrow wing with oscillating flap
Configuration	Semi-span arrow wing with fuselage
General description	The supersonic transport (SST) wind tunnel model was specifically tested for the purpose of verification of aeroelastic CFD codes and active control technology [86]. It has a NACA0003 section and is a cranked double delta wing. A fuselage swell near the wing trailing edge, which was present in the experimental model to house the flap oscillation mechanism, is eliminated from the CAD model. The wing tip is modelled by rotating the aerofoil at the tip.
Model	The model was proposed by the Society of Japan Aircraft Company (SJAC) and a full description is available from Refs. [86–88]. Both geometric and finite element models (structural) are available. It is a double swept-back semi-span delta wing with a simple fuselage. The structure of the SST was modelled as a two-dimensional plate in MSC.NASTRAN with the aid of the PATRAN preprocessor.
Motion Data	Sinusoidal pitching of flap about swept hinge line Steady and unsteady pressures, together with motion of points on model. Note that unsteady forces at specified sections are also available in the original data set.
Use	Used in this programme to test the flap modelling of coupled CFD-CSM method. This model is excellent for testing the elastic capability of coupled CFD-CSM methods with validation data in the transonic range.
Conditions	Mach number = 0.8, zero angle of attack, and flap frequency varied between 5 Hz and 25 Hz

aeroelastic tools that work in the time domain, as opposed to the frequency domain.

The very complexity of an aircraft design means that for aeroelastic calculations it is impractical to construct a detailed structural model that includes all the internal structure, and indeed the important dynamics can often be described using a simplified model. Instead the structure is usually modelled as an external FEM from which more simple models can be derived that are appropriate to the fidelity required and the application. Traditionally, the structural models for aeroelastic applications have represented the aircraft as a set of beams, sticks and plates (e.g. Ref. [82]). Thus it is generally true that the data nodes of the structural model and the aerodynamic model do not coincide so that some form of interpolation is required to express the aerodynamic forces on the structural model and the shape change (structural response) on the aerodynamic model.

Table 8

Test case	Hawk aircraft
Configuration	BAE Systems Hawk Aircraft; complete aircraft model, with all major components and including geometry with combat flap
General description	The Hawk aircraft is an advanced jet trainer with a low-mounted swept-back wing that is tapered with a curved tip. Although basically a subsonic aircraft, it can attain supersonic speeds in dive.
Model	Multiblock grids were generated for a number of configurations, including wing only, wing with combat flap, wing-fuselage and tailplane, wing-fuselage-tailplane-fin-rudder. The structural model is based on beams. To obtain aeroelastic results for non-linear phenomena, the model has also included cases in which the wing is artificially weakened so that the structural modulus is an order of magnitude lower.
Motion	Control surface motion, including combat flap and rudder buzz
Data	Flight test aeroelastic data were provided for evaluation of the codes
Use	The principal use of this configuration within this programme has been to establish the viability and effectiveness of the coupled CFD-CSM method for real aircraft configurations
Conditions	Run in transonic conditions

There have been various attempts to overcome these difficulties. The simplest conceptually and most accurate is to construct, or reconstruct, a high fidelity structural mesh with one-to-one correspondence in node number and location, solved concurrently (in real time) with the aerodynamic mesh. However, in practice this is an inefficient use of resources, and indeed the reconstruction is impossible from some simplified models. Alternatively a three stage process may be used, comprising projection, interpolation, and recovery (the latter formally being the same problem as projection, although using different notation). The process involves interpolating structural displacements onto a non-matching aerodynamic grid, and forces from the aerodynamic grid back to the structural grid, and may be achieved in several ways.

Projection may be achieved by a loads interface model, specially recreating the missing structure in the FEM. However, this is not always possible, and it is time consuming. Alternatively the missing structure may be assumed to be linearly elastic, and then an interpolation based on a boundary element method [89,90], constant volume tetrahedra (CVT, discussed below) can be used. Finally constant displacement, solid rod, or projection

methods may be used. For a discussion on the relative methods of each, see Ref. [91]. Of these, the latter three are similar, do not allow for elastic behaviour, and are particularly suited for flat plate structural models.

The interpolation stage may either in some cases be bypassed by having all aerodynamic surface points assigned individual displacements in the projection stage, or more usually achieved by one of many splining techniques, such as infinite plate spline, thin plate spline (TPS), the multiquadratic-biharmonic method, finite surface spline, or an inverse isoparametric method (IIM). For an extensive evaluation of these methods see Ref. [92]. The TPS method was generally found to perform the best particularly in areas with limited structural nodes (e.g. leading and trailing edges).

Finally, weighting functions can be used which use the shape functions of fluid flow and an intermediate plane to integrate forces [93,94]. However, definition of the intermediate plane is difficult, as integration of the product of fluid and structural forces is required, and in turn this demands a common surface, which does not actually exist. In general, intermediary meshes may be used to solve this problem [95], but construction of such is not straight forward. Despite this the method has been successfully applied. Other possible alternatives include the moving least squares and IIM, the former also being a weighting method and hence limited in the same way, and the latter based on shape functions.

The two coupling methods used in the PUMA DARP shared significant areas of similarity. Both are based on the constant volume tetrahedra (CVT) scheme, and hence an important part of the work on full non-linear simulation was to compare the results produced by different codes that used similar transformations, to determine the priority of solver over coupling method in aeroelastic simulations, and furthermore to develop and validate the methods against more complex vehicle shapes, in terms of configuration and structural model complexity. The significance of this work is highlighted by the similarity of results produced for test cases in which previous workers had found significant variance (specifically the multi-disciplinary optimisation (MDO) wing, discussed below in Section 6.3)—this suggests the importance of the coupling scheme, and its reliable implementation into any aeroelastic code in providing at least consistent

results (accuracy being a separate issue, and more difficult to prove in the MDO case).

In this section the two approaches to coupling the aerodynamic grid and the structural model are considered for the general case in which the two grids are entirely non-coincident. The validity of these approaches has been established and their ability to satisfy the fundamental requirements for accurate shape representation and conservation are demonstrated. Two CFD codes have been used in the studies reported herein: the PMB code developed at Glasgow University [96] and the RANSMB code originally developed by British Aerospace [97] and extended for aeroelastic applications by Bristol University. Both these codes use a multiblock grid strategy with structured grids within each block. The grid movement schemes are, therefore, derived for this particular grid approach, however, certain of the principles for grid movement are more generally applicable. The grid movement schemes are described and their capabilities for handling complex movement, including control surfaces are presented. Coupling between the structural and aerodynamic solutions can either be synchronous (strong) in time, or not (weak). Previous work has established the strong coupling temporal approach [98] and this is not described further in this paper. Structural behaviour is represented by modal analysis, although other methods have been examined [99].

4.2. Fluid–structure coupling for aeroelastic modelling

In computational aeroelasticity fluid forces must be communicated to a structural grid, and in return resulting deflections of this grid must be communicated back to the aerodynamic mesh. This problem is complicated by the fact that the nodes in these grids are of differing number (far less are required in the structural solver for solutions of equivalent accuracy), are not located at the same points in Cartesian space, and indeed are often located on entirely separate surfaces. An efficient and accurate coupling method is therefore critical in developing coupled CFD–CSD methods. Both PMB and RANSMB use as a foundation of this process the CVT formulation.

The CVT scheme is a transformation technique proposed in Goura [101]. Each fluid surface grid point ($\mathbf{x}_{a,l}$) is first associated with a triangular element Δ constructed from three structural grid

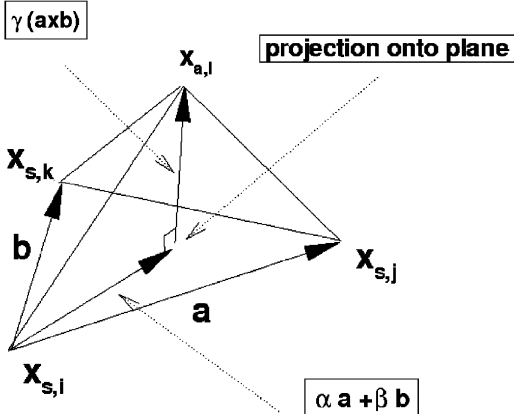


Fig. 3. Tetrahedron used for the CVT transformation [102].

points ($\mathbf{x}_{s,i}$, $\mathbf{x}_{s,j}$ and $\mathbf{x}_{s,k}$). The position of $\mathbf{x}_{a,l}$ is given by the expression

$$\mathbf{x}_{a,l} - \mathbf{x}_{s,i}(t) = \alpha \mathbf{a} + \beta \mathbf{b} + \gamma \mathbf{d}, \quad (1)$$

where $\mathbf{a} = \mathbf{x}_{s,j} - \mathbf{x}_{s,i}$, $\mathbf{b} = \mathbf{x}_{s,k} - \mathbf{x}_{s,i}$, and $\mathbf{d} = \mathbf{a} \times \mathbf{b}$. Here the term $\alpha \mathbf{a} + \beta \mathbf{b}$ represents the location of the projection of $\mathbf{x}_{a,l}$ onto Δ and $\gamma \mathbf{d}$ is the component out of the plane of Δ , as shown in Fig. 3. In the above the values of α , β and γ are calculated as

$$\alpha = \frac{|\mathbf{b}|^2(\mathbf{a} \cdot \mathbf{c}) - (\mathbf{a} \cdot \mathbf{b})(\mathbf{b} \cdot \mathbf{c})}{|\mathbf{a}|^2|\mathbf{b}|^2 - (\mathbf{a} \cdot \mathbf{b})(\mathbf{a} \cdot \mathbf{b})}, \quad (2)$$

$$\beta = \frac{|\mathbf{a}|^2(\mathbf{b} \cdot \mathbf{c}) - (\mathbf{a} \cdot \mathbf{b})(\mathbf{a} \cdot \mathbf{c})}{|\mathbf{a}|^2|\mathbf{b}|^2 - (\mathbf{a} \cdot \mathbf{b})(\mathbf{a} \cdot \mathbf{b})}, \quad (3)$$

$$\gamma = \frac{|\mathbf{c}| \cdot \mathbf{d}}{|\mathbf{d}|^2}. \quad (4)$$

Eq. (1) gives a non-linear relationship between the fluid and structural locations which can be linearised in the structural displacements to give

$$\delta \mathbf{x}_{a,l} = \mathbf{A} \delta \mathbf{x}_{s,i} + \mathbf{B} \delta \mathbf{x}_{s,j} + \mathbf{C} \delta \mathbf{x}_{s,k}, \quad (5)$$

$$\mathbf{A} = \mathbf{I} - \mathbf{B} - \mathbf{C},$$

$$\mathbf{B} = \alpha \mathbf{I} - \gamma \mathcal{U} \mathcal{V}(\mathbf{b}),$$

$$\mathbf{C} = \beta \mathbf{I} + \gamma \mathcal{U} \mathcal{V}(\mathbf{a}),$$

$$\mathcal{U} = \mathbf{I} - \frac{2}{d^2} \mathcal{D}(\mathbf{d}) \mathcal{S}(\mathbf{d}), \quad (6)$$

$$\begin{aligned} \mathcal{V}(\mathbf{z}) &= \begin{pmatrix} 0 & -z_3 & z_2 \\ z_3 & 0 & -z_1 \\ -z_2 & z_1 & 0 \end{pmatrix}, \\ \mathcal{D}(\mathbf{z}) &= \begin{pmatrix} z_1 & 0 & 0 \\ 0 & z_2 & 0 \\ 0 & 0 & z_3 \end{pmatrix}, \\ \mathcal{S}(\mathbf{z}) &= \begin{pmatrix} z_1 & z_2 & z_3 \\ z_1 & z_2 & z_3 \\ z_1 & z_2 & z_3 \end{pmatrix}. \end{aligned} \quad (7)$$

To avoid incurring significant errors from this linearisation, it is always applied about the current structural location, as opposed to the original (undeflected) one. Hence there is a linear relationship for each application of the transformation, and the principle of virtual work is then used to give the force transformation. Denoting the linear relationship defined by Eq. (5) as

$$\delta \mathbf{x}_a = S(\mathbf{x}_a, \mathbf{x}_s) \delta \mathbf{x}_s, \quad (8)$$

the force transformation is given as

$$\delta \mathbf{f}_s = S^T \delta \mathbf{f}_a. \quad (9)$$

This method was used for single component aeroelastic calculations in Goura [101] and Goura et al. [103]. A version of this method that deals with structural models that feature beams was developed in Rampurawala [104].

The CVT scheme may be supplemented for sparse grids through the use of an intermediate grid approach, defined by the intersection of the outward normals of the structural grid with the aerodynamic surface. The interpolation of the displacements from the structural to the intermediate grid uses the non-linear CVT method described previously. The tetrahedra are found by connecting each point on the intermediate surface to the accompanying triple/triples on the structural surface (see Fig. 4).

As the intermediate and aerodynamic grids now coincide, the interpolation process is simplified, and thin plate spline (TPS) [105,106], is used for this process. A full description of this and several other possible methods may be found in Ref. [91]. However, for the cases described herein, it was generally found that this process made little improvements to the results.

Interesting challenges can be introduced by behaviour arising from the FEM. The main requirement of the structural model is that the main

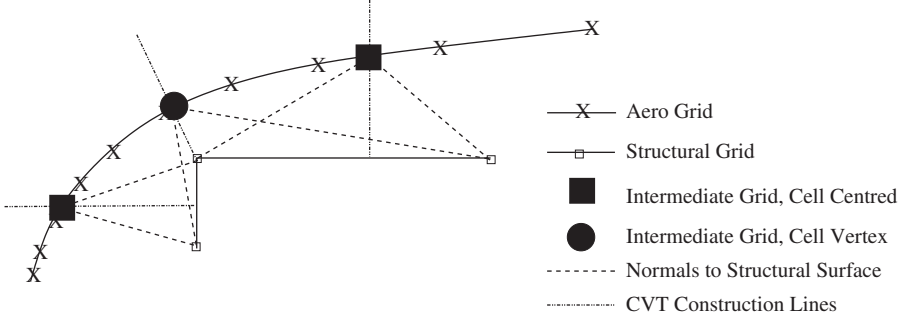


Fig. 4. Aerodynamic, structural, and intermediate grids, from [91].

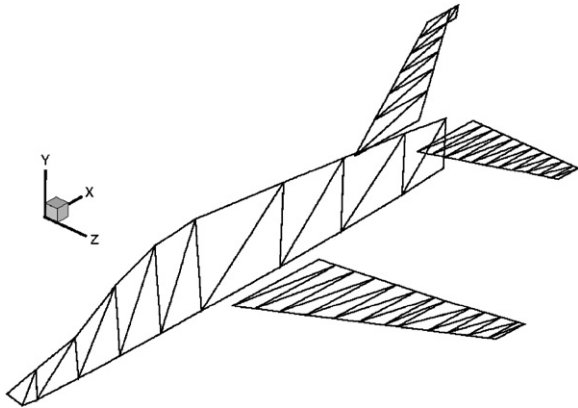


Fig. 5. The triangular surface elements for a structural model of the Hawk [102].

modes observed in the GVT are represented. This can be possible for low order models, perhaps involving beams and plates. Low order models have the advantage that they are computationally compact (although when the cost of CFD calculations is considered this is a minor advantage) and that they can be matched with GVT data by changing a relatively small number of parameters in the model. Legacy models (e.g. of the Hawk aircraft shown in Fig. 5) are of this type. An example of the behaviour in the FEM which poses problems in the transformation arises at the tailplane root. The tailplane is not constrained to follow the fuselage there in this model, and in fact for some nodes they move in different directions. This is not important for predicting the modes adequately, but it poses difficulties for constructing a closed description of the geometry for the CFD surface grid. This is illustrated in Fig. 6(a) where the tailplane and fuselage junction becomes crossed over and the vertical fin detaches from the fuselage. Even very

small mismatches like this can lead to poor grid quality (see [104]).

To overcome this a multi-level mapping method was developed. The idea is that the motion of points on, for example, the wing is not independent of the fuselage to which the wing is attached. The wing points must therefore attach to the fuselage as the wing root is approached. A transformation is defined for each component and is then averaged according to a hierarchy to ensure that components match at junctions. In the Hawk case two levels are defined, one for the fuselage and one for all other components. The fuselage is defined as being predominant so all components attach to the fuselage as it is approached. The distance from the nearest fuselage fluid point is calculated for all fluid surface points. This is then used to weight the transformations obtained from the two levels, one based on linking all components to a triangle on the fuselage structural grid and the other based on linking to a triangle on the correct component (i.e. wing fluid points to triangles on the wing structural grid, fuselage fluid points to the fuselage structural points, etc.). As the fuselage is approached, all the weight is put on the fuselage based transformation, ensuring that the junctions are properly defined. The resulting improvements in the surface definition are shown in Fig. 6(b). Finally, on coarse FEM grids, the method of associating aerodynamic points with structural triangles needs some care. This issue was considered in Ref. [102].

A similar problem was encountered for the Generic Large Aircraft (GLA) WBNP model due to the presence of multiple structural elements (body, wing, nacelles, and pylons) which do not coincide at nodes. This model was chosen as a test to demonstrate the capability of the PUMA methods for a complex, but important, geometric feature of civil configurations. In many studies, only

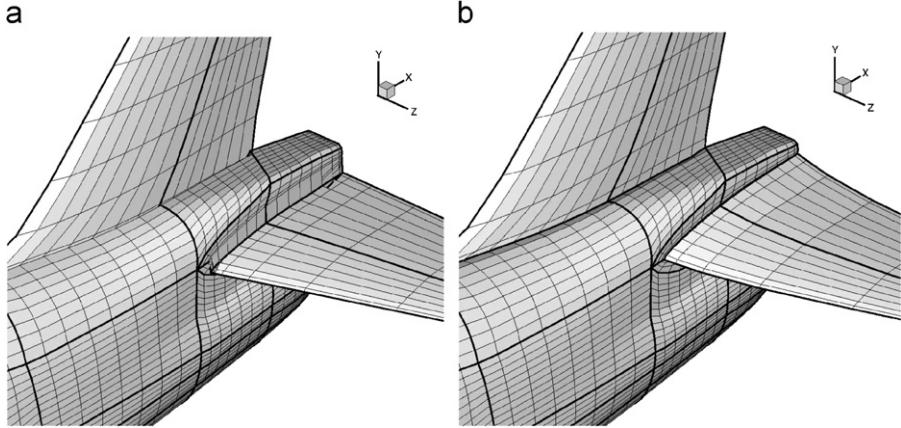


Fig. 6. Difference in one and two levels transformed surfaces showing the folding of the grid in the junction regions when using the one level transformation [102]: (a) one level; (b) two levels.

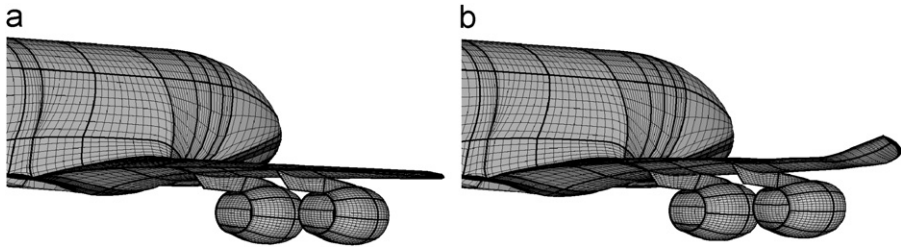


Fig. 7. Deformations of complex configurations: the GLA WBNP model (block boundaries highlighted in bold: (a) undeflected; (b) deflected).

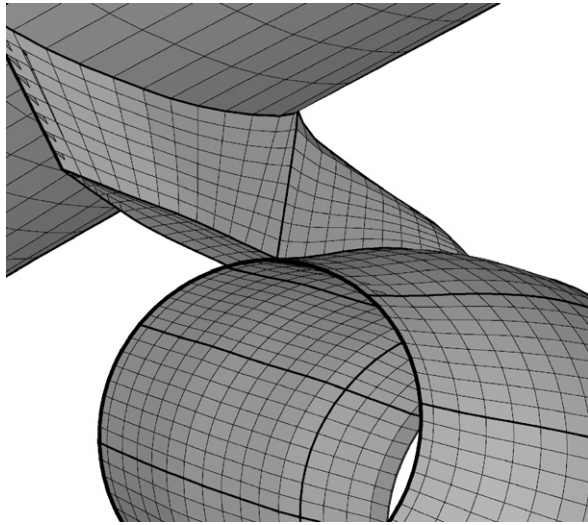


Fig. 8. Detail showing deflected nacelle pylon wing region, GLA WBNP.

the structural effect of the nacelle/pylon has been accounted for and the aerodynamic effects ignored. As shown in Figs. 7 and 8, a hierarchical smoothing process allowed continuous surface geometries,

facilitating high fidelity modelling of complex features. This process becomes even more important for Navier–Stokes types grids with fine cells near the surface.

4.3. Moving grid methods for unsteady CFD

4.3.1. Introduction

The movement of the computational grid associated with the displacement of a prescribed boundary can be a challenging problem in aeroelastic simulation as the displacement from jig shape to flight shape, and then from flight shape to dynamic displacements may be large. Previous work [107,108] demonstrated that a complete regeneration of the grid is an unnecessary overhead and that any surface motions may be considered as displacements to some initial (mean) grid. This initial grid must be provided as input and may be generated using any of the usual multiblock mesh generation techniques.

In the solvers used in this work, the multiblock partitioning of the domain is defined as one to one i.e. each block face has only one adjacent block with

only one type of boundary condition. This means that solid surface edges always coincide with block edges. This definition allows the motion of the block boundaries to be used to represent the gross motion of the computational domain.

For structured *single* block grids, it has been shown [107,108] that an algebraic decay of the surface displacements into the rest of the computational domain is an efficient grid movement method. But multiblock grids are unstructured at the block level and so this simple technique cannot be applied across block boundaries. For small motions, with relatively large blocks at the surface, it may only be necessary to move these large blocks, but if solutions are required where the aircraft jig shape is used for the original CFD grid, then the static aeroelastic deformation will be too large for this method to work on most multiblock grids.

The use of the linear spring analogy, with a Jacobi iterative solution, has long been used for unstructured dynamic grids [109]. This involves replacing each grid line with a spring whose stiffness is given the reciprocal of the grid line length to some integer power. The spring stiffnesses can be recalculated between each new grid, which produces a large computational overhead and does not guarantee that the mesh will remain close to the mean grid over large numbers of oscillations. Alternatively the spring stiffnesses can be fixed at the initial values of the mean grid. However, the resulting scheme will produce grid cross-over [110], particularly for rotations of the moving surfaces. A further consideration against the direct application of the spring analogy is that the number of iterations required by the Jacobi solution increases proportionally with the number of points [111]. We therefore see that the algebraic methods, of transfinite interpolation (TFI), are not robust relative to multiblock topologies while the spring analogy with fixed stiffnesses is not robust relative to large displacements and does not maintain orthogonality.

The methodology used in this work combines the spring analogy, with fixed stiffnesses, to calculate the block boundary motions and then TFI to define the motion within each block. Forcing functions [107,108] are defined at the moving boundary and decayed exponentially into the domain to ensure grid qualities are maintained. Using this forcing function, the displaced grid near the surface possesses the same spacing and degree of orthogonality (at the block level) as the initial mesh. The main difficulty in using this method is that the

multiblock mesh is unstructured at the block level and the exponential decay of the forcing function along the block edges becomes more complex [110].

The motion of the body surface is split into three components; corner, edge, and face displacements. The grid block boundary motion is the sum of these three components with the block interior motion then calculated using TFI.

To demonstrate the effect of the forcing function on the motion of the block edges, the rigid pitch of a generic wing–body–pylon–nacelle configuration is considered. The undisturbed surface grid for this configuration is shown in Fig. 9(a) while Fig. 9(b) shows block edge detail of the undisturbed grid for a vertical section running chordwise through the centre of the wing–pylon–nacelle. It can be seen that the block topology is complex and the blocks are small near the surface. Fig. 9(c) and (d) shows the block edge positions, on this same vertical section, after a 30° rigid rotation (pitch up). Fig. 9(c) shows the results using the forcing function and demonstrates that the surface blocks are almost rigidly rotated with the surface. By contrast Fig. 9(d) demonstrates the results when the forcing function is not used, close inspection shows that many blocks around the surface are highly skewed or even completely collapsed.

4.4. Initial validation: AGARD 445.6 flutter boundary

The methods described were developed to model the aeroelastic behaviour of aircraft. To build confidence, the methods were applied to the AGARD 445.6 weakened wing (wing 3) [82,9].

Flutter boundaries are shown in Fig. 10, together with typical results taken from [112,81]. Agreement between RANSMB and PMB is good, as would be expected given the similarity of the methods, although RANSMB consistently predicts a slightly lower flutter speed than PMB. The agreement with experiment is good and similar to published results from other non-linear codes. There is a significant difference between computational results and the experimental measurements for supersonic flow (see for example [81,113]); RANSMB and PMB are consistent with other methods in this respect.

4.4.1. Comparison with commercial linear/non-linear methods

The time-domain methods above have been compared with commercially available packages

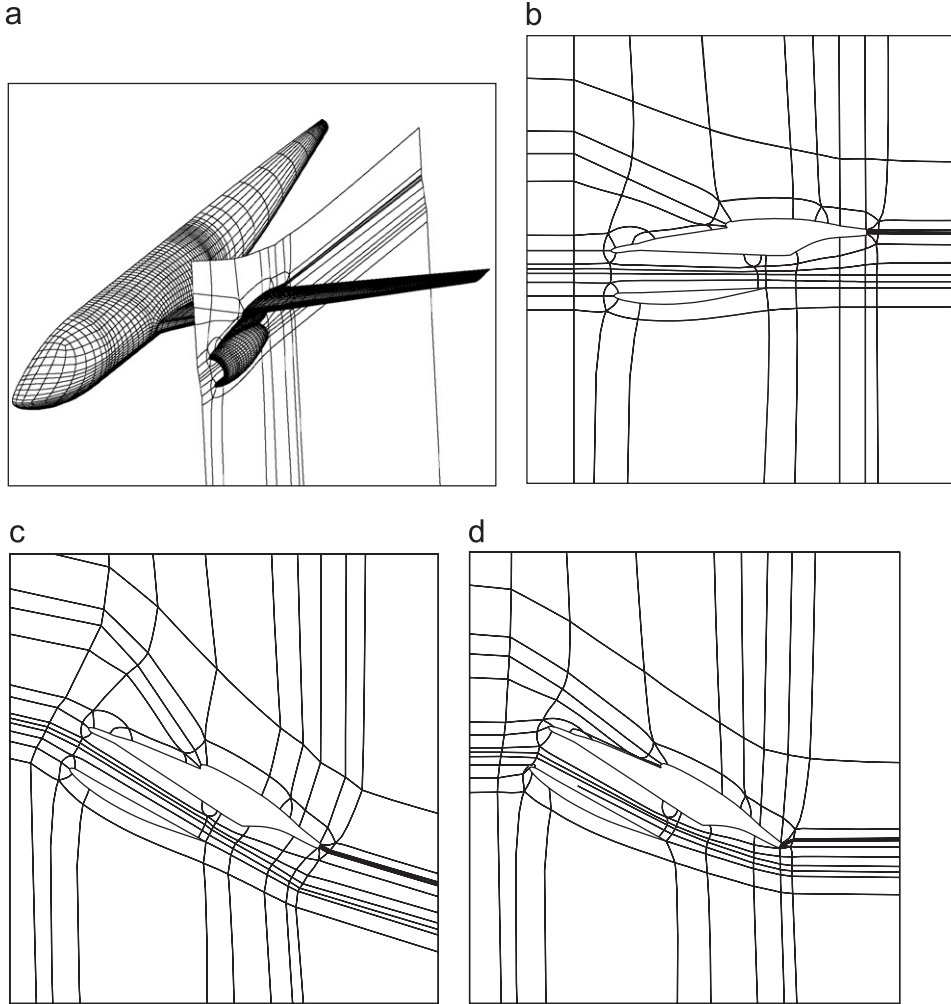


Fig. 9. Wing–Body–Pylon–Nacelle configuration: results of a 30° rigid rotation of the whole aircraft on the motion of block edges around the nacelle. Surface grid (a) and block edges for a vertical slice through the centreline of the nacelle (b), for the undisturbed grid. Block edges for a vertical slice through the centreline of the nacelle after the 30° pitch up: (c) with forcing function and (d) without forcing function.

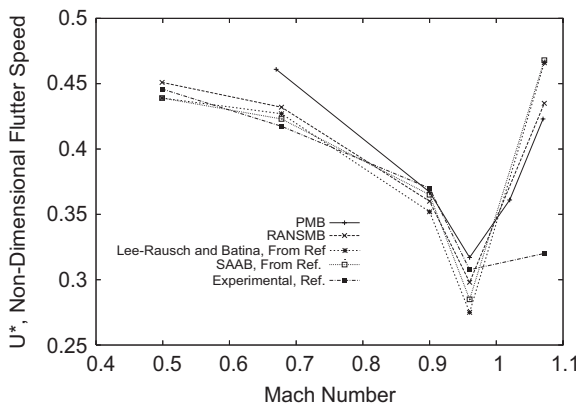


Fig. 10. Flutter boundaries, AGARD 445.6 wing.

(MSC.NASTRAN and ZAERO). Results generated by the use of the commercial packages were produced using the same structural/aerodynamic grid.

As shown in Fig. 11, the linear methods generally produce the correct overall trends, i.e. a reduction in flutter speed index with increasing Mach number, with a minimum in the non-dimensional flutter speed at a Mach number of approximately 0.9 but the flutter speed is predicted about 10% too high on average. MSC.NASTRAN and ZONA6 rely on purely linear aerodynamic models, and hence produce very similar boundaries.

ZTAIC includes compressibility effects and the improvement in prediction of the transonic dip can

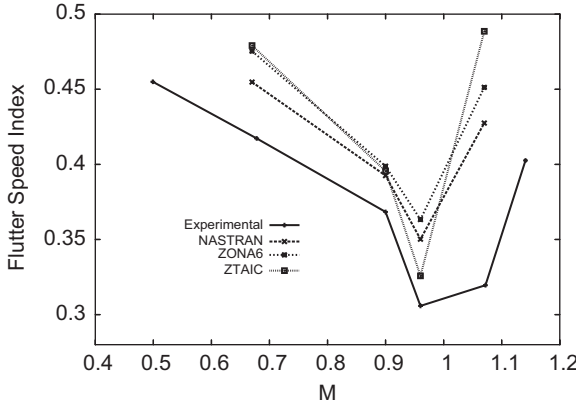


Fig. 11. Linear flutter boundaries, AGARD 445.6 wing. From Ref. [82].

be seen. The ZTAIC method differs from other commercial packages, in that it is globally non-linear, as the initial steady state flow field may be derived from a CFD solution (as in this case), or experimentally measured input. Dynamic behaviour is modelled through small perturbations from one-dimensional flow, and as such represents an approximation of the unsteady transonic flowfield. In terms of formulation and execution time, it is something of an intermediate between the rapid, but physically limited linear methods, and the more time consuming coupled codes. It is interesting to note that it is closer to the experimental value at $M = 0.96$ than either of the other two codes, and similar to that the code from which the pressure inputs were derived (PMB).

The unsteady coefficients in both ZAERO solutions (ZONA6 and ZTAIC) and MSC.NASTRAN's doublet-lattice method are produced by solving the unsteady small disturbance equation, implying a primary flow purely in the chordwise direction. This limits accuracy near the leading and trailing edges, and cannot properly allow for the effects of sweep. This introduces an error in flutter speed index across the full Mach number range. In the transonic region, an inability to account for shock waves introduces a further error, which leads to over prediction of flutter speed index in the transonic dip. This latter effect is at least partially corrected in the ZTAIC method by the use of a non-linear CFD derived flow field as input.

4.5. Treatment of control surfaces

4.5.1. Introduction

The methods discussed so far allow for the analysis of any aircraft structure that has a

continuous, smoothly varying aerodynamic surface. However, many aeroelastic responses occur due to the presence of control surfaces, which introduce a discontinuity into the aircraft surface. Simulating these components poses significant challenges, particularly since the grid types used in the current work are block structured.

The first approach is to deform a continuous mesh, i.e. the edges of the control surface are blended into the wing and so the grid connectivity is maintained [114,115]. This can be achieved simply via the transformation scheme and is considered in Section 4.5.2.

A multiblock mesh can be generated that includes 'fan' meshes, in which all the cell volumes are zero until the control surface is deflected, but this can lead to poor quality cells. Another possibility is the Chimera overlapping mesh approach developed by Steger and Benek [116], which allows the modelling of multiple, moving bodies by overlapping high-quality single block meshes. As there is no constraint of matching block boundaries, it is easier to generate and fit meshes to complex geometries. However, the information transfer from block to block is complex, requiring an expensive grid tagger and a major change to the flow solver; furthermore, conservation is difficult to maintain. These approaches were not attempted but, as an alternative to the blended treatment, it was decided to investigate a sliding grid—or non-matching block boundaries—approach as this allowed a wider range of motion. This work is discussed in Section 4.5.4.

4.5.2. Blended treatment

When blended control surfaces are used in the aeroelastic simulation the blending is easily implemented in the calculation while maintaining a reasonable grid quality, even for very large flap deflection angles. The blending of inboard and outboard flap edges is carried out using a three level hierarchical blending scheme [115]. For the flap this means that the inboard and outboard edges are driven by the wing and the flap nodes adjacent to the edge are dependent on a combination of wing and flap deformations. For example, for the rudder, the extent of the influence of the fin/fuselage on the flap depends on a blending parameter (see Section 4.3), hence the choice of the blending parameter controls the extent of blended length of the flap. The choice of the blending parameter depends on the extent of mismatch at the component interface. A very large mismatch will require a smaller absolute

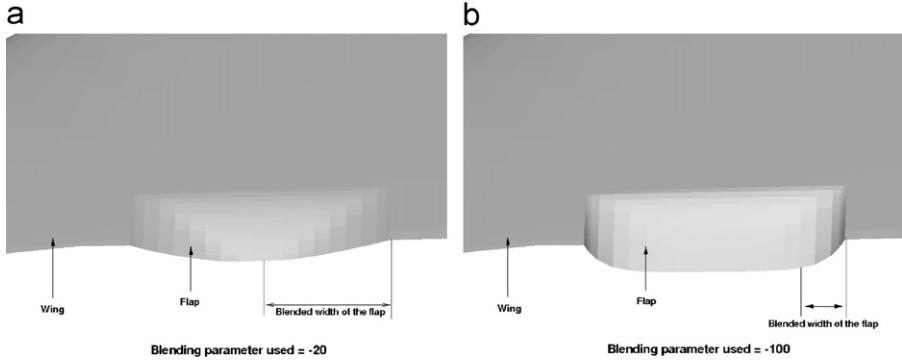


Fig. 12. Transformed flap mode using two different values of blending parameter: (a) shallow blending; (b) sharp blending.

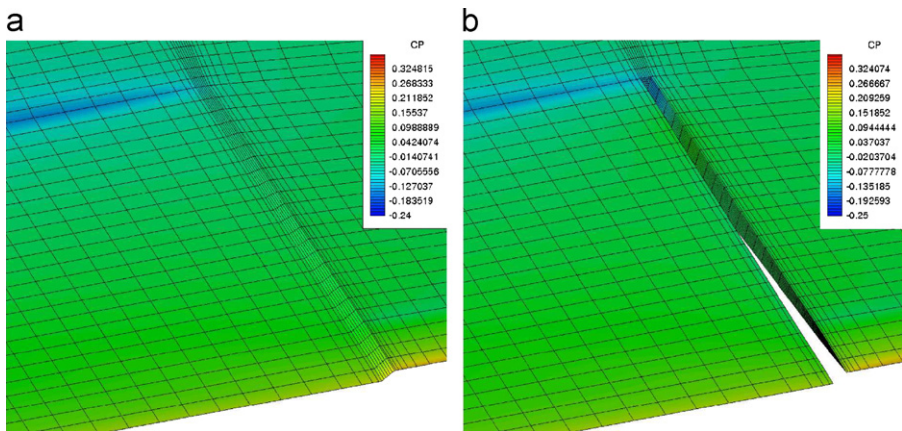


Fig. 13. The two types of modelling of the flap edges on the SST wing [117]: (a) Cp contours on a blended flap; (b) Cp contours over a flap with free edges.

value of the blending parameter which means a large area of the lower hierarchy component will be influenced by the higher hierarchy component. A larger value will limit this influence to a smaller area of the lower hierarchy component, as shown in Fig. 12.

4.5.3. SST

In this section we present results to investigate the performance of the blended wing treatment for an arrow wing test case. This is a summary of detailed results which appear in Refs. [117–120].

The Japanese Aerospace Exploration Agency (JAXA) flew an unpowered supersonic transport (SST) model aircraft in 2002 as part of a programme to develop technology for a future SST passenger aircraft. Wings for SST aircraft are likely to be thin, making it difficult to have stiff hinges or powered actuators for trailing edge flaps. Buzz therefore becomes a concern, particularly due to shock motions over flaps.

Work was done using an SST wind tunnel configuration developed by JAXA to advance the computational aeroelastic simulation methods for trailing edge flaps. First, forced flap motions were imposed for a flexible wing. Data from wind tunnel tests are available to validate the wing structural and aerodynamic response. A number of issues were investigated regarding the flap treatment in the simulation. Next, self-excited flap motions were studied.

The flap is modelled as a separate plate attached to the main wing through springs. Two structural models were constructed using the same material and geometric properties. The difference between the two models is in the value of the spring stiffness at the flap hinge. The spring stiffness constant in Model 1 is adjusted so that it gives a flap frequency of 16.2 Hz which is within the realistic frequency range of a mechanically constrained trailing edge control surface. The spring stiffness constant of the hinge in Model 2 is set very high so that the flap is

constrained and the flap mode is eliminated. By increasing the stiffness of the flap hinge the flap oscillation mode was eliminated at the same time maintaining the shape and frequencies of other modes. The wing structure is made up of 550 triangular elements and the flap has 20 elements. The fuselage structure consists of two triangular elements that are clamped rigid.

To model the effect of gaps and viscosity a total of four different grids have been used in this work. Viscous calculations are performed with only blended flaps. There are 14 cells in the chordwise direction and 28 in spanwise direction on the flap. The size of the viscous grid is 800k cells. The grid is capable of accurately resolving the flow in the region of interest but at the same time is small enough to allow rapid turn around for the unsteady calculations. The fine Euler grid has 1.6 million cells. There are 24 cells in the chordwise direction and 50 spanwise on the flap. A coarse grid is obtained from the fine grid by removing every alternate grid point in all the three directions. The coarse Euler grid has 200k cells. An extra grid was generated with a gap between the flap edges and the wing. This has the same resolution as the coarse Euler grid for blended flaps. The blended and gap treatments of the flap are shown in Fig. 13.

Results were obtained for various mean angles of incidence, flap amplitude, Mach number and, flap oscillating frequency. One set of results will be shown here, namely for Mach 0.8, zero mean incidence and a flap amplitude close to 1°. The flap frequency is varied from 10 to 25 Hz in 5 Hz steps. At a frequency of 15 Hz the flap oscillation was observed to couple with the first wing bending mode, resulting in a more energetic wing response. A time step sensitivity study showed that a smaller time step was needed for 15 Hz forced motion, when the resonance takes place. Grid refinement showed that the response and pressures were well represented on the coarse Euler grid. Also, the Euler and

RANS predictions for this case, when the shock is not close to the trailing edge, are very similar.

Pressures were measured at 38% and 74% of wing span and a Fast Fourier Transform used to obtain the unsteady pressure coefficients. Unsteady deflections were obtained along a line extending from the fuselage. These measurement locations are shown in figure 14. The comparison between computations and measurements is shown in figure 15 and the agreement is good. The larger response at 15 Hz is clear from the figure. Similar levels of agreement were obtained at other conditions.

The influence of the treatment of the flap was investigated and results are shown here for a mean incidence of -2° . The comparison of response is shown in Fig. 16 and shows close agreement between the results for the blended and gap treatments. These and similar results in the current study suggest that the blended treatment (which is simpler) is adequate for this type of calculation.

We now turn to the self-excited response of a flap, and in particular when a shockwave goes onto the flap. The flap attachment is weakened to give a natural frequency of oscillation for the flap of 16.2 Hz. No validation data are available.

The influence of the flap grid treatment was investigated again since the local aerodynamics on the flap would be expected to be more influential on buzz than in the forced motion cases. Again the coarse Euler grid was used to investigate this issue. The degree of blending was found to influence the results. First the flap was blended into the wing sharply (i.e. following the real flap position until close to the flap edge). Allowing a more gradual blending was seen to damp out the flap response. Two examples of the blending are shown in Fig. 12. The stronger blending (Fig. 12(b)) gives results that are reasonably insensitive to further sharpening, i.e. sharper blending implies greater geometric integrity. This blended case was then compared with having

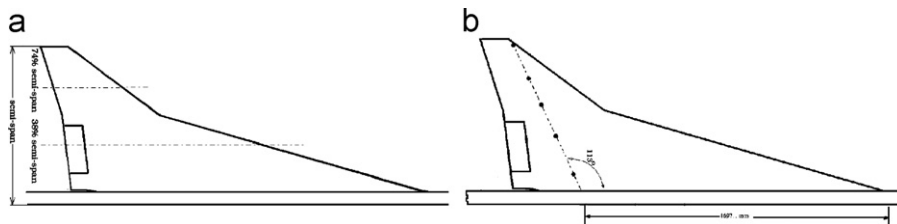


Fig. 14. Location of measurement points in the SST experiments: (a) location of unsteady pressure transducers; (b) location of optical targets to measure dynamic deformation.

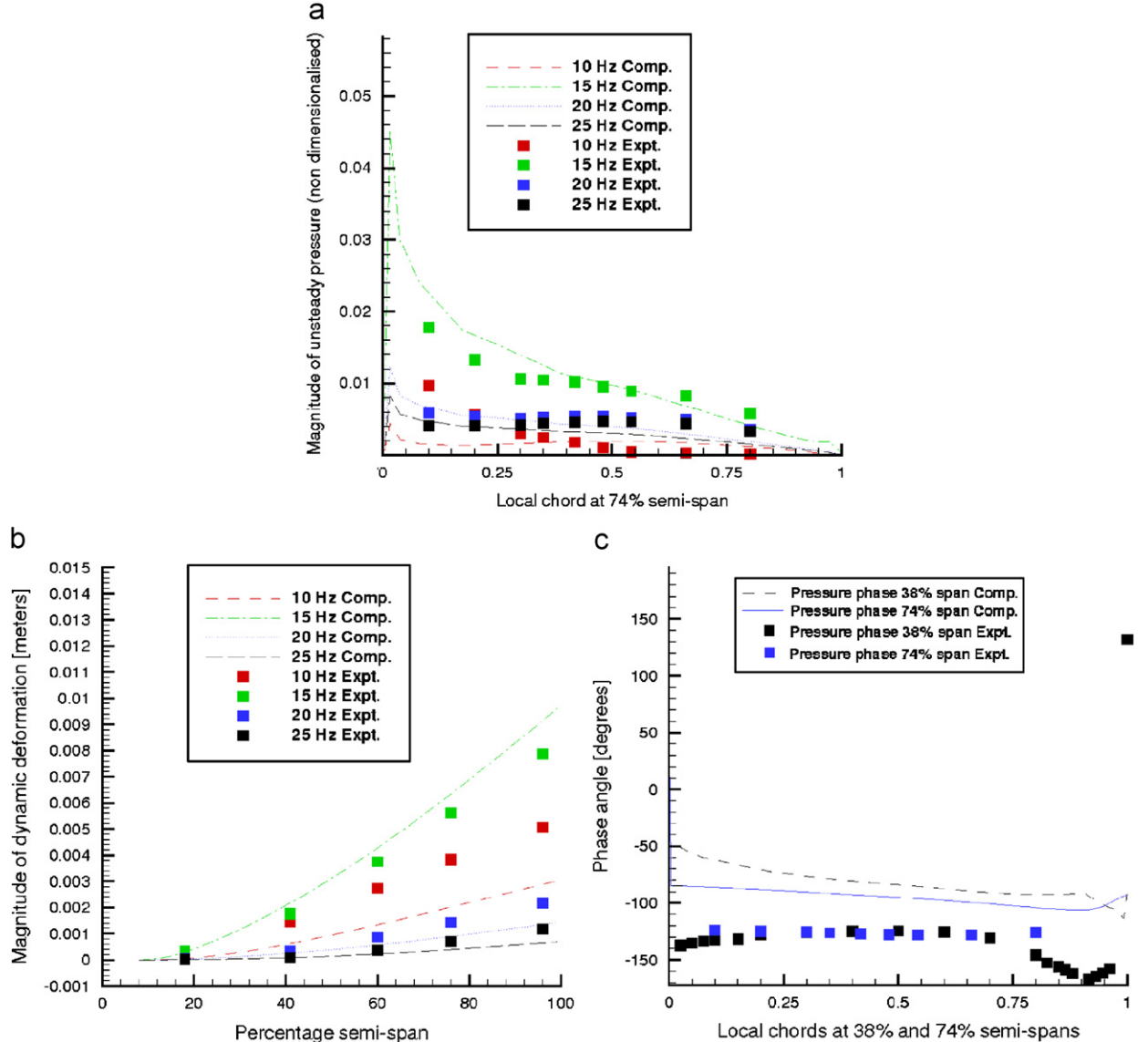


Fig. 15. Unsteady pressure and deformation plots for SST Case 1 computations on a coarse grid using Euler equations [117]: (a) unsteady pressure at 74% semi-span location; (b) unsteady deformation along the span (see Fig. 14); (c) pressure phase lag at the FOF of 15 Hz.

gaps at the flap ends. The comparison for a damped and an LCO response is shown in Fig. 17. The buzz onset angle was not altered much and there is a marginal increase in amplitude of oscillation for the blended case due to the larger area covered for the flap.

The influence of viscous effects was then examined. The mean shock location was previously known to be critical to the loss of stability. If the incidence is used to match mean shock locations between the viscous and Euler results then the buzz

behaviour is similar. In the viscous case the appearance of separation at higher flap angles reduces the limit cycle amplitude.

Finally, and most interestingly, there is a dependence of the buzz behaviour on the initial kick given to the flap to initiate the response. For some Mach numbers and angles of incidence, if the initial kick was large enough that a strong shock formed on the flap then an LCO could be sustained. If this was not the case then a damped response results. A buzz response is shown in Fig. 17.

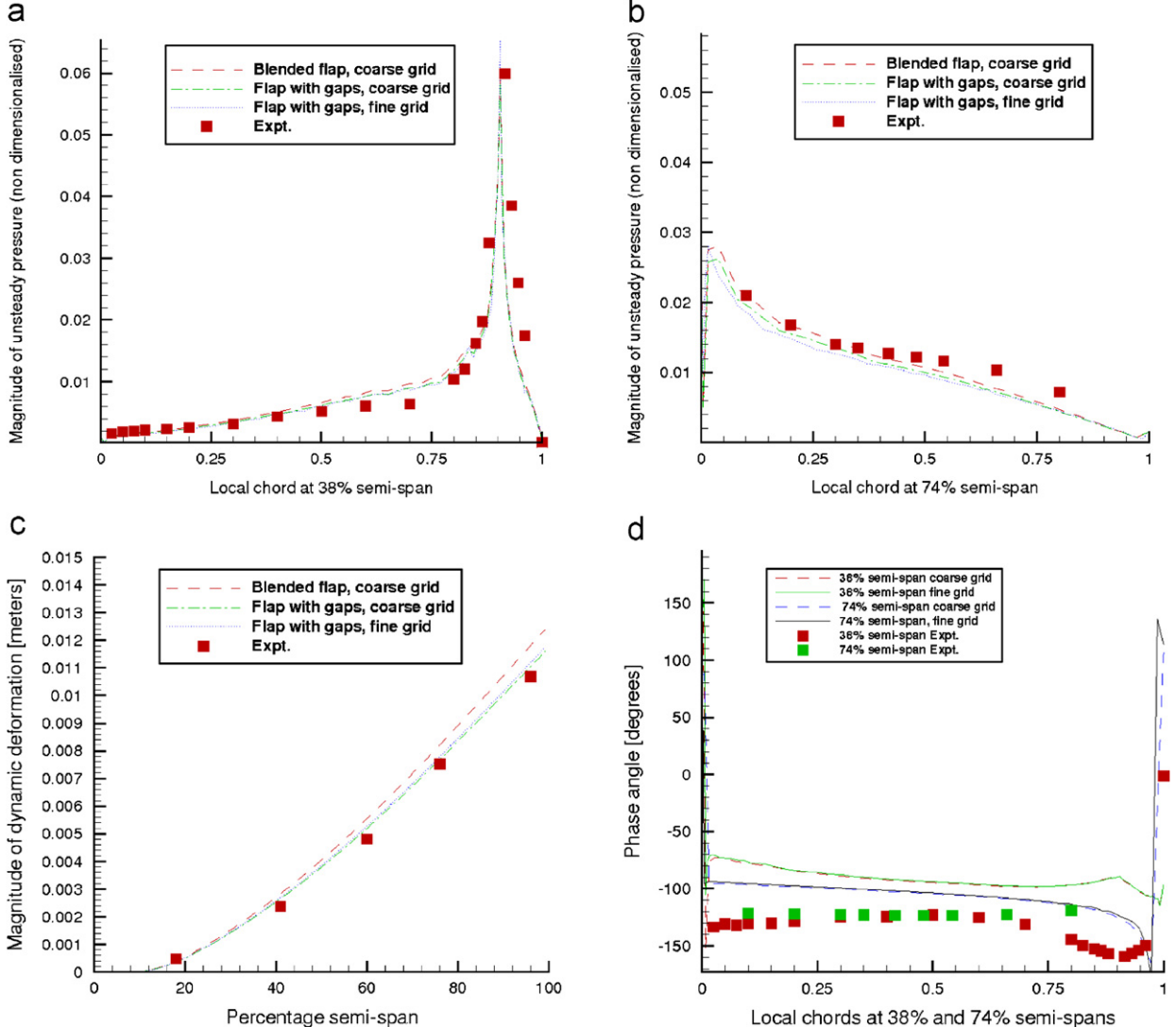


Fig. 16. Unsteady pressure and deformation plots for the SST Case 2 computations on a coarse and fine grids using flaps with gaps and at FOF of 15 Hz using the Euler equations [117]: (a) unsteady pressure at 38% semi-span location; (b) unsteady pressure at 74% semi-span location; (c) unsteady deformation along the span (see Fig. 14); (d) pressure phase lag of fine and coarse grids with at the FOF of 15 Hz.

4.5.4. Sliding mesh treatment

Sliding meshes are an extension of patched grids, whereby blocks have common interfaces, but non-matching grid nodes along the boundaries. The allowance for discontinuity across grid boundaries also enables the use of isolated mesh refinement and clustering of cells. Tang and Zhou [121] present a non-conservative method for generating boundary conditions, but the general consensus is for conservative treatments to ensure the correct prediction of shocks. Berger [122] presents a general formulation of conservative boundary conditions for discontinuous grids, whether in space,

time or a change in scheme. A more specific example of Berger's flux interpolation method is proposed by Rai [123,124]. Rai uses one-sided flux interpolation where the interface condition for one block is defined by the numerical fluxes, the other for the neighbouring block by the conservative variables. A slightly different approach is taken by Lerat and Wu [125] who use a flux-splitting method which is linearly equivalent to an area-weighted interpolation. Bohbot et al. [126] extend this method for use with a Navier–Stokes solver, and sliding meshes, for full three-dimensional aircraft configurations.

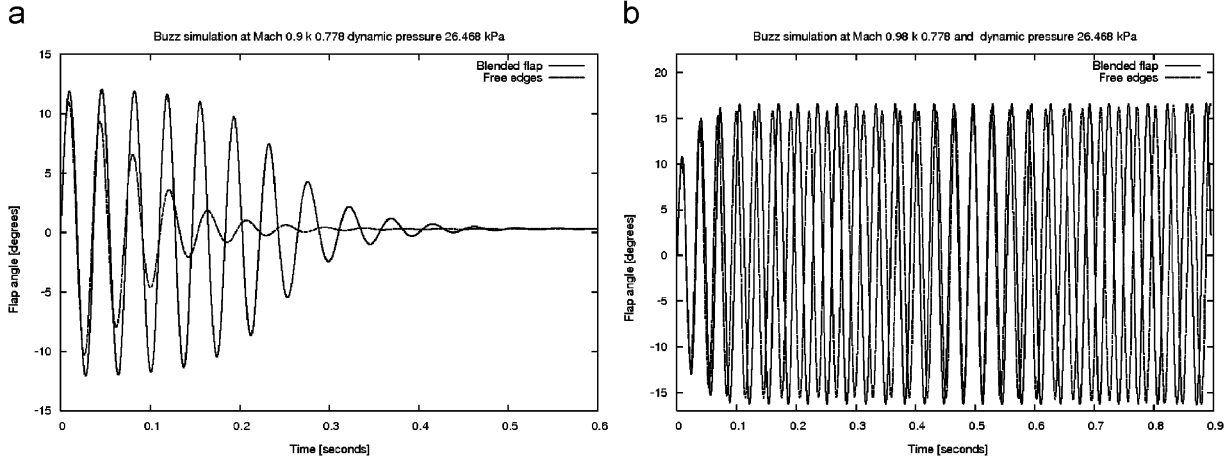


Fig. 17. Flap response of blended and free flaps at different Mach numbers [119].

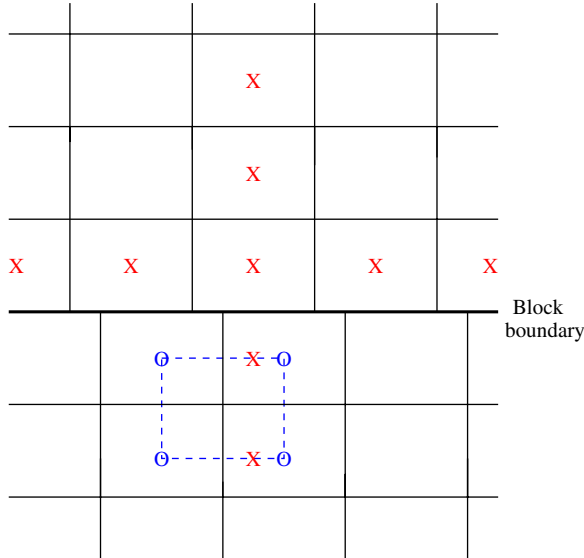


Fig. 18. Patched grid with halo cell-centre positions.

In this section, methods of information transfer across sliding and non-matching boundaries are presented, the aim of which is application to the case of a wing with a moving control surface. Two methods are discussed and tested; halo cell interpolation and a conservative flux interpolation method. Consider the two-dimensional patched grid boundary shown in Fig. 18. In order to complete the five point stencil required by the solver, two halo cells must be computed (marked as the two crosses in the lower block). Halo cells may not simply assume the positions and values of neighbouring cells, as is the case for basic internal block boundaries, and an interpolation method is needed.

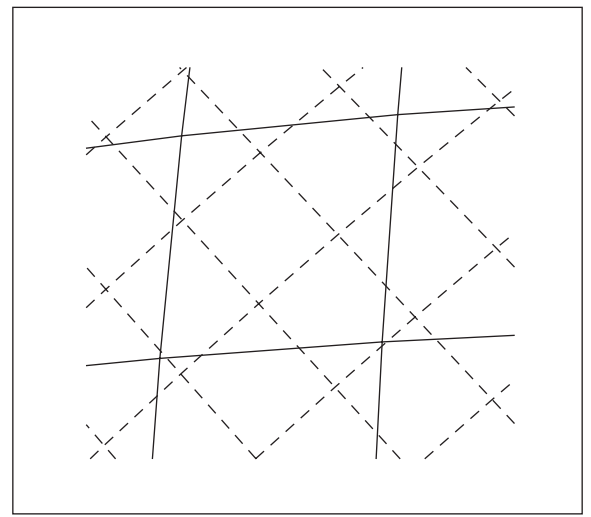


Fig. 19. Example of three-dimensional patched grid boundary.

The halo cell positions are determined by computing internal cell-centre positions across the block boundary and a search is made for the closest grid point in the neighbouring block to the calculated halo position. The four cell-centre values surrounding this closest grid point (seen in Fig. 18) are bilinearly interpolated to determine the values of the halo cell solution. Interpolation coefficients are calculated by converting grid positions into computational space. This halo cell interpolation is easily extended for three-dimensional meshes where eight cell centres, rather than four, are required around the closest grid point in the neighbouring block. These are trilinearly interpolated to determine the values of the halo cell solution.

The halo approach shown is not strictly conservative, i.e. the total flux integral along a sliding boundary from values computed on one side may not equal that from the values computed on the other side. In an effort to make this information transfer conservative, fluxes can also be interpolated across the boundary, as well as the conserved variables. This is performed as a one-sided interpolation, following the direction of flow or from a fine to a coarse mesh.

Consider the three-dimensional example, shown in Fig. 19, of a sliding boundary. Every cell has a calculated flux through each of its faces. In addition to the halo cell interpolation, the desired flux $\mathbf{F}_{i,j}$ through the boundary cell face (marked by solid lines) is calculated using an area-weighted function of the fluxes of coincident cell faces from the neighbouring block. This relationship may be described by

$$A_{i,j} \mathbf{F}_{i,j} = \sum_{s=1}^S A_{int_s} \mathbf{F}_s, \quad (10)$$

where $A_{i,j}$ is boundary cell face area, S is the total number of coincident faces and A_{int_s} is the associated intersecting cell face area from the neighbouring block.

The difficulty of this method lies in determining the intersecting cell faces and corresponding intersection areas. Initially, a search is made in the blocks on the other side of the sliding boundary for the closest grid point and cell centre to the current boundary cell centre. Within this vicinity, a search is made for any intersecting cell faces. First, a search is made along each of the four edges of the current face for any intersecting cell edges from the

neighbouring sliding block, and their i and j index values recorded. A search is also made for any matching or coincident nodes, so the method works for all cases, matching or non-matching. These intersecting edges are marked in Fig. 20(a) in bold.

Using these intersections, one can determine how many and which nodes lie on the current face. These nodes are used to calculate the perimeter of each face intersection area. Consider an arbitrary point or node 1 on a cell face, as pictured in Fig. 20(b). Starting from this point, a clockwise path is followed along the cell edge until another corner or an intersection with another cell edge is encountered, recorded and marked as point 2. The path now moves in a new direction along the intersecting edge until a new corner or intersection is found. This process is repeated until a return to point 1. Having now obtained the perimeter, it is possible to calculate the intersection area of this intersecting cell face. This search is repeated for all the other nodes located on the required face, always working in a clockwise direction to avoid duplication of areas. An extra search is made to include any intersecting areas with corresponding nodes lying outside of the current face.

This method is applied to all intersecting cells. The entire procedure is extremely complex, particularly when crossing other block boundaries, and demands a significant computational overhead relative to the halo method. Tests performed on a variety of aerodynamic cases found that any differences in results using either halo or flux interpolation were negligible. Despite the halo interpolation method being non-conservative, it was used in further computations due to its faster

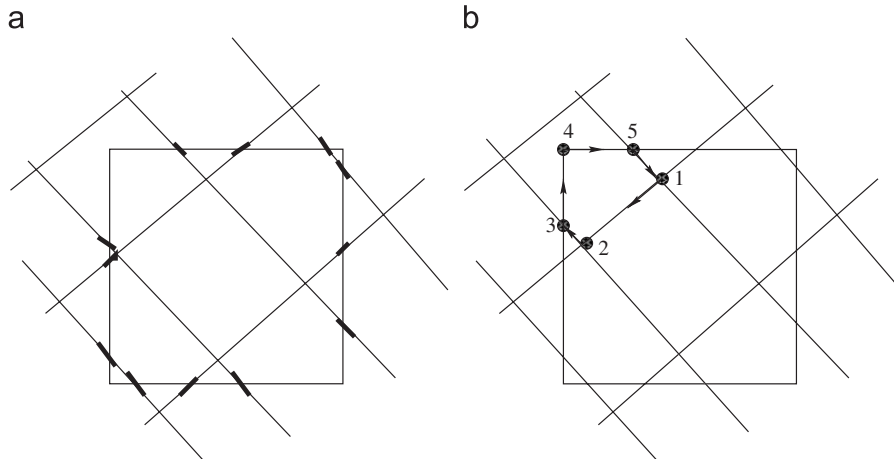


Fig. 20. Three-dimensional flux interpolation methodology: (a) face edge intersections; (b) determining area perimeters.

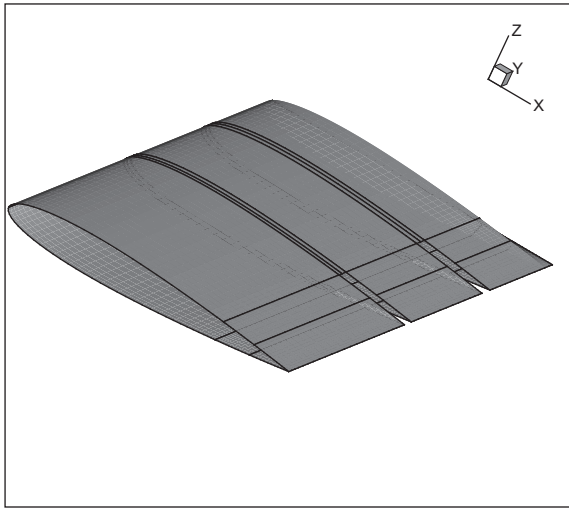


Fig. 21. View of three-dimensional wing and control surface blocking.

run time, relative ease of implementation and comparable accuracy.

4.5.5. BACT wing

The Benchmark Active Controls Technology (BACT) wing (Table 5) was used for validation of the sliding plane methods, as it represents one of a very few experimental attempts to examine the aeroelastic and aeroservoelastic behaviour of a wing with control surfaces. Results are compared with those computed using a blended mesh treatment, as considered above. The work presented is a summary of that found in Refs. [127,128], and aeroelastic analyses can be found in Refs. [129,130].

In order to use the sliding plane methodology, a gap is generated between the wing and the side of the control surface as shown by the surface blocking in Fig. 21, where each gap either side of the flap is two blocks wide. This gap was created in the first instance, to avoid the problem of ‘new’ grid cells appearing in the flow, on the edges of the control surface as it was deflected, which causes another grid cell identification problem. As the flap moves, the blocks directly touching either end move with it, creating a discontinuous surface between the wing side grid and flap grid. The model chosen for study is the BACT model [84,85], which was part of the Benchmark Models Program at NASA Langley Research Centre. The primary objectives of the BACT experiments were to further validate unsteady CFD and aeroelastic codes with the inclusion of a trailing edge flap and spoilers, and to study the

behaviour of the control surfaces, ultimately for the design of active control laws. Therefore the BACT wing is a suitable choice for the current investigation, although only the trailing edge flap is considered. This wing has an aspect ratio of two with NACA0012 section and control surface occupying 30% span.

Steady aerodynamic results have been obtained for a wing with a deflected flap in the transonic region (freestream Mach 0.77), using both sliding and blended meshes. The halo interpolation method has been tested on a range of angles of incidence (α) and flap angle (β). Figs. 22 and 23 compare the Mach contours and surface pressure coefficients computed using RANSMB for a wing with $\alpha = 2.5^\circ$ and $\beta = 5.0^\circ$, using a gap mesh and a blended mesh. Excellent agreement is shown between the two sets of results, apart from in the gap where there is some periodic separated flow for the patched mesh, as expected. Fig. 24 shows surface pressure coefficients for a wing at $\alpha = 0.0^\circ$ and $\beta = 10.0^\circ$. Again, it is clear that the presence of the gap does not unduly affect the flow. Inside the gap is an area of almost zero velocity flow, and the solution in this region is reasonable considering that an inviscid solver is attempting to solve a viscous-type region.

However, although the results are qualitatively the same whether using a blended or sliding grid, there is a difference between lift coefficient variations. The results are compared to aerodynamic data obtained for the BACT wing [85] in Table 9. The sliding mesh approach predicts a slightly lower lift derivative than the blended mesh approach due to gaps between the wing and the flap which reduce the overall surface area and allow flow through them, and hence reduce lift. As a result, derivatives calculated using the sliding mesh are closer to experimental data [84,85] due to the more realistic physical representation.

A forced motion case was also performed to further compare the blended and sliding approaches. The simulation was started from a steady state solution at an incidence of 1.25° and $M = 0.77$, and the flap allowed to oscillate sinusoidally with an amplitude of $\pm 4.0^\circ$ and a reduced frequency of $k = 0.08$. The C_L response is shown in Fig. 25. It is clear that the blended mesh approach has a noticeably higher $\partial C_L / \partial \beta$ than the sliding mesh approach, as was reported for the steady aerodynamic simulations.

Static aeroelastic calculations were performed for a range of incidences and flap deflections. First, a

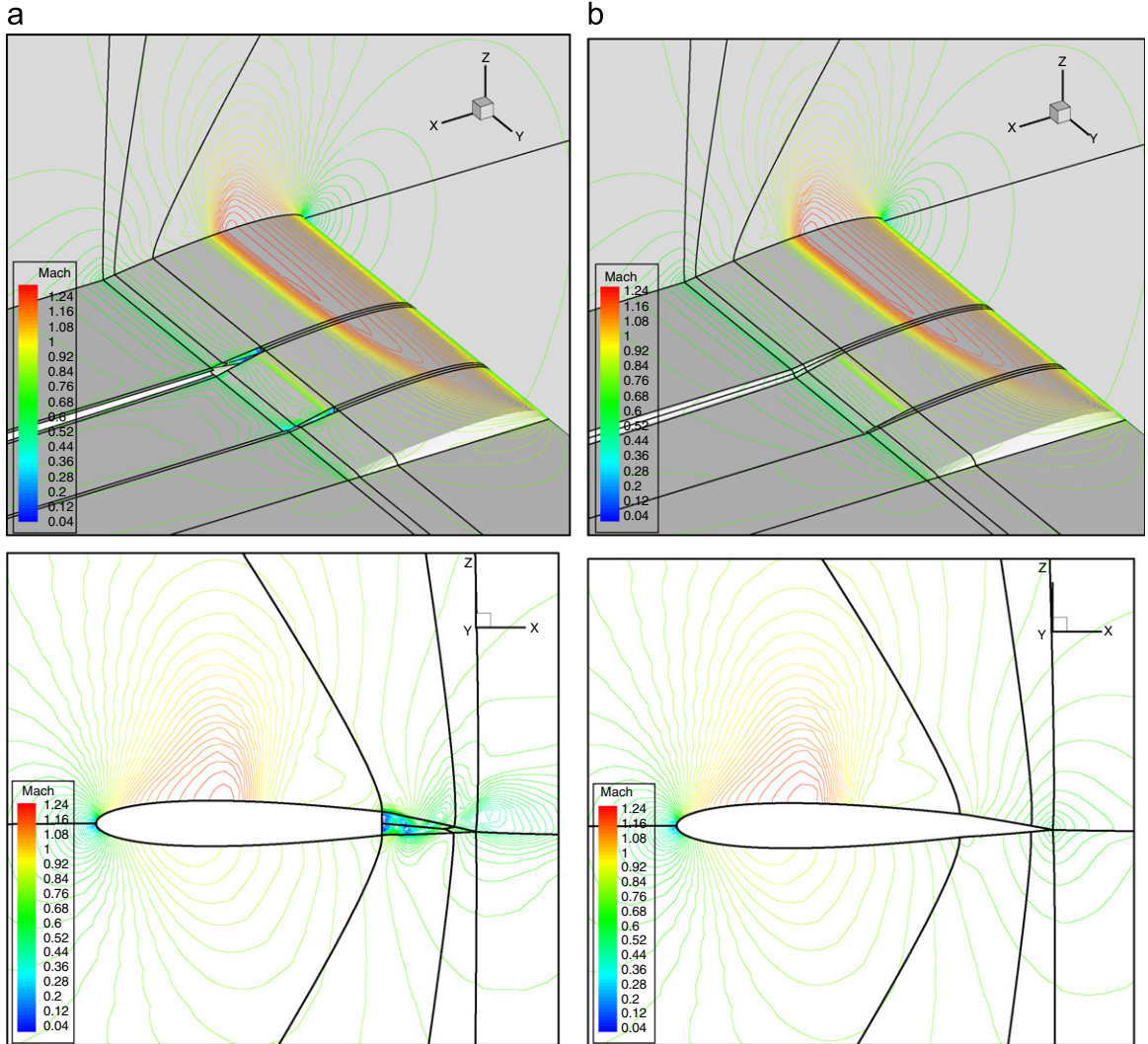


Fig. 22. Mach contours for $\alpha = 2.5^\circ$, $\beta = 5.0^\circ$, aerodynamic results: (a) patched; (b) blended.

steady base solution was computed for a rigid wing with zero flap deflection using the aerodynamic solver. In order to obtain the aeroelastic solution, the modal structural model was then coupled with the aerodynamic model and a simulation was run from the steady base solution. A control law was used to move the flap to the desired deflection and the aeroelastic simulation continued until equilibrium was reached between the structural and aerodynamic forces, i.e. the wing ceases to move and settles into a final, steady position. Artificial damping was added to reduce the time taken to reach equilibrium. Fig. 26 shows an example at Mach 0.77, with incidence of 2.5° and flap deflection of 5° . Once again, although the two approaches produce similar results, those of the sliding mesh

approach are more realistic in the region of the flap (see Fig. 26(a)).

4.5.6. Conclusions

Representation of control surfaces for use in aero-structural coupled simulations has been considered, using the SST and BACT wings for comparison. Aerodynamic and aeroelastic results have been obtained for a range of wing incidence and flap deflection, using sliding, gap and blended meshes. It was found that control surfaces can be modelled using either representation. Although qualitatively the same, results suggest that the sliding plane approach is more accurate and closer to experimental data, due to a more realistic physical representation. However, in most cases

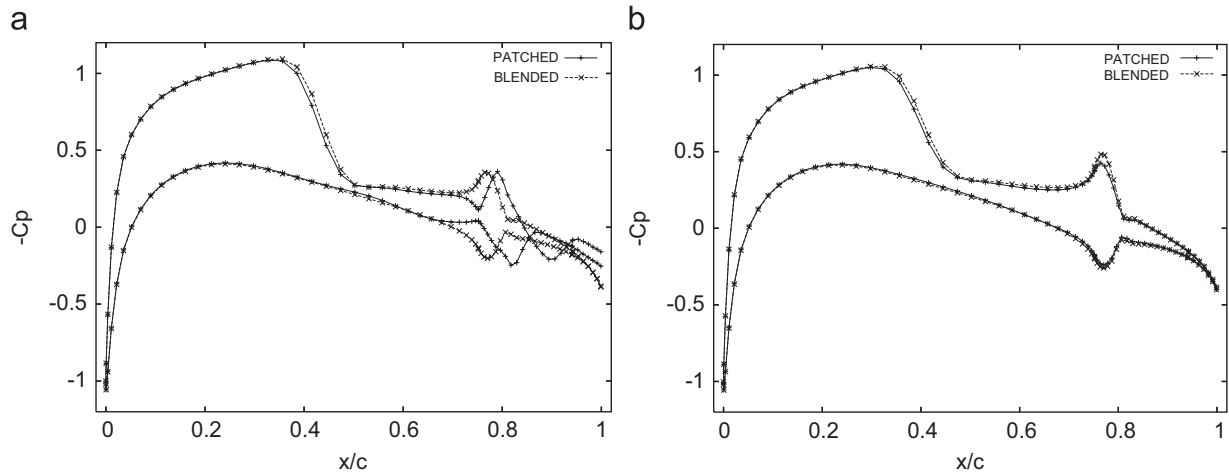
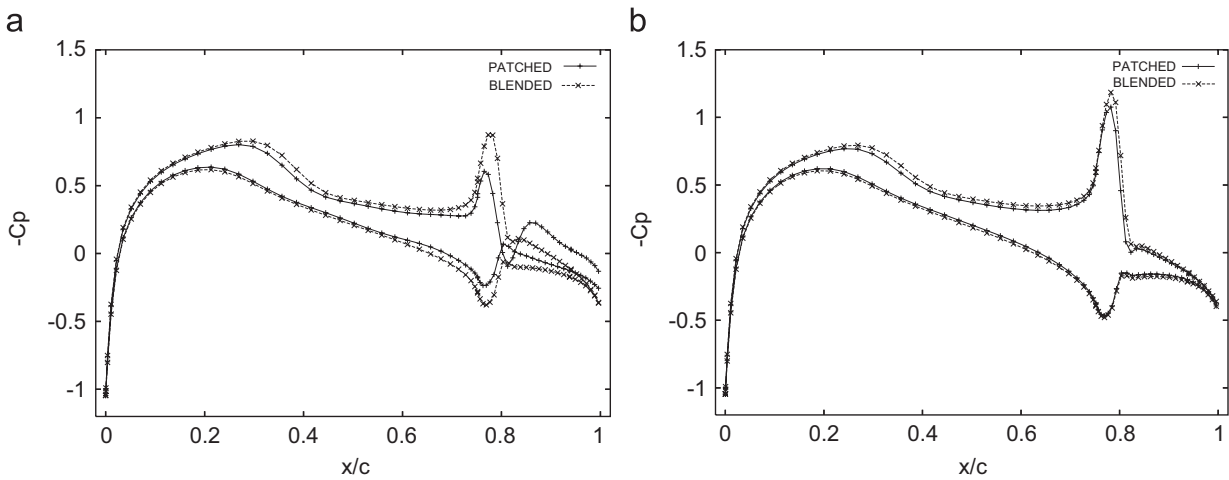
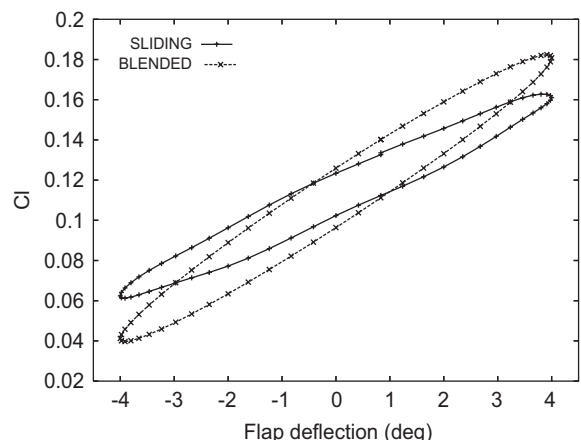
Fig. 23. Surface pressures for $\alpha = 2.5^\circ$, $\beta = 5.0^\circ$, aerodynamic results: (a) 45% span; (b) 60% span.Fig. 24. Surface pressures for $\alpha = 0.0^\circ$, $\beta = 10.0^\circ$, aerodynamic results: (a) 45% span; (b) 60% span.

Table 9
Comparison of lift curve slopes

	$\delta C_L/\delta\alpha$ per rad	$\delta C_L/\delta\beta$ per rad
Wind tunnel data	4.584	0.63
Gap mesh	4.904	0.83
Blended mesh	4.973	1.01

considered the blended wing produces acceptable results and is easier and quicker to implement and run. Future work would involve further investigation into the effect of larger flap deflections, and viscous effects such as vortices forming off the trailing edge, for which sliding gap meshes may have more advantages.

Fig. 25. C_L histories with oscillating flap comparing gap and blended mesh.

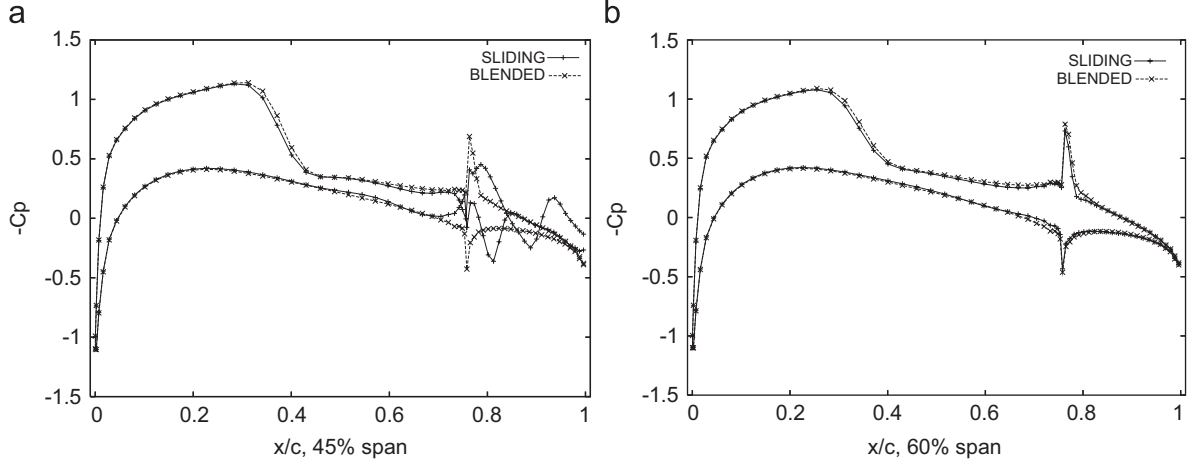


Fig. 26. Surface pressures for $\alpha = 2.5^\circ$, $\beta = 5.0^\circ$, static aeroelastic case: (a) 45% span; (b) 60% span.

5. Fast flutter prediction—prediction methods for non-linear aeroelasticity

The time-domain methods of the preceding section have demonstrated accurate non-linear prediction both within this programme, and elsewhere. But, despite significant improvements in efficiency in recent years, such methods still remain too costly for the routine prediction of the flutter boundary, providing, instead, effective tools for examining specific problem conditions. Non-linear methods that can search the entire flight envelope for instability conditions require different approaches if affordable tools are to be developed. In this section, we describe approaches considered within PUMA and indicate those that have been validated sufficiently for deployment within the industrial environment.

5.1. Overview

Non-linear systems can undergo a wealth of different types of bifurcation to self-excited vibrations. Such bifurcations include not only sub-critical and super-critical Hopf but also folds, period doubling, secondary Hopf, chaos, and others. While most researchers in non-linear aeroelasticity have focused on the Hopf bifurcation, it is clear that other types of bifurcation can occur in aeroelastic systems. For example, systems with freeplay cannot undergo Hopf bifurcations. Therefore, the development of methodologies that can predict a variety of bifurcation types for non-linear aeroelastic systems

is potentially relevant. Until recently most of this work has been carried out on systems of academic interest, such as the pitch-plunge airfoil [131] and the Hancock wing model [132,133].

CFD based simulation of behaviour, such as the results shown above for control surface buzz are impressive and encapsulate the important physics. But, the cost is high and this motivates a desire to retain the modelling whilst reducing the computational time. This leads to the problem which is addressed in the next section, namely large dimension models that are likely to behave in a predictable way (e.g. damped response, LCO).

5.2. Dynamically linearised CFD approaches—ROMSI

5.2.1. Introduction

The objective of system reduction methods is to identify a lower dimension model (ROM) from a full system of equations in such a way as to retain a reasonable accuracy. System reduction methods have been used with success in other fields of engineering and the research reported here seeks to apply such a technique to fluid modelling.

In this section the flow under investigation is assumed to be statically non-linear, but dynamically linear. These assumptions mean that the unsteady CFD equations form a linear system which can be written in state-space form. Whilst many reduction methods can be directly applied to the matrices of the large linear system of equations (e.g. ERA (modified Ho algorithm) [134,135], POD [136],

Krylov-subspace [137], Arnoldi [138,139]), in fluid dynamics it has been more common to create ROMs in the discrete frequency or discrete-time domain using methods that do not require explicit construction of the system matrices. This is because in general for most CFD codes neither the continuous nor the discrete system matrices are ever explicitly constructed. Instead the CFD code solves either a discrete frequency or discrete-time approximation to the continuous-time set of equations (obtained after spatial discretisation); the ROM initially produced is therefore itself a discrete frequency or discrete-time model.

Reduced systems have then been found by a number of techniques when the flow is assumed harmonic with a discrete frequency, most prominently via eigenmode summation and proper orthogonal decomposition [47]. Eigenmode summation has been used to reduce the Euler equations [48]. However, the application of proper orthogonal decomposition is increasingly investigated with models constructed for the Euler equations by Hall et al. [49,50]. Further improvements via balanced proper orthogonal decomposition have also been obtained [51].

The approach developed here uses a discrete-time implementation of the continuous-time CFD equations to identify the discrete-time pulse responses of the system, which characterise all solutions of the dynamically linear system [63,64,140,141]. These responses are then used with the ERA [134], which is a balanced reduction method, to generate a discrete time reduced order system (discrete ROMSI). A continuous-time model (continuous ROMSI) can be derived from the discrete-time system. Advantages of ROMSIs generated using this approach are

- they can be derived with minimal work from an existing CFD code;
- the continuous ROMSIs can be used with varying time steps which allows coupling to structural models with discrete non-linearities (such as freeplay [142]);
- the ROM is only dependent on the surface displacements used as pulse inputs to identify the model.

The statically non-linear mean or base solution is found by running the non-linear CFD code. The dynamically linear pulse responses about the non-linear mean are then found using a time-linearised version of the unsteady moving mesh code.

5.2.2. State-space models of the CFD code

The continuous linearised version of the CFD equations about a non-linear mean is written in continuous state-space form as

$$\begin{aligned}\dot{\mathbf{x}}(t) &= \mathbf{A}\mathbf{x}(t) + \mathbf{B}\mathbf{u}(t), \\ \mathbf{y}(t) &= \mathbf{C}\mathbf{x}(t) + \mathbf{D}\mathbf{u}(t),\end{aligned}\quad (11)$$

where \mathbf{A} , \mathbf{B} , \mathbf{C} and \mathbf{D} are the system matrices, \mathbf{u} is the input vector, \mathbf{x} is the state vector and \mathbf{y} is the output vector that is defined to produce the required information about the system.

The inputs are defined as the set of surface displacements and corresponding surface speeds that characterise the motion of interest. In this work, the structural models to be coupled with the ROMSIs are modal. For modal applications the inputs are defined as the set of surface displacements and speeds corresponding to each mode. For these aeroelastic systems the required output is the modal force.

The continuous system (11) is put into a discrete form using a first order finite difference approximation which acts as a filter to remove the high frequency eigenvalues from the pulse responses

$$\begin{aligned}\frac{\tilde{\mathbf{x}}_k - \tilde{\mathbf{x}}_{k-1}}{\Delta t} &= \mathbf{A}\tilde{\mathbf{x}}_k + \mathbf{B}\tilde{\mathbf{u}}_k, \\ \tilde{\mathbf{y}}_k &= \mathbf{C}\tilde{\mathbf{x}}_k + \mathbf{D}\tilde{\mathbf{u}}_k,\end{aligned}\quad (12)$$

where $\tilde{\mathbf{x}}$, $\tilde{\mathbf{u}}$ and $\tilde{\mathbf{y}}$ are discrete approximations to the state, input and output vectors, respectively.

On rearranging this becomes

$$\begin{aligned}\tilde{\mathbf{x}}_k &= \tilde{\mathbf{A}}\tilde{\mathbf{x}}_{k-1} + \tilde{\mathbf{B}}\tilde{\mathbf{u}}_k, \\ \tilde{\mathbf{y}}_k &= \tilde{\mathbf{C}}\tilde{\mathbf{x}}_k + \tilde{\mathbf{D}}\tilde{\mathbf{u}}_k,\end{aligned}\quad (13)$$

where the discrete system matrices are given by

$$\begin{aligned}\tilde{\mathbf{A}} &= (\mathbf{I} - \mathbf{A}\Delta t)^{-1}, \\ \tilde{\mathbf{B}} &= (\mathbf{I} - \mathbf{A}\Delta t)^{-1}\mathbf{B}\Delta t, \\ \tilde{\mathbf{C}} &= \mathbf{C}, \\ \tilde{\mathbf{D}} &= \mathbf{D}.\end{aligned}\quad (14)$$

To simplify the process of obtaining a ROM of the system, the system output is modified. Since \mathbf{D} (and thus $\tilde{\mathbf{D}}$) are known matrices, both the continuous system and the discrete approximation use a modified output, by subtracting the term $\mathbf{D}\mathbf{u}(t)$ from the continuous output and the term $\tilde{\mathbf{D}}\tilde{\mathbf{u}}$ from the discrete output equation. The modified discrete system is then

$$\begin{aligned}\tilde{\mathbf{x}}_k &= \tilde{\mathbf{A}}\tilde{\mathbf{x}}_{k-1} + \tilde{\mathbf{B}}\tilde{\mathbf{u}}_k, \\ \tilde{\mathbf{y}}_k^m &= \tilde{\mathbf{y}}_k - \tilde{\mathbf{D}}\tilde{\mathbf{u}}_k = \tilde{\mathbf{C}}\tilde{\mathbf{x}}_k.\end{aligned}\quad (15)$$

This can be solved using one-sided z -transforms [143,144] to give the output equation

$$\tilde{\mathbf{y}}^m(k) = \sum_{n=0}^k \mathbf{H}_{k-n} \tilde{\mathbf{u}}_n. \quad (16)$$

The matrix \mathbf{H}_k is composed of columns which are the outputs for a unit sample pulse on each separate input, i.e. the i th column is the output vector at time k for a unit sample input in the i th component of $\tilde{\mathbf{u}}$ with all other entries of $\tilde{\mathbf{u}}$ set to zero, see Aplevich [145].

The sequence

$$\{\mathbf{H}_0, \mathbf{H}_1, \mathbf{H}_2, \dots, \mathbf{H}_k, \dots\} = \{\tilde{\mathbf{C}}\tilde{\mathbf{B}}, \tilde{\mathbf{C}}\tilde{\mathbf{A}}\tilde{\mathbf{B}}, \dots, \tilde{\mathbf{C}}\tilde{\mathbf{A}}^k\tilde{\mathbf{B}}, \dots\} \quad (17)$$

is called the Markov sequence and together with the input uniquely determines the forced response of the system.

5.2.3. System reduction

The ROMSI is calculated using the ERA [134]. This method requires the construction of the Hankel matrices $\tilde{\mathbf{H}}_{rs}(k)$ which are $r \times s$ block matrices defined by

$$\begin{aligned} \tilde{\mathbf{H}}_{rs}(k) &= \begin{bmatrix} \mathbf{H}_k & \mathbf{H}_{k+1} & \mathbf{H}_{k+2} & \dots & \mathbf{H}_{k+s-1} \\ \mathbf{H}_{k+1} & \mathbf{H}_{k+2} & \mathbf{H}_{k+3} & \dots & \mathbf{H}_{k+s} \\ \cdot & \cdot & \cdot & & \cdot \\ \cdot & \cdot & \cdot & & \cdot \\ \cdot & \cdot & \cdot & & \cdot \\ \mathbf{H}_{k+r-1} & \mathbf{H}_{k+r} & \mathbf{H}_{k+r+1} & \dots & \mathbf{H}_{k+s+r-2} \end{bmatrix}. \end{aligned} \quad (18)$$

The ERA initially gives a discrete-time ROMSI of the CFD code. A continuous-time ROMSI is then obtained by inverting the transformation used to get from the continuous to the discrete system (14) before system reduction. The resulting reduced aerodynamic system matrices are denoted by: \mathbf{A}_r , \mathbf{B}_r , \mathbf{C}_r and \mathbf{D}_r . Similarly the reduced state vector is \mathbf{x}_r .

5.2.4. Practical procedure for generating ROMSI for aeroelastic applications

The equation for the unsteady aeroelastic response with no damping is

$$\ddot{\mathbf{q}} + \omega^2 \mathbf{q} = \mathbf{f}, \quad (19)$$

where \mathbf{q} are the modal displacements, ω is the diagonal matrix of eigenvalues of the structural modal decomposition and \mathbf{f} is the vector of modal forces.

Separating into steady and unsteady components

$$\ddot{\mathbf{q}} + \omega^2 \mathbf{q} = \hat{\mathbf{f}} + \bar{\mathbf{f}} - \omega^2 \bar{\mathbf{q}}, \quad (20)$$

where $\bar{\mathbf{f}}$ is the modal force resulting from a steady modal displacement of $\bar{\mathbf{q}}$. Note that $\bar{\mathbf{q}}$ need not be the steady state coupled solution at the flutter condition. However, the closer this is to the steady non-linear coupled solution the more accurate the linearisation will become. Results indicate that the process is insensitive to the value of $\bar{\mathbf{q}}$ for the benign cases considered; see Section 6.3.2.

Applying the reduction technique of Section 5.2.3 with the output vector chosen to be the modal force perturbation due to an input vector defined as the modal velocities and displacements, gives a coupled system of the form

$$\begin{aligned} \frac{d}{dt} \begin{bmatrix} \dot{\mathbf{q}} \\ \hat{\mathbf{q}} \\ \mathbf{x}_r \end{bmatrix} + \begin{bmatrix} 0 & \omega^2 - \mathbf{D}_r & -\mathbf{C}_r \\ -I & 0 & 0 \\ 0 & -\mathbf{B}_r & -\mathbf{A}_r \end{bmatrix} \begin{bmatrix} \dot{\mathbf{q}} \\ \hat{\mathbf{q}} \\ \mathbf{x}_r \end{bmatrix} \\ = \begin{bmatrix} \bar{\mathbf{f}} - \omega^2 \bar{\mathbf{q}} \\ 0 \\ 0 \end{bmatrix}. \end{aligned} \quad (21)$$

The forces scale directly with the static pressure so that if the pulse responses are calculated for a free stream dynamic pressure of Q_{sim} then the modal forces at dynamic pressure Q becomes

$$\mathbf{f} \frac{Q}{Q_{\text{sim}}}. \quad (22)$$

Flutter values are found by identifying the value of Q for which any eigenvalues of the matrix on the left-hand side of Eq. (21) cross the imaginary axis.

The efficiency of the flutter prediction using the ROMSI technique is determined by the length of pulse response (number of time steps) required by ERA to identify an accurate model. This issue is investigated for the AGARD 445.6 test case used previously for initial testing of the time-domain CFD codes (Section 4.4).

5.2.5. Three-dimensional test case: the AGARD 445.6 wing

A series of flutter calculations were carried out on the weakened AGARD 445.6 (4) wing model using

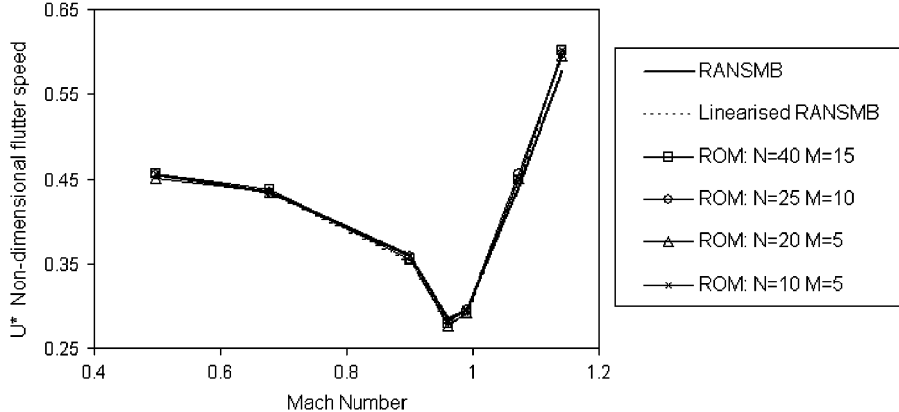


Fig. 27. Flutter boundary variation for ROMSI with number of time steps used (N) and the number of aerodynamic modes retained (M).

the full non-linear Euler code and the ROMSI technique. The wing is symmetric and hence the steady state position about which the ROMSI model is constructed is invariant with Mach number and dynamic pressure. As the flutter boundary may be defined by the stability to an infinitesimally small perturbation, the use of the dynamic linearity assumption central to the ROMSI construction is valid, and we would expect the results to clearly demonstrate the behaviour of the ROMSIs when the pulse response length and model rank are varied.

The flutter boundary for the full non-linear Euler equations is plotted in Fig. 27, together with a number of typical ROMSI flutter boundaries. These show the variation in flutter boundary location for differing numbers of time steps (N) used to create the ROMSI and differing rank (M) of ROMSI retained. It was found that the flutter boundary remained invariant to the number of time steps taken until approximately 10 time steps were used.

The execution time required to generate the flutter boundary is determined by the number of time steps used to create the ROMSI. For the AGARD wing, $15 \times 16 \times 2 = 480$ time steps were required to create a ROMSI at each Mach number, which is considerably quicker than the approximately 5000 time steps required to identify each flutter point using the full coupled time marching method. Further performance improvement can be achieved by reducing the number of modes used in the analysis.

Once created the ROMSI is valid for any pressure if the dependence of the steady state on the pressure is insignificant. As an example Fig. 28 shows time histories created using the models developed to identify the flutter boundary for Mach 0.96 and

0.499. For each Mach number the full Euler and ROMSI time histories of the tip deflection and rotation are plotted for dynamic pressures near the flutter boundary and at 25% of the flutter boundary. The ROMSI models were created using 20 time steps and can be seen to overlay the full solution.

5.3. Hopf bifurcation based methods

In 1999, Morton and Beran from the US Air Force Laboratories [146] proposed a new way of reducing the cost of calculating stability behaviour. A modified system calculates the value of the parameter for which an eigenvalue of the system Jacobian matrix crosses the imaginary axis. Their method suffered from limitations imposed by the use of a direct linear solver when solving this modified system.

These problems were resolved in [147] where a sparse matrix formulation was used to make feasible the solution of the linear system for much larger grids. The Newton iteration was modified to enhance the efficiency of the scheme following work on approximate Jacobian matrices for CFD only problems [96]. The method was shown to be effective for tracing out flutter boundaries for symmetric aerofoils moving in pitch and plunge, with reductions of two orders of magnitude in the computational time required when compared with time marching.

Whilst knowledge of the onset of instability is important, other pieces of information are required in practice. For example, flight tests measure damping and compare this with predictions to inform decisions about future test points. If this requires recourse to time-domain simulations then much of the advantage of the methods of the

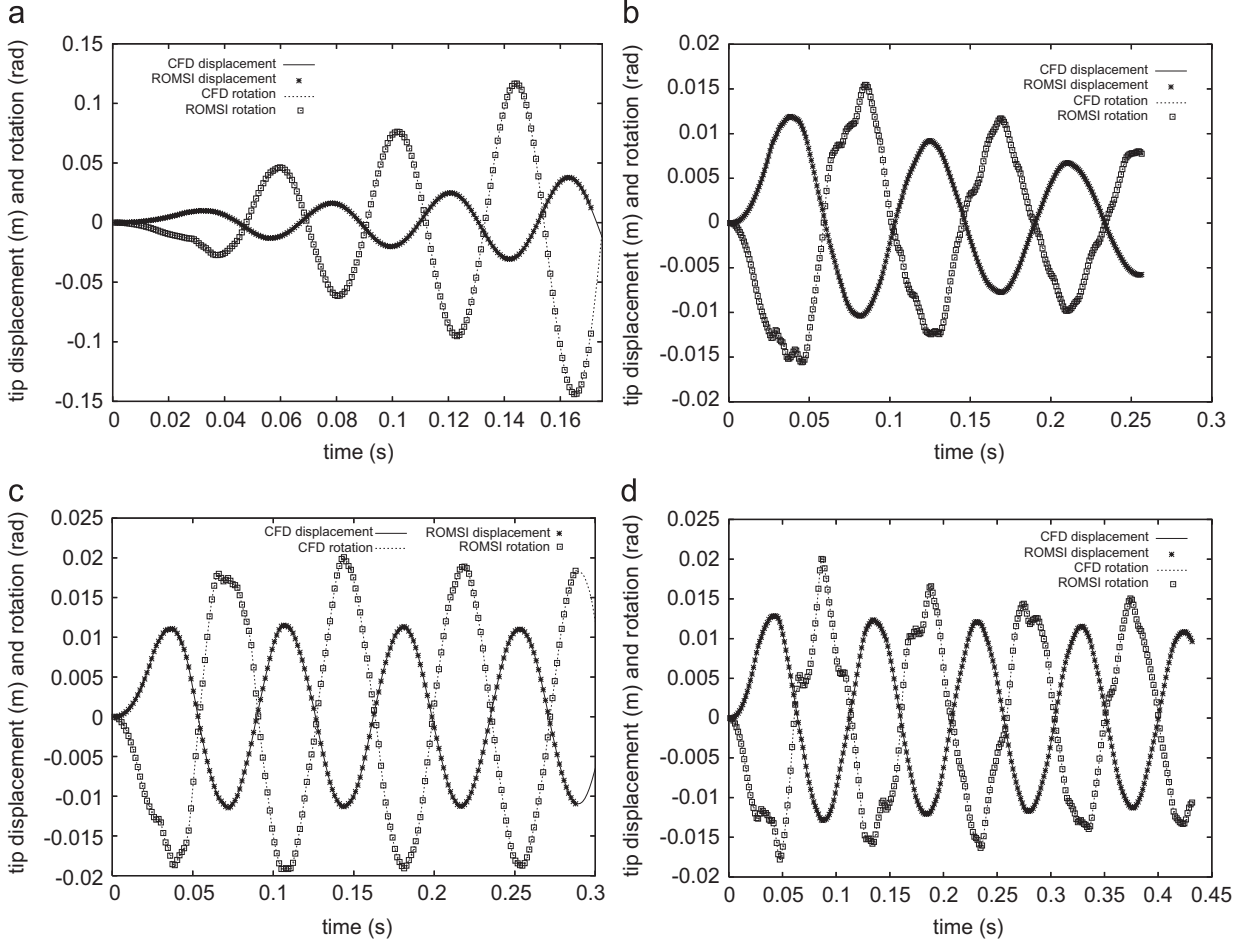


Fig. 28. Comparison of aeroelastic response of the wing tip displacement and rotation, for varying Q with fixed ROMSI: (a) Mach 0.499 Q near flutter boundary value of Q ; (b) Mach 0.499 Q at 25% of flutter boundary Q ; (c) Mach 0.96 Q near flutter boundary value of Q ; (d) Mach 0.96 Q at 25% of flutter boundary Q .

previous paragraph is lost. A systematic approach to model reduction for damping was given in [148].

This section continues with an outline of the stability prediction methods. These three methods described are the direct calculation suitable for a known (and fixed) steady state, the inverse power method which can be used to track eigenvalues for a symmetric or non-symmetric problem, and a reduced model which allows the calculation of damping. Results are presented in this section for the AGARD wing.

5.3.1. Hopf bifurcation calculation for symmetric problems

The semi-discrete form of the coupled CFD–FEM system is

$$\frac{dw}{dt} = \mathbf{R}(w, \mu), \quad (23)$$

where

$$\mathbf{w} = [\mathbf{w}_f, \mathbf{w}_s]^T, \quad (24)$$

is a vector containing the fluid unknowns \mathbf{w}_f and the structural unknowns \mathbf{w}_s and

$$\mathbf{R} = [\mathbf{R}_f, \mathbf{R}_s]^T, \quad (25)$$

is a vector containing the fluid residual \mathbf{R}_f and the structural residual \mathbf{R}_s . The residual also depends on a parameter μ which is independent of \mathbf{w} . An equilibrium of this system $\mathbf{w}_0(\mu)$ satisfies $\mathbf{R}(\mathbf{w}_0, \mu) = \mathbf{0}$.

A Hopf bifurcation with respect to the parameter μ occurs in the stability of the equilibrium at values of μ such that $A(\mathbf{w}_0, \mu)$ has one eigenvalue $i\omega$ which crosses the imaginary axis. Denoting the corresponding eigenvector by $\mathbf{P} = \mathbf{P}_1 + i\mathbf{P}_2$, a critical value of μ is one at which there is an eigenpair ω and

\mathbf{P} such that

$$\mathbf{A}\mathbf{P} = i\omega\mathbf{P}. \quad (26)$$

This equation can be written in terms of real and imaginary parts as $\mathbf{AP}_1 + \omega\mathbf{P}_2 = \mathbf{0}$ and $\mathbf{AP}_2 - \omega\mathbf{P}_1 = \mathbf{0}$. A unique eigenvector is chosen by scaling against a constant real vector \mathbf{q} to produce a fixed complex value, taken to be $0 + 1i$. This yields two additional scalar equations $\mathbf{q}^T\mathbf{P}_1 = 0$ and $\mathbf{q}^T\mathbf{P}_2 - 1 = 0$.

A bifurcation point can be calculated directly by solving the system of equations

$$\mathbf{R}_A(\mathbf{w}_A) = \mathbf{0}, \quad (27)$$

where

$$\mathbf{R}_A = \begin{bmatrix} \mathbf{AP}_1 + \omega\mathbf{P}_2 \\ \mathbf{AP}_2 - \omega\mathbf{P}_1 \\ \mathbf{q}^T\mathbf{P}_1 \\ \mathbf{q}^T\mathbf{P}_2 - 1 \end{bmatrix}. \quad (28)$$

and $\mathbf{w}_A = [\mathbf{P}_1, \mathbf{P}_2, \mu, \omega]^T$. If there are n components in \mathbf{w} then \mathbf{w}_A has $2n + 2$ components, as does \mathbf{R}_A and hence Eq. (27) is closed.

Newton's method can be used to solve this type of problem. A sequence of approximations \mathbf{w}_A^n to a solution is generated by solving the linear system

$$\frac{\partial \mathbf{R}_A}{\partial \mathbf{w}_A} \Delta \mathbf{w}_A = -\mathbf{R}_A^n, \quad (29)$$

where $\Delta \mathbf{w}_A = \mathbf{w}_A^{n+1} - \mathbf{w}_A^n$. The Jacobian matrix on the left-hand side of Eq. (29) is given in expanded form as

$$\frac{\partial \mathbf{R}_A}{\partial \mathbf{w}_A} = \begin{bmatrix} A & I\omega & (\mathbf{AP}_1)_\mu & \mathbf{P}_2 \\ -I\omega & A & (\mathbf{AP}_2)_\mu & -\mathbf{P}_1 \\ \mathbf{q}^T & 0 & 0 & 0 \\ 0 & \mathbf{q}^T & 0 & 0 \end{bmatrix}. \quad (30)$$

Another consideration for applying this approach is that a good initial condition is required, and in particular a good guess for the eigenvector is needed. To deal with non-symmetric systems, and to allow the calculation of an initial guess, a second method the inverse power method, is useful. This is described next.

5.3.2. Shifted inverse power method

The power method [149] is an algorithm for calculating the dominant eigenvalue eigenvector pair of any given diagonalisable matrix A . Its extension to the shifted inverse power method is practical for finding any eigenvalue provided that a

good initial approximation for the eigenvalues is known. Assume that the $n \times n$ matrix A has distinct eigenvalues $\lambda_1, \lambda_2, \dots, \lambda_n$ and consider the eigenvalue λ_j . Then a constant ω can be chosen so that $1/(\lambda_j - \omega)$ is the dominant eigenvalue of $(A - \omega I)^{-1}$:

For initial guess x_0 and constant ω

For $k = 1, 2, \dots$ Do :

$$\begin{aligned} z_k &= (A - \omega I)^{-1}x_{k-1}, \\ \mu_k &= \|z_k\|_\infty, \\ x_k &= z_k/\mu_k. \end{aligned} \quad (31)$$

EndDo

This system comprises the bulk of the equations for the direct Hopf bifurcation and so all the methods described below are applicable to this system as well.

If an estimate for the instability frequency is available then this can be used as a shift for the inverse power method to generate an initial guess for the direct solution. If this is not the case then the inverse power method can be applied to each structural mode to calculate the root locus.

5.3.3. Response from reduced order method

The eigenvector which goes critical at a Hopf bifurcation will also be the least lightly damped mode for parameter values in a region below the bifurcation value. In this region the asymptotic damping value will be determined by this mode. It is possible to reduce the full system by a change of variables to calculate the damping by only considering a low dimension reduced model [148].

There are two key steps involved. First, the full system variables are projected onto the critical eigenvector. Second, the full order system is expanded in a Taylor series and, applying the change of variables, is also projected onto the critical eigenvector. The result is a two degree-of-freedom model for the least damped part of the eigenspace. The model is parameterised through a Taylor expansion in the bifurcation parameter.

To represent LCOs extra terms need to be added to the damping model. The system still responds in the critical mode, but the non-linear influence of the non-critical modes, and higher order terms in the Taylor series, need to be included. The solution to the technical difficulties is presented in Ref. [150]. The result is a powerful set of methods for determining the bifurcation point,

and the pre- and post-bifurcation behaviour through a two degree-of-freedom model.

5.3.4. AGARD 445.6 wing

The first three-dimensional results were obtained using the direct method for the AGARD wing [151]. The Newton iterations were driven by the Jacobian of the first order spatial scheme. The flutter boundary in the transonic region is shown in Fig. 29 and shows perfect agreement between the direct and time domain predictions. The cost of the direct method is roughly that of a single steady state solution, which represents a reduction in computational cost when compared with the time domain method for bracketing the flutter speed of two

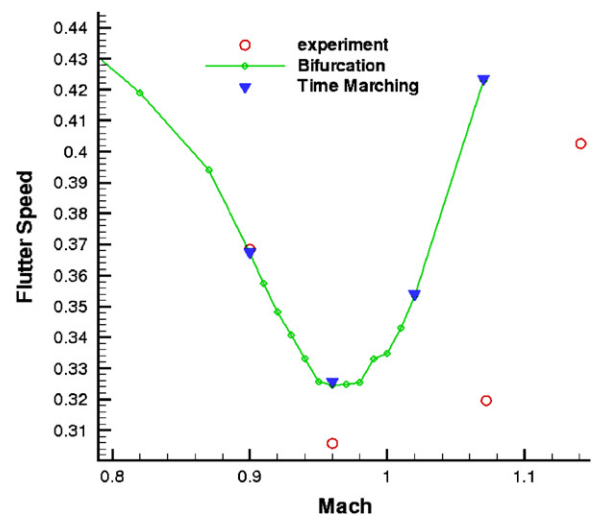


Fig. 29. Comparison with measurements of the stability boundaries calculated using time marching and the bifurcation solver [151].

orders of magnitude. A detailed study of grid refinement and the influence of damping was also given in [151].

The inverse power method can be used to track the eigenvalues with dynamic pressure and this is shown in Fig. 30. These results use the second order Jacobian matrix. The calculation of each eigenvalue pair is made at a cost of roughly one steady state solution, and so the computation of the behaviour of the four important eigenvalues at six values of dynamic pressure takes less CPU time than 30 steady state calculations.

The reduced damping model was computed [148] and results shown for values of dynamic pressure which are 5%, 10%, 20% and 40% below the bifurcation value for Mach numbers of 0.67, 0.90, 0.96 and 1.07. The response was compared with the full order system prediction, and the case at Mach 0.96 is shown in Fig. 31. Good agreement is obtained at a much reduced computational cost.

5.4. Local linearisation approaches

There are numerous examples of fundamental solutions to non-linear aeroelastic problems, starting in the 1980s (e.g. [152]) and continuing steadily to the present. The main objective is usually the prediction of the stability of such aeroelastic systems in the range of flight conditions, amplitudes, and frequencies in which LCO may be encountered. A typical system investigated by many authors is the pitch-plunge airfoil with various types of non-linearity. The most popular non-linearities investigated are cubic stiffness (e.g. [153,154], and many others) piecewise-linear stiffness (e.g. [29,155]) and, more recently, non-linear aerodynamics

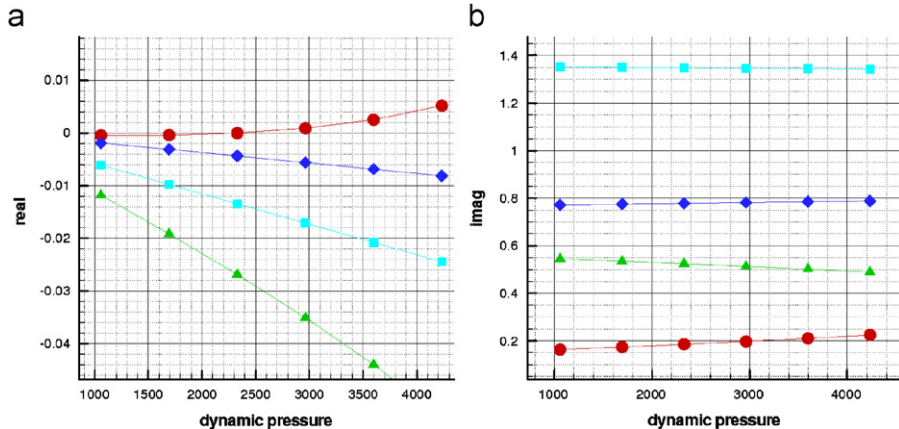


Fig. 30. Tracking of eigenvalues for AGARD wing at Mach 0.97: (a) real; (b) imaginary.

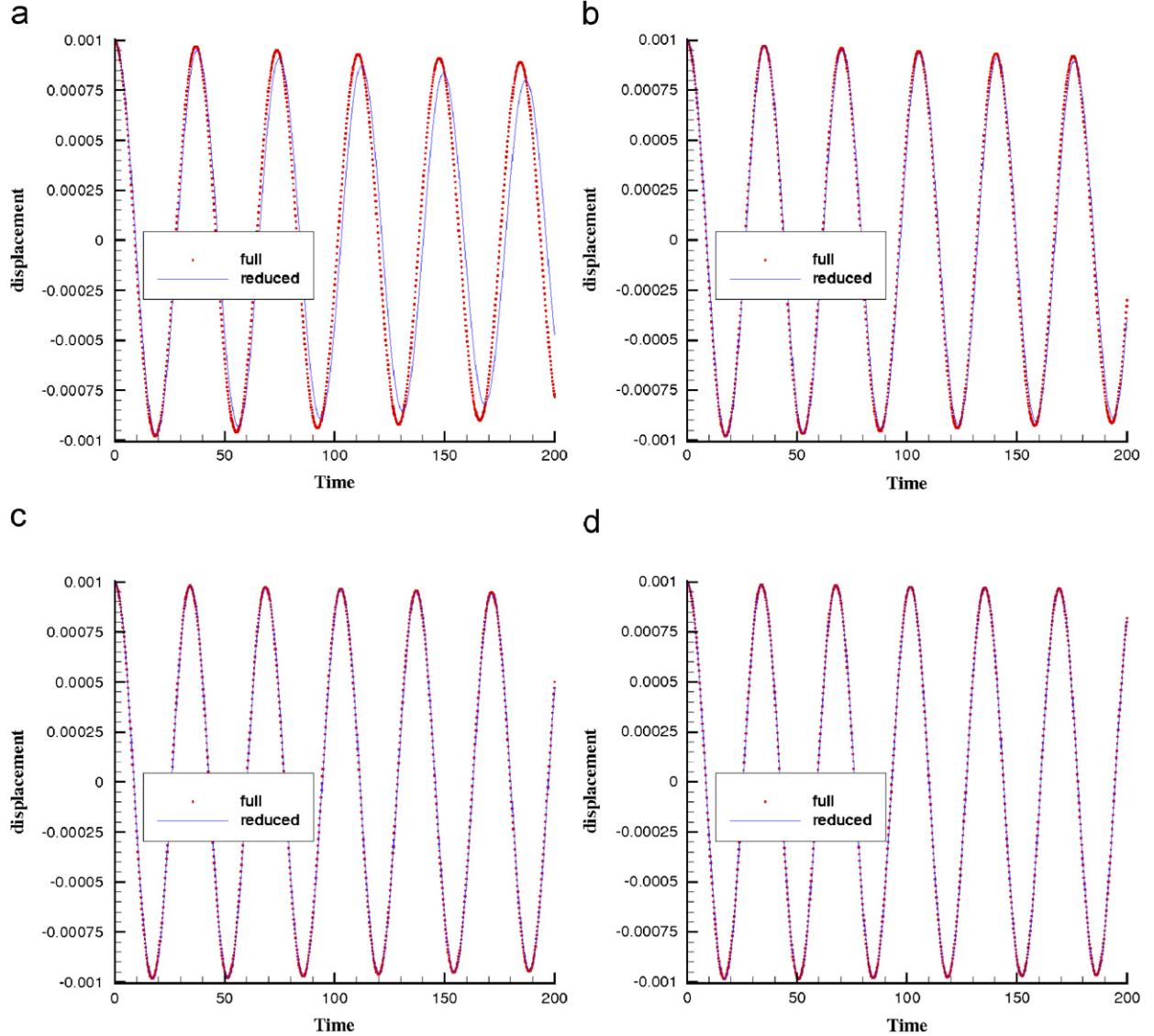


Fig. 31. Comparison of results from the full model and damping reduced model at $M = 0.96$ for values of dynamic pressure below the flutter boundary: (a) 60%; (b) 80%; (c) 90%; (d) 95%.

(e.g. [156–159]). Other types of non-linearities have been investigated such as non-linearities in the control system [160], due to external stores [31] and due to large deformations [161].

Bifurcation analysis for simple aeroelastic systems has been performed using numerous methods. These include cell mapping [162], HB [152], HOHB [57,163], center manifold [164], normal form [165], numerical continuation [166,167] and others. While these methods have shown various degrees of promise, as yet, there has been no effort to compare their performance and to determine which are the most suitable approaches for aeroelastic problems.

Here, the HOHB method and the numerical continuation approach have been applied to a significantly larger system with some relevance to industrial applications, namely the BAH wing (Table 1). It is shown that as well as a super-critical Hopf, the methodology applied here can predict a secondary Hopf bifurcation. It can be further extended to systems undergoing fold and period doubling bifurcations; this has already been achieved by other researchers but for much smaller and simpler systems. The HOHB and numerical continuation approaches can deliver a complete picture of the LCO amplitude and frequency on all

bifurcation branches existing in a system's parameter space. Furthermore, they can predict both stable and unstable limit cycles.

5.4.1. Higher order harmonic balance

The concept behind the HB (and its higher orders), as applied to free vibration problems, is very simple. The method attempts to find a Fourier series approximation of the true response of a given non-linear system that is undergoing LCO. In other words, it is assumed that the solution of the non-linear system can be represented as a sum of sine and cosine terms. Consider a general unforced non-linear system of the form

$$\dot{\mathbf{x}} = \mathbf{f}(\mathbf{x}, t, \lambda), \quad (32)$$

where $\mathbf{x}(t)$ is a $m \times 1$ vector of system states, t is the time, λ is a system parameter and $\mathbf{f}(\mathbf{x}, t, \lambda)$ is a $m \times 1$ vector of non-linear functions. The object of harmonic balancing is to identify periodic solutions of this system that can be approximated by a sum of sinusoids. There are two mechanisms by which periodic oscillations can occur: either the system is excited by an external periodic force or it is undergoing self-excited oscillations, also known as LCO. This section deals with the latter case, hence, the forced response case will not be discussed.

Assuming that the system is undergoing LCOs and following the HB methodology, the states are approximated by

$$\mathbf{x} = \mathbf{X}_0 + \sum_{k=1}^N \mathbf{X}_{k1} \sin k\omega t + \mathbf{X}_{k2} \cos k\omega t, \quad (33)$$

where ω is the fundamental response frequency, \mathbf{X}_0 , \mathbf{X}_{k1} , \mathbf{X}_{k2} are vectors of unknown coefficients and N is the order of the approximation. Eq. (33) is substituted into Eq. (32) and then harmonic balancing is performed. This consists simply of equating the coefficients of every sine and cosine term to zero. In other words, the total coefficient of $\sin \omega t$, $\cos \omega t$, $\sin 2\omega t$, $\cos 2\omega t$, etc., as well as that of the constant term must be equal to zero, in order for the equations of motion to be satisfied. Harmonic balancing leads to $m \times (2N + 1)$ non-linear algebraic equations in terms of ω , \mathbf{X}_0 , \mathbf{X}_{k1} and \mathbf{X}_{k2} , of the form

$$\mathbf{g}(\mathbf{X}_0, \mathbf{X}_{k1}, \mathbf{X}_{k2}, \omega) = \mathbf{0}, \quad (34)$$

where \mathbf{g} are non-linear functions. The solution of these equations yields a complete approximation of the true LCO behaviour of the non-linear system. Notice that there are $m \times (2N + 1) + 1$ unknowns including the frequency and only $m \times (2N + 1)$

equations. This problem can be overcome without loss of generality if, for example, the first element of \mathbf{X}_{12} is set to zero, thus decreasing the number of unknowns to $m \times (2N + 1)$.

The main condition for this procedure to work is that the system really does undergo LCO. If it does not then all the amplitudes \mathbf{X}_{k1} and \mathbf{X}_{k2} will be calculated as zero. It is obvious that the main difficulty in the HB methodology is the solution of the non-linear algebraic system. Another problem is the handling of the non-linear terms. Finally, the order, N , of the series in Eq. (33) must be selected carefully. If the order is chosen as $N = 1$, then the classical first order HB approximation is obtained. HOHB schemes refer to $N > 1$.

HB solutions can be continued using a pseudo-arc length approach, exactly as is done for numerical continuation. If natural parameter continuation is chosen then HOHB solutions will also fail at bifurcation points. The direction of the continuation is defined by

$$\frac{\partial \mathbf{X}^T}{\partial s} \frac{\partial \mathbf{X}}{\partial s} + \frac{\partial \omega^2}{\partial s} + \frac{\partial \lambda^2}{\partial s} = 1, \quad (35)$$

where $\mathbf{X} = [\mathbf{X}_0^T \mathbf{X}_{k1}^T \mathbf{X}_{k2}^T]^T$. Secondary Hopf bifurcations are negotiated by keeping \mathbf{X} constant but increasing the frequency ω by one harmonic.

5.4.2. Numerical continuation

Numerical continuation is a class of methods that have been developed over many years to solve nonlinear problems that depend on the values of one or more parameters. There are several software packages available that can perform numerical continuation, such as AUTO [168] and MATCONT [169]. Some of these packages have been used for aeroelastic bifurcation analysis, such as the work by Roberts et al. [166], Beran et al. [170] and Dimitriadis et al. [167]. However, these packages were not developed specifically for aeroelastic models and have limitations on the size of system they can handle. In this work, a faster numerical continuation approach, referred to as incremental numerical continuation [171], is presented and demonstrated on a realistic model of a wing.

Consider again Eq. (32) and assume that the system they describe admits periodic solutions of period T for a range of λ values. The time coordinate can be scaled with respect to the period using

$$\tau = \frac{t}{T} \quad (36)$$

so that Eq. (32) becomes

$$\mathbf{x}' = T\mathbf{f}(\mathbf{x}, \lambda), \quad (37)$$

where ' denotes differentiation with respect to τ .

Assume that Eq. (32) has a known periodic solution, $\mathbf{x}_0(t)$ at λ_0 with a period T_0 . This solution may have been obtained through numerical integration. Then

$$\mathbf{x}'_0 = T_0\mathbf{f}(\mathbf{x}_0, \lambda_0). \quad (38)$$

Solutions \mathbf{x} in the neighbourhood of λ_0 are sought, without recourse to further numerical integration. It is assumed that the derivative of \mathbf{f} with respect to λ is continuous and finite in the neighbourhood. Furthermore, it is assumed that a small increase in the value of λ , from λ_0 to $\lambda_0 + \Delta\lambda$, will result in small increases in the values of \mathbf{x} and T . Therefore,

$$\begin{aligned} \mathbf{x} &= \mathbf{x}_0 + \Delta\mathbf{x}, \\ T &= T_0 + \Delta T. \end{aligned} \quad (39)$$

Substituting Eqs. (39) into (37) yields

$$\mathbf{x}'_0 + \Delta\mathbf{x}' = (T_0 + \Delta T)\mathbf{f}(\mathbf{x}_0 + \Delta\mathbf{x}, \lambda_0 + \Delta\lambda). \quad (40)$$

Expanding the non-linear function as a first order Taylor series around λ_0 yields

$$\begin{aligned} \mathbf{x}'_0 + \Delta\mathbf{x}' &= (T_0 + \Delta T)\left(\mathbf{f}(\mathbf{x}_0, \lambda_0) + \frac{d\mathbf{f}}{d\mathbf{x}}\Big|_{\mathbf{x}_0, \lambda_0}\right. \\ &\quad \times \Delta\mathbf{x} + \left.\frac{d\mathbf{f}}{d\lambda}\Big|_{\mathbf{x}_0, \lambda_0}\right. \Delta\lambda \\ &= T_0\mathbf{f}(\mathbf{x}_0, \lambda_0) + T_0\mathbf{A}\Delta\mathbf{x} + T_0\mathbf{B}\Delta\lambda + \mathbf{C}\Delta T, \end{aligned} \quad (41)$$

where the notation has been simplified using

$$\begin{aligned} \mathbf{A}(t) &= \frac{d\mathbf{f}}{d\mathbf{x}}\Big|_{\mathbf{x}_0, \lambda_0}, \\ \mathbf{B}(t) &= T_0 + \frac{d\mathbf{f}}{d\lambda}\Big|_{\mathbf{x}_0, \lambda_0}, \\ \mathbf{C}(t) &= \mathbf{f}(\mathbf{x}_0, \lambda_0) \end{aligned} \quad (42)$$

and terms in $\Delta T\Delta\mathbf{x}$ and $\Delta T\Delta\lambda$ are assumed to be negligible. Substituting from Eqs. (40) into (41) yields

$$\Delta\mathbf{x}' = T_0\mathbf{A}\Delta\mathbf{x} + T_0\mathbf{B}\Delta\lambda + \mathbf{C}\Delta T. \quad (43)$$

Eq. (43) is a set of n first order linear differential equations with time-varying coefficients, to be solved for the unknown changes $\Delta\mathbf{x}$ and ΔT . As with all initial value problems, the solution $\Delta\mathbf{x}(t)$ depends uniquely on the value of the initial conditions, $\Delta\mathbf{x}(0)$. Since the solution \mathbf{x} must be

periodic the states must have the same values at the beginning and the end of the period, i.e. $\mathbf{x}(0) = \mathbf{x}(T)$. The initial solution \mathbf{x}_0 is also periodic so that $\mathbf{x}_0(0) = \mathbf{x}_0(T)$, meaning that

$$\Delta\mathbf{x}(0) = \Delta\mathbf{x}(T). \quad (44)$$

Therefore, solutions to Eq. (43) are sought, such that Eq. (44) is satisfied. There are n unknown initial conditions and one unknown period perturbation, ΔT , for a total of $n + 1$ unknowns; while there are only n equations.

In order to complete the system of equations it must be noticed that $\Delta\mathbf{x}$ can only be small if \mathbf{x}_0 and \mathbf{x} are in phase. Therefore, it must be ensured that there is no phase shift between \mathbf{x}_0 and \mathbf{x} . There is no unique condition that will force the two signals to be in phase. One such condition used by the developers of AUTO and CONTENT [172] is

$$\int_0^1 \mathbf{x}^T \mathbf{x}'_0 d\tau = 0 \quad (45)$$

which requires that the signals \mathbf{x} and \mathbf{x}'_0 be 90° out of phase (orthogonal). Eqs. (43)–(45) can be transformed to a linear system of equations and solved simultaneously, thus avoiding the time-consuming Newton-type iterations used by AUTO and other software packages. The simplest way to achieve this is to apply a forward finite difference expansion to Eqs. (43) and solve the complete system for $\Delta\mathbf{x}(0)$ and ΔT .

The solution can be continued by changing the value of λ by $\Delta\lambda$ at each step. This procedure is called natural parameter continuation and will fail at bifurcation points. In this work, pseudo-arclength continuation [173] is employed instead. The solution is continued with respect to the distance travelled along the LCO branch, known as the arclength, s . The direction of the continuation is normalised such that

$$\frac{\partial \mathbf{x}(0)^T}{\partial s} \frac{\partial \mathbf{x}(0)}{\partial s} + \frac{\partial T^2}{\partial s} + \frac{\partial \lambda^2}{\partial s} = 1. \quad (46)$$

This continuation approach will not fail at fold bifurcations. Finally, the branch-switching approach by Beyn et al. [174] is used in order to change branches when Hopf bifurcations are encountered.

5.4.3. The BAH aeroelastic wing model

The aeroelastic model used in this work is a mathematical representation of the BAH wing (Table 1) as used in [76]. It is a jet transport wing

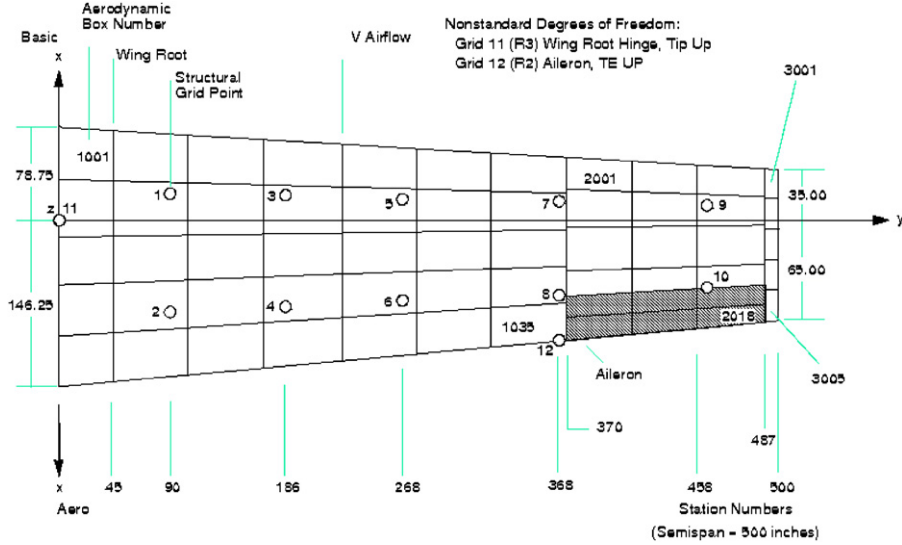


Fig. 32. BAH wing and finite element model [76].

devised by Bisplinghoff et al. [5]. Rodden et al. [75] adapted this wing for use as a demonstrator for the MSC.NASTRAN software. The wing and its associated FEM are shown in Fig. 32.

The structural model of the BAH wing is a FEM with 12 nodes translating to 72 degrees of freedom. In modal space nine modes are retained. The aerodynamic forces are calculated using the generalised AIC matrix obtained from MSC.NASTRAN. In modal space the equations of motion are

$$\mathbf{M}\ddot{\mathbf{q}} + \mathbf{C}\dot{\mathbf{q}} + \mathbf{K}\mathbf{q} = \mathbf{Q}(s, V), \quad (47)$$

where V is the free stream airspeed, s is the Laplace operator, \mathbf{M} , \mathbf{C} , and \mathbf{K} are the structural mass, damping, and stiffness matrices and \mathbf{Q} is the AIC matrix. In this case the structural damping matrix is equal to zero. Notice that \mathbf{Q} is a function of s and therefore this form of the equations of motions can only be solved in the Laplace or frequency domain (if the substitution $s = i\omega$ is assumed). Non-linear systems are usually represented in the time domain therefore the equations of motion must be transformed to this domain before adding the non-

linearity. This is achieved using the rational fraction approximation approach by Eversman and Tewari [175]. Using Roger's formula [176] the AIC matrix is written as a rational fraction expansion of the form

$$\mathbf{Q}(s) = \frac{1}{2}\rho V^2 \left(\mathbf{A}_0 + s \frac{c}{V} \mathbf{A}_1 + s^2 \left(\frac{c}{V} \right)^2 \mathbf{A}_2 + \frac{V}{c} \sum_{n=1}^{n_L} \frac{\mathbf{A}_{n+2}}{s + (V/c)\gamma_n} \right), \quad (48)$$

where ρ is the air density, c is the wing chord, \mathbf{A}_n are 9×9 constant matrices, γ_n are aerodynamic lag variables and n_L is the number of lag variables. For this work, n_L was chosen to be equal to 4. The \mathbf{A}_n matrices and γ_n lags can be calculated using any number of methods, including the method described by Eversman and Tewari [175]. Then, the equations of motion can be written in their final form as

$$\dot{\mathbf{x}} = \mathbf{Ax}, \quad (49)$$

where \mathbf{x} is a 54×1 state vector containing the modal velocities, modal displacements and 36 aerodynamic states and \mathbf{A} is given by

$$\mathbf{A} = \begin{pmatrix} -\bar{\mathbf{M}}^{-1}\bar{\mathbf{C}} & -\bar{\mathbf{M}}^{-1}\bar{\mathbf{K}} & -\bar{\mathbf{M}}^{-1}\bar{\mathbf{A}}_3 & -\bar{\mathbf{M}}^{-1}\bar{\mathbf{A}}_4 & -\bar{\mathbf{M}}^{-1}\bar{\mathbf{A}}_5 & -\bar{\mathbf{M}}^{-1}\bar{\mathbf{A}}_6 \\ \mathbf{I} & \mathbf{0} & \mathbf{0} & \mathbf{0} & \mathbf{0} & \mathbf{0} \\ \mathbf{0} & \mathbf{I} & (-V/c)\gamma_1 \mathbf{I} & \mathbf{0} & \mathbf{0} & \mathbf{0} \\ \mathbf{0} & \mathbf{I} & \mathbf{0} & (-V/c)\gamma_2 \mathbf{I} & \mathbf{0} & \mathbf{0} \\ \mathbf{0} & \mathbf{I} & \mathbf{0} & \mathbf{0} & (-V/c)\gamma_3 \mathbf{I} & \mathbf{0} \\ \mathbf{0} & \mathbf{I} & \mathbf{0} & \mathbf{0} & \mathbf{0} & (-V/c)\gamma_4 \mathbf{I} \end{pmatrix}, \quad (50)$$

where

$$\begin{aligned}\bar{\mathbf{M}} &= \mathbf{M} - \frac{1}{2} \rho c^2 \mathbf{A}_0, & \bar{\mathbf{C}} &= -\frac{1}{2} \rho V c \mathbf{A}_1, \\ \bar{\mathbf{K}} &= \mathbf{K} - \frac{1}{2} \rho V^2 \mathbf{A}_2, & \bar{\mathbf{A}}_n &= \frac{1}{2c} \rho V^3 \mathbf{A}_{n+2}.\end{aligned}\quad (51)$$

Eq. (49) is a complete representation of the linear BAH wing in the time domain. As mentioned earlier, a small amount of bilinear stiffness has been added to the control surface rotation. Bilinear non-linearity is characterised by the following equation:

$$f(y_c) = \begin{cases} K_2 y_c + (K_1 - K_2)\delta & \text{if } y_c > \delta, \\ K_1 y_c & \text{if } -\delta < y_c < \delta, \\ K_2 y_c + (K_2 - K_1)\delta & \text{if } y_c < -\delta, \end{cases}\quad (52)$$

where y_c is the co-ordinate on which the non-linearity depends, δ is the width of the bilinear region, K_1 is the stiffness inside the bilinear region and K_2 is the stiffness everywhere else. The control surface rotation is represented by the 71st physical displacement of the finite element grid, i.e. $y_c = y_{71}$. The modal stiffness matrix was transformed to the physical domain using the modal transformation matrix, Φ , also provided by MSC.NASTRAN. Then, the 71st diagonal element of the physical stiffness matrix was set to 0. The instantaneous values of

$y_c = y_{71}$ can be obtained from

$$y_{71}(t) = \Phi_{71} \mathbf{q}, \quad (53)$$

where Φ_{71} is the 71st row of the modal matrix Φ . The full non-linear equations of motion become

$$\dot{\mathbf{x}} = \mathbf{Ax} + \mathbf{af}(y_{71}), \quad (54)$$

where $\mathbf{a} = [\bar{\mathbf{M}}^{-1} \Phi_{71}^T \mathbf{n} \ 0]^T$, where \mathbf{n} is a 72×1 vector whose elements are equal to zero except for the 71st elements which is equal to 1. Only a small amount of bilinearity was added to the system with $K_1 = 10^4$ and $K_2 = 1.17 \times 10^4$, while the width of the bilinear region was set to $\delta = 0.01$ rad. Fig. 33 shows the resulting shape of the bilinear function.

5.4.4. Results

Fig. 34 shows the LCO maximum amplitude and fundamental frequencies obtained for a range of airspeeds from the HOHB method, compared to the numerical integration results. Only the top half of the amplitude diagram is shown as the LCOs are symmetrical. Two HB solutions are plotted, a fifth order and 17th order one. It can be seen that the maximum amplitudes and fundamental frequencies from the two schemes are identical. The difference can only be seen when looking at the converged waveforms of the LCOs obtained at a single airspeed. Fig. 35 shows the LCO waveforms in y_{71}

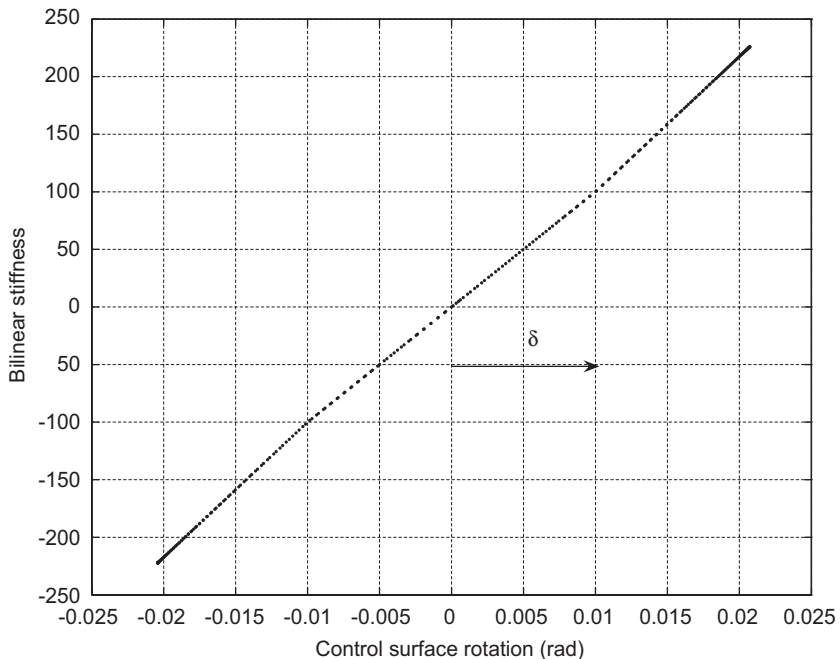


Fig. 33. Bilinear stiffness function.

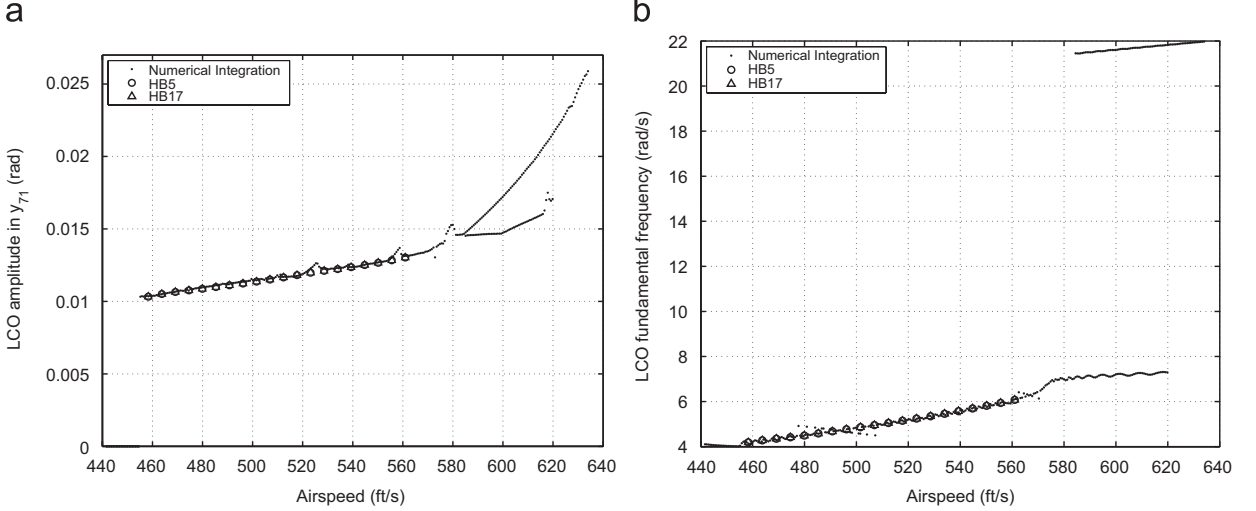


Fig. 34. Harmonic balance LCO amplitude and frequency diagrams: (a) amplitude; (b) frequency.

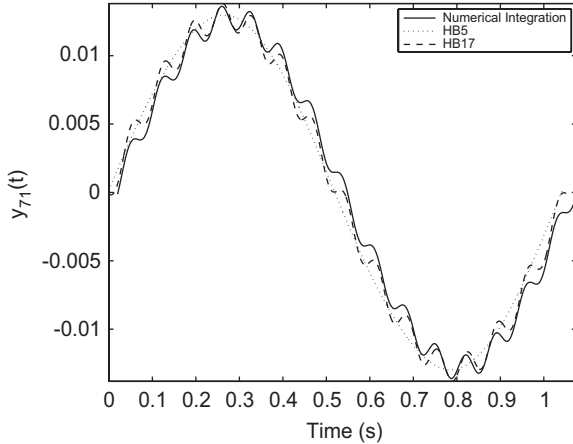


Fig. 35. Comparison of waveforms obtained from fifth and 17th order HB schemes at 560 ft/s.

obtained from numerical integration, the fifth order and the 17th order scheme at $V = 560$ ft/s. It is obvious that the 17th order scheme yields a waveform that correctly contains a significant higher order component (actually 15th order), which is missing from the LCO predicted by the fifth order method. However, the difference in maximum amplitude between the two LCOs is very small.

A second striking feature of Fig. 34 is that there are no HB results at airspeeds higher than 565 ft/s. At this airspeed the system undergoes a secondary Hopf bifurcation. The existence of a secondary Hopf can be verified by the eigenvalues of the determinant of the HB scheme. Fig. 36 shows the variation of the real and imaginary parts of a pair of

conjugate eigenvalues from 525 to 565 ft/s. It can be seen that the real part becomes zero just after 565 ft/s. The existence of a pair of purely imaginary conjugate eigenvalues is the definition of a Hopf bifurcation.

The secondary Hopf point causes the single LCO branch to split into two. The HB scheme can jump straight through a secondary (or primary in fact) Hopf point and follow the original branch. The branch is followed up to an airspeed of 620 ft/s where it becomes unstable (as seen in the numerical integration results).

A harmonic shifting approach can be used to move to the higher LCO branch. The amplitude values calculated pre-critically are kept constant but moved to progressively higher harmonics post-critically until a converged solution is obtained. For example, X_{31} becomes equal to X_{11} and X_{11} is set to zero; similarly for all the other coefficients. The fundamental frequency is kept equal to the pre-bifurcation value. This new set of X and ω values is then used as the initial guess in the HOHB procedure. Notice that classical Hopf bifurcation does not introduce sub-harmonics so the harmonic shifting need only be performed in one direction.

Fig. 37 shows LCO amplitude and frequency results obtained from a fifth order HB scheme with harmonic shifting. The new fundamental frequency is three times the pre-bifurcation frequency, i.e. the LCO has only moved up by one harmonic. It can be seen that now both the lower and upper LCO branches are accurately calculated.

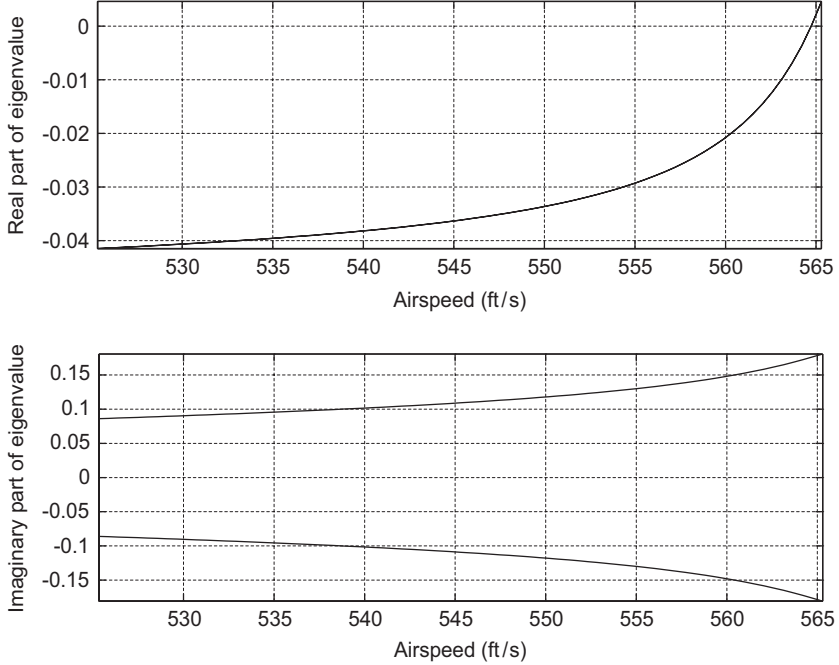


Fig. 36. Behaviour of eigenvalues and determinant of Jacobian near secondary Hopf bifurcation.

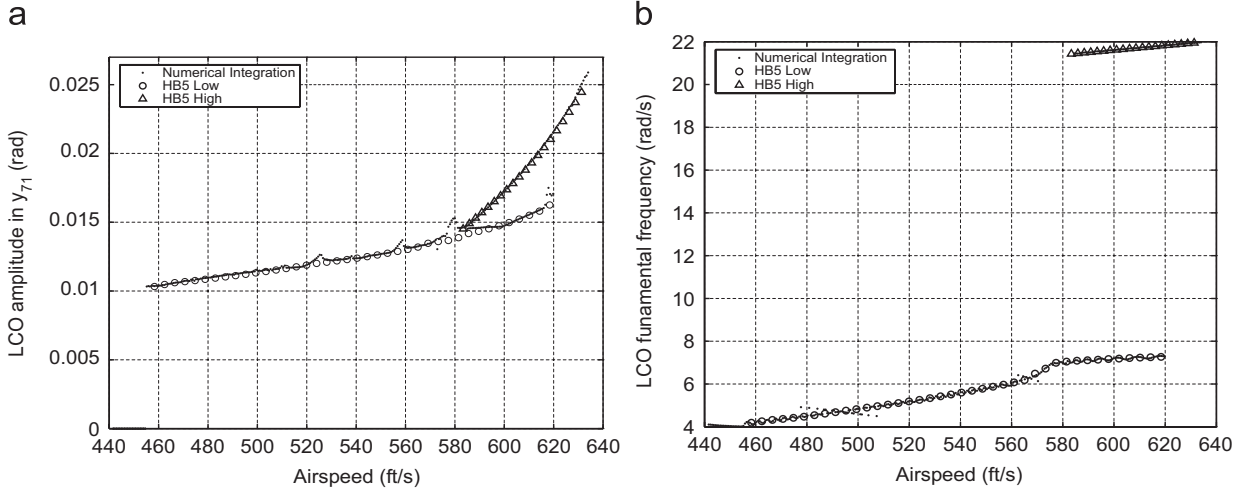


Fig. 37. Harmonic balance with harmonic shifting LCO amplitude and frequency diagrams: (a) amplitude; (b) frequency.

Fig. 38 shows bifurcation diagrams obtained by a fifth and a 17th order scheme for the lower LCO branch. These should be compared to Fig. 39 obtained from numerical integration. It can be seen that the fifth order HB scheme misses the two intermittent regions of increased complexity. Additionally, it yields a lower order approximation to the bifurcation diagram after the second Hopf

point. Conversely, the 17th order scheme captures both the intermittent regions and the full complexity of the post-critical LCOs. It is, however, much more computationally expensive, with an execution time comparable to that of the numerical integration algorithm.

Numerical continuation results for the Bisplinghoff, Ashley and Halfman (BAH) wing model are

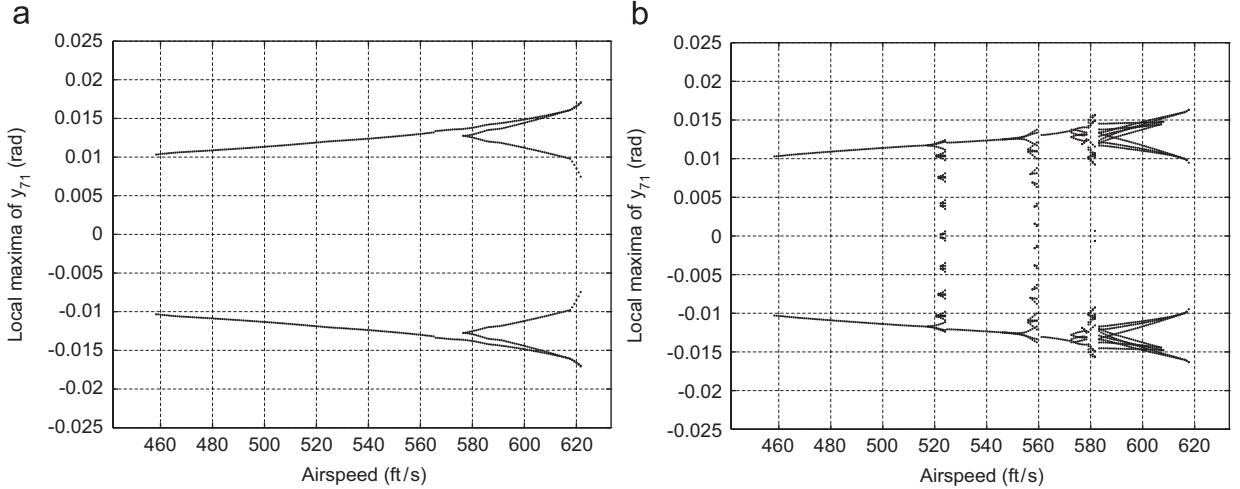


Fig. 38. Bifurcation diagrams from fifth and 15th order HB schemes for the lower LCO branch: (a) HB5; (b) HB17.

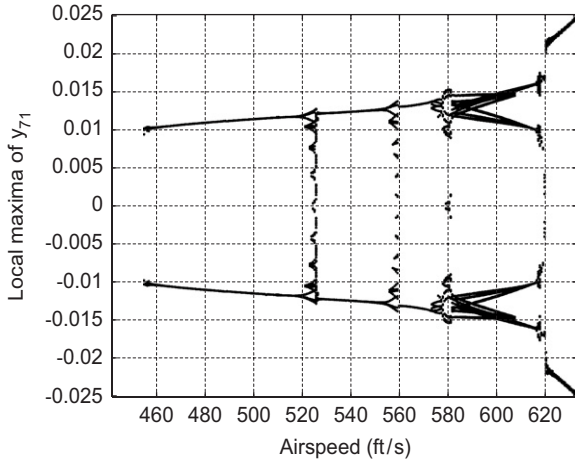


Fig. 39. Lower branch bifurcation diagram.

presented in Fig. 40. The numerical continuation results are compared against numerical integration for both amplitude (Fig. 40(a)) and frequency (Fig. 40(b)). Again only the positive amplitude axis is shown as the LCOs are symmetrical. As with the HOHB technique both LCOs branches are correctly predicted for both amplitude and frequency.

The secondary Hopf bifurcation is successfully negotiated and the period doubling behaviour is accurately captured. In fact, the bifurcation diagram obtained from the numerical continuation solution is identical to Fig. 39 obtained from numerical integration. The execution time of the numerical continuation approach was comparable to that of the fifth order HOHB scheme.

6. Application of technologies

6.1. Goland wing

6.1.1. Introduction

An example of non-linearity seen in flight is the LCO of the F-16 with certain store combinations [31]. The prediction of this phenomenon has stimulated the development of new computational methods. A model problem developed to test methods is the Goland wing with a tip store (Table 2). The Goland wing has a chord of 6 ft and a span of 20 ft, a 4% thick parabolic section, and is unswept. This wing is interesting because of the appearance of an LCO bucket at transonic conditions. Investigations of this bucket have been made using the TSD [77] and Euler equations [177]. Studies of the influence of the inertial properties of the tip store [178] and the inclusion of the store aerodynamics [179] have also been published.

The current section uses this test case for two purposes. First, the case is useful to test the time domain simulation. Second, it is of practical interest to examine time responses just before the onset of LCO to see if there is any sign of what is coming.

6.1.2. Time-domain results

Results were generated for the heavy version of the Goland wing. In the CFD calculations the tip store was neglected. A grid with 27,000 points was generated, again with points concentrated around the tip region. The structural model includes the tip store, and is based on Ref. [77]. Four modes were

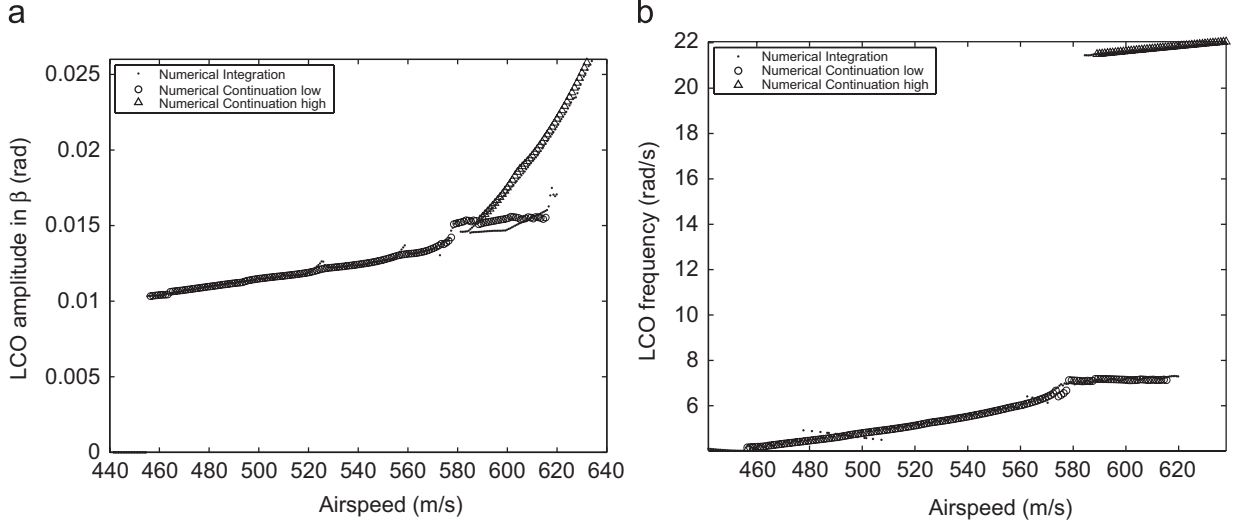


Fig. 40. Numerical continuation result: (a) LCO amplitude; (b) LCO frequency.

retained in the simulation (first bending at 1.72 Hz, first torsion at 3.05 Hz, second bending at 9.18 Hz and second torsion at 11.10 Hz). The full FE model was built in MSC.NASTRAN using CQUAD4 and CROD elements.

A set of time-domain calculations was computed at sea level conditions. Previous published results showed the appearance of an LCO for a narrow range of Mach number around $M = 0.92$. A time step equivalent to around 70 steps per cycle of response was used. The response for many Mach numbers was calculated and four examples are shown in Fig. 41. These Mach numbers are to the left of the bucket (0.89), in the bucket (0.93 and 0.94) and to the right (0.96). The surface solution at the extremes of the cycle for the limit cycle response is shown in Fig. 42. Here the contours show the difference in the instantaneous and the mean pressure values. The undeflected tip location is also shown. The motion at the tip is predominantly a pitching about the leading edge. The main pressure changes induced by this motion are a shock movement and a change in pressure distribution around the tip leading edge.

Fig. 43 is a bifurcation plot, i.e. a plot of the LCO branch that the system is following. LCO amplitude is plotted against Mach number. LCOs are first encountered at $M = 0.915$ and disappear at $M = 0.95$. The bifurcation plot was calculated from time-marching simulations from two different sets of initial conditions. The two resulting curves are very similar, indicating that this is the only LCO branch for the Goland wing.

6.1.3. Signal processing and parameter estimation

Few studies have concentrated on the subject of predicting the onset of LCOs from sub-critical data in a manner similar to traditional flight flutter testing methodologies which can determine the flight condition at which linear flutter occurs without ever testing at this flight condition. The objective is to use a number of signal processing and system identification methodologies to analyse sub-critical data in order to predict changes in the stability of aeroelastic structures for many types of bifurcation. Such a capability would be very useful, not only for the analysis of coupled CFD/FE models, but also during flight flutter testing. The initial focus is on the use of data from a simulated system. The responses to initial conditions of the Goland wing CFD/FE model at different flight speeds are analysed to determine the extent of the non-linearity below the critical onset of LCO.

Short time Fourier transform (STFT) and Hilbert transform are used to determine the presence of non-linearity, while the Nissim and Gilyard [180] method is used to estimate the aeroelastic parameters. Although this method is valid in subsonic flows, Lisandrini et al. [181] have shown that this approach can be applied in the transonic flight regime, as long as the shock waves are weak. For a system with linear aerodynamics the identified structural matrices, must be fairly constant with flight condition.

The STFT and Hilbert transform for mode 1 responses at $M = 0.9$ are shown in Fig. 44. The

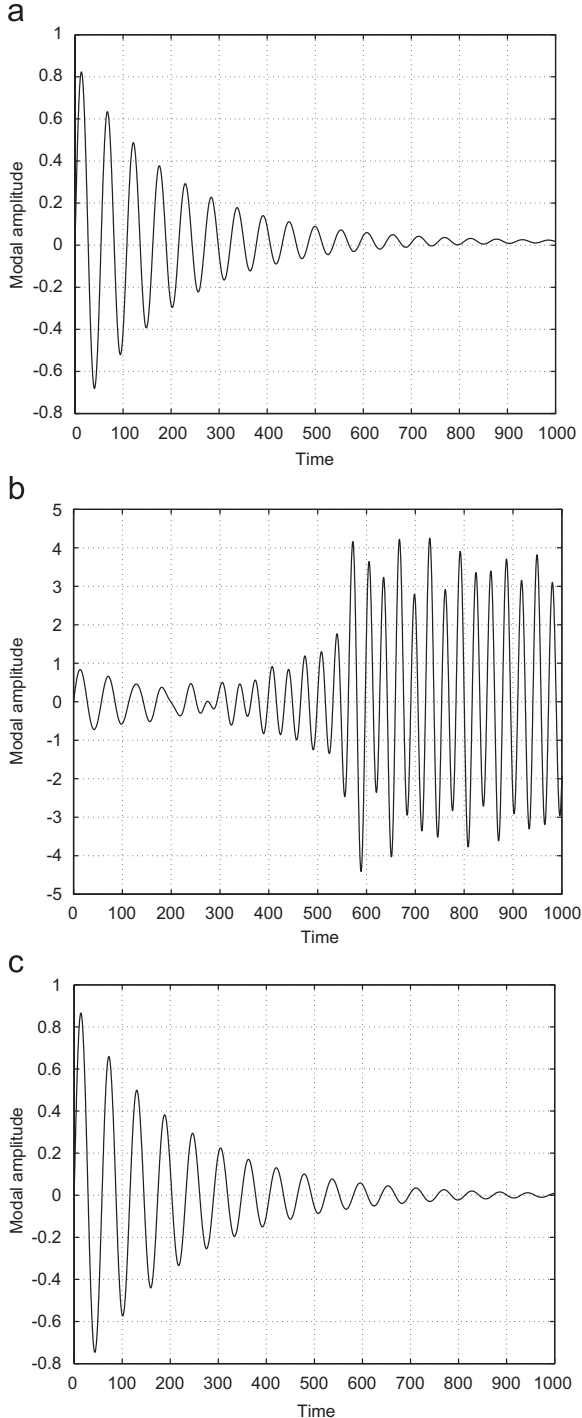


Fig. 41. Goland wing responses of mode 1 for increasing Mach numbers: (a) $M = 0.90$; (b) $M = 0.92$; (c) $M = 0.95$.

STFT for $M = 0.9$ (Fig. 44(a)) contains a single constant frequency throughout the duration of the response. There is no indication of non-linearity as

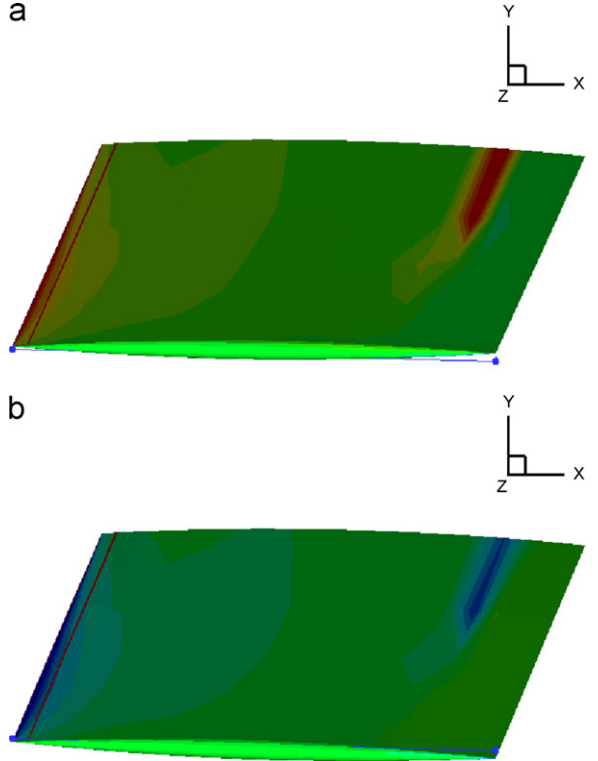


Fig. 42. Response at extremes of the Goland wing at 1.35 times the critical value of dynamic pressure. The undeflected tip position of the wing is indicated and the surface contours shown are for change of pressure from the equilibrium value. These results are for the Goland wing at Mach 0.92: (a) up; (b) down.

there are no higher harmonics and the frequency does not change over time. At the same Mach number, the backbone curves derived via the Hilbert transform can be observed in Fig. 45(a). The backbones show the frequency at which the system oscillates at various vibration amplitude or damping levels. For the $M = 0.9$ case the frequency of oscillation remains constant for all amplitude and damping values, as expected from a linear system.

At $M = 0.92$ the STFT shows a shift in frequency with time (Fig. 45(a)). There is an initial frequency component which decays and disappears momentarily, reappearing at a non-dimensional time of 500. A new frequency component appears which carries on indefinitely. The amplitude backbone curve of Fig. 45(b) also displays three distinct regions, one due to the initial decay, one due to the transition towards the LCO and one due to the fully developed LCO. As the LCO introduces a higher frequency component it can be concluded that the non-linearity is stiffening in nature.

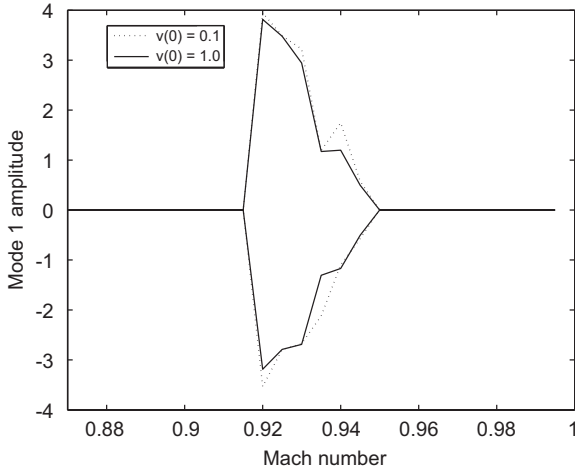


Fig. 43. Bifurcation plot for Goland wing at two different sets of initial conditions.

If the system is linear at pre-bifurcation conditions, the Nissim and Gilyard method can be used to identify the aeroelastic equation of motion. Each term of the identified structural damping matrix is plotted for increasing Mach number in Fig. 46. Up until $M = 0.88$ the terms of the identified matrix are fairly constant, after this speed some of the terms start to deviate. This shift from constant becomes total at $M = 0.905$. All the other identified matrices present a similar pattern of behaviour. At $M = 0.945$ the terms of the identified matrices have reverted back to the linear values. The bifurcation is found to start around $M = 0.91$. This can be used for the prediction of the non-linear behaviour that, in this case leads to instability. However, this prediction would only be able to use speeds that are within 6% of the bifurcation Mach number.

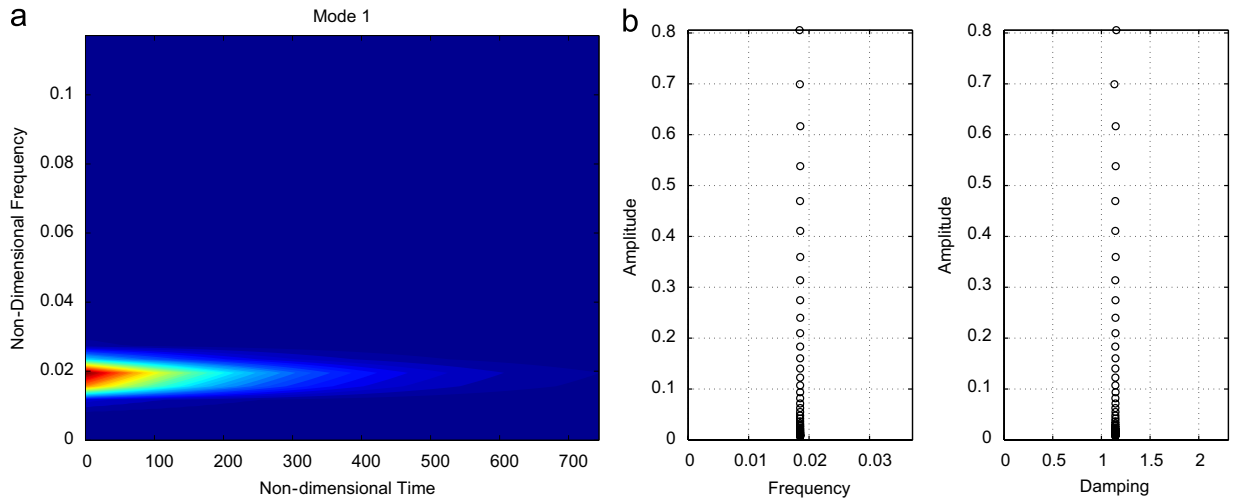


Fig. 44. $M = 0.90$: (a) STFT; (b) Hilbert transform.

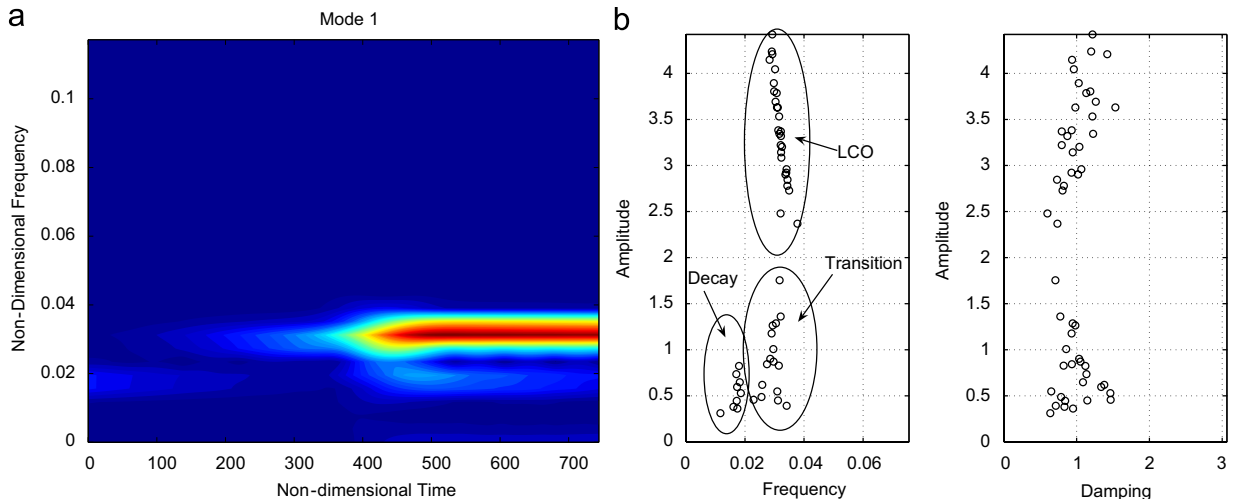


Fig. 45. $M = 0.92$: (a) STFT; (b) Hilbert transform.

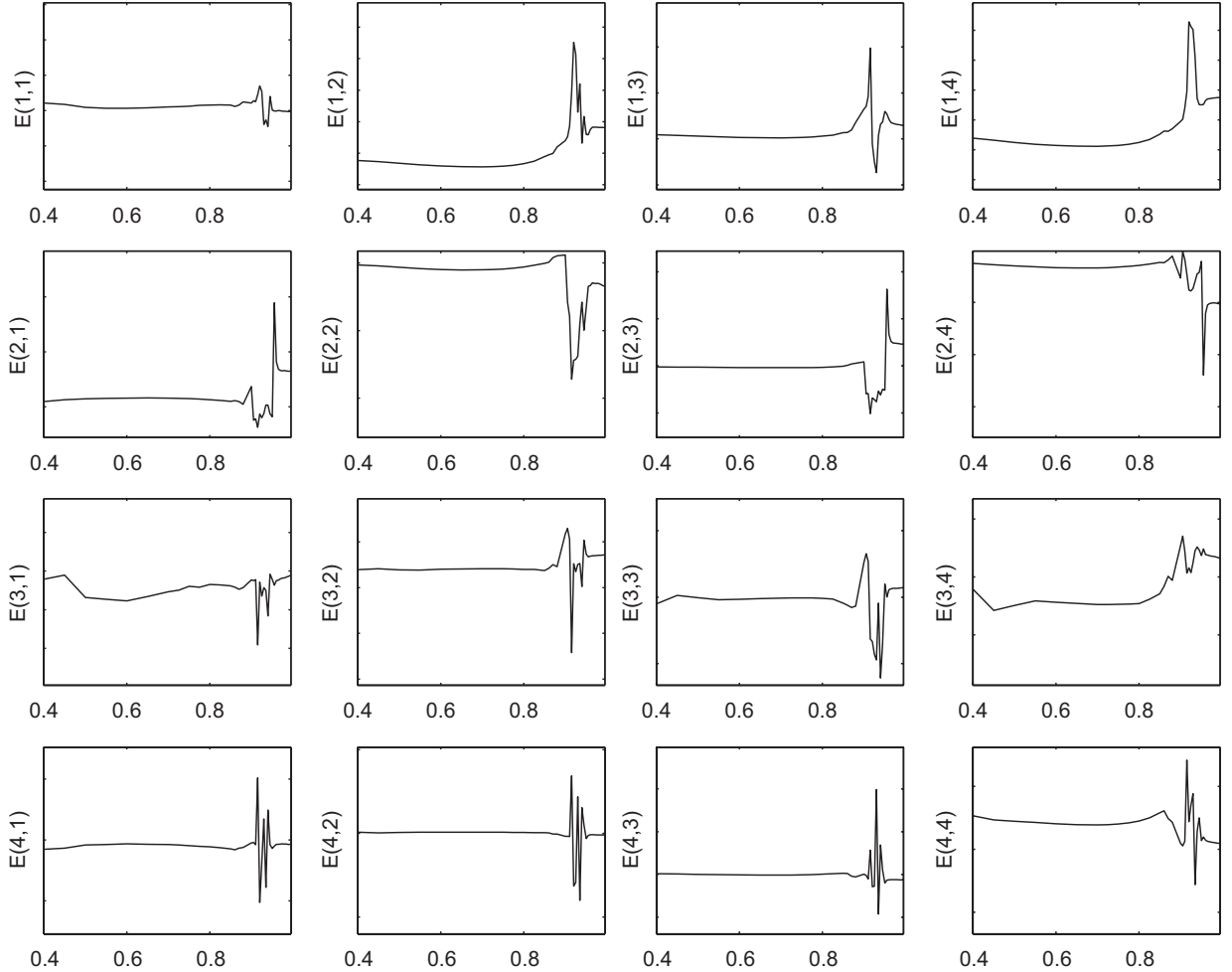


Fig. 46. Goland model identified matrix.

By looking at the local Mach number on the upper surface at various speeds (Fig. 47) it can be seen that at $M = 0.88$ the flow over the entire wing is subsonic, by the time $M = 0.90$ is reached a supersonic region has appeared. A shock wave is present lying at approximately 75% of the chord-length. At $M = 0.93$ the supersonic region has grown and the shock wave has moved to 85% of the chord. At $M = 0.96$ most of the flow on the wing's surface is supersonic and the shock wave has moved to the trailing edge.

The application of linear signal processing and system identification techniques to data from the CFD/FE model shows that the bifurcation flight condition can be predicted using linear methods. This is a significant finding because it means that, for the type of aeroelastic instability investigated here, linear data analysis methods can be used

during flight flutter testing. However, such methods can only predict the bifurcation condition, they cannot model the post-bifurcation behaviour, i.e. LCO amplitude and frequency. The non-linearity and LCOs are caused by the appearance of a shock wave on the wing surface. The aeroelastic behaviour appears to become non-linear when the flow first becomes supersonic and disappears when the shock wave reaches the wing trailing edge.

6.2. Hawk

6.2.1. Overview

The transfer of methods to industry was an important objective of the PUMA research programme. The test case that was used to effect the transfer to BAE SYSTEMS was the Hawk trainer (Table 8). This family of aircraft entered service in

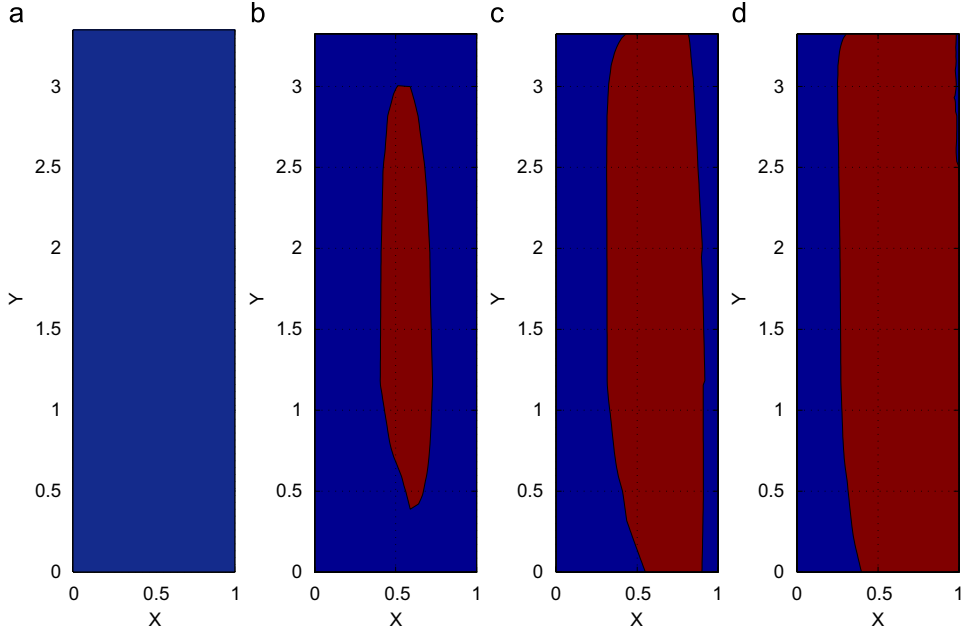


Fig. 47. Extent of supersonic flow over wing surface at four different Mach numbers: (a) M088; (b) M090; (c) M093; (d) M096.

1976. An exercise was embarked on with engineers from the Hawk project team to establish the methods for their use. In addition to potential future use for Hawk aeroelastic analysis, the transfer was intended to expose further developments needed for the methods to be routinely applicable in an industrial setting. An important aspect was to build confidence in the predictions.

On an existing military airframe, aeroelastic analysis is likely to focus on store combinations. In this case, for linear analysis, the structural model is modified and the aeroelastic analysis rerun without any change being needed for the doublet-lattice aerodynamics. The main effort involved in a CFD analysis is in the generation of a grid. For the exercise with the Hawk team it was decided to de-emphasise this aspect. Useful progress could be made by setting up at the outset a library of aircraft grids, and mapping these to the structural model. The effort in running a simulation for altered structural models was then reduced to changing the mode shapes, as in the linear case.

The library included grids generated for the components shown in Fig. 48. This allowed for a range of investigations, including low computational cost, wing only cases to full aircraft. A study of a control surface instability, rudder buzz, driven by shock motions, was also made.

This section describes the results of the exercise. It starts with an overview of the linear analysis, and then goes through a set of results obtained for the Hawk with increasing complexity. Finally, the achievements are summarised and next steps listed. In particular, the issue of CFD grid generation is considered.

6.2.2. Linear analysis

The Hawk aeroelastic model consists of a finite element structural model and a doublet-lattice unsteady aerodynamic model. The structural model is a half model of the starboard side of the aircraft. It is a beam model, with massless elastic beams representing fuselage, wing, fin, moving tailplane, and control surfaces. These beams are interconnected using springs, and the mass distribution is modelled with connected masses. The full aircraft is represented by applying appropriate constraints (boundary conditions) to the half model at all points in the plane of symmetry to provide symmetric or antisymmetric motion. This model has been constructed using NASTRAN software, in which an eigensolution provides the normal modes of vibration. Its extensive validation against GRT data, conducted over 30 years, has contributed to its maturity. Doublet-lattice panels are used to represent the unsteady aerodynamics on the wing, wingtip stores, tailplane, fin, aileron, flap, and

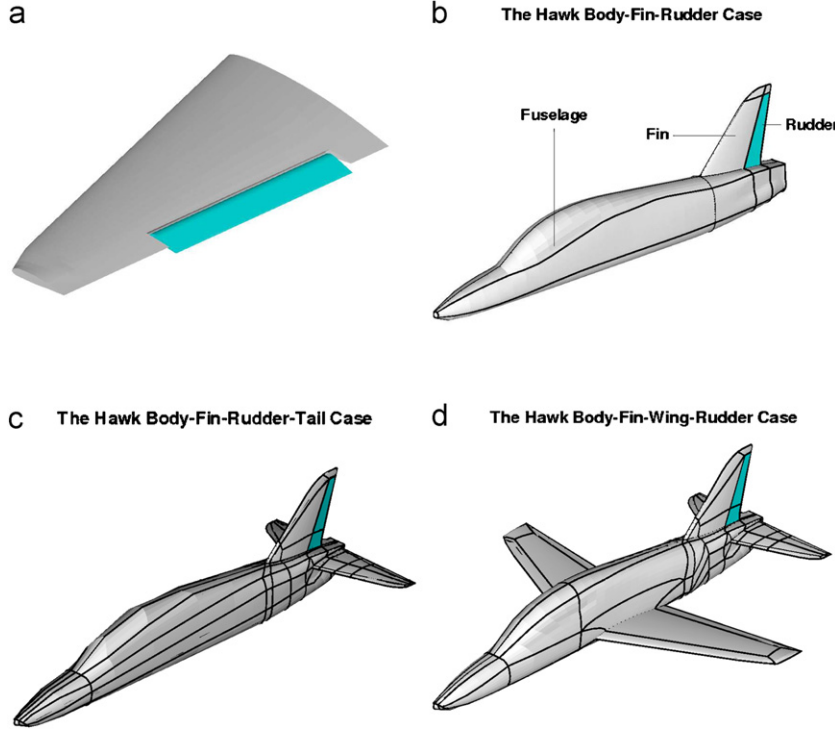


Fig. 48. Geometry of four of the Hawk CFD grid library cases: (a) combat flap; (b) body-fin-rudder; (c) body-fin-tail-rudder; (d) body-wing-fin-tail-rudder.

rudder. The aerodynamic forces are applied to the structure through grid points along the leading and trailing edges of the flying surfaces, splined to the flexible beams via massless rigid bars. There are no aerodynamic panels representing the fuselage. This unsteady aerodynamic model has been formulated in NASTRAN which, together with the structural model, is used to produce flutter solutions. The aeroelastic model was validated against flight flutter tests. If present, underwing stores and pylons are modelled using connected masses and springs. No aerodynamic panelling is applied to underwing stores. The NASTRAN structural model is shown in Fig. 49.

6.2.3. CFD grids

The CFD grids were generated using the commercial package ICEMCFD. The topologies used were of the O-type since this was found to concentrate points in the wing tip region where the accuracy for aeroelastic calculations is particularly important [151]. Of course, O-grids are not suitable for capturing wakes, but these were not of central importance for the current work. Views of the O-grid topology around a fuselage and the O-grid on the wing are shown in Fig. 50.

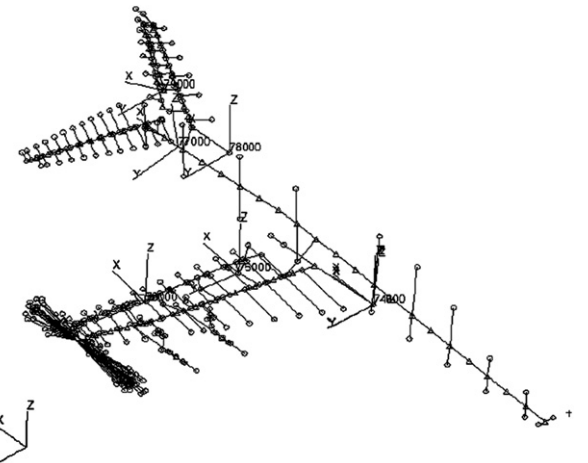


Fig. 49. NASTRAN structural model of Hawk aircraft.

All of these grids were mapped to the baseline structural model, following the methods described in Section 4.2.

6.2.4. Wing and wing–body–tail configurations

The initial calculations were reported in Ref. [102]. These focussed on the wing and wing–body–tail configurations, and the main purpose was

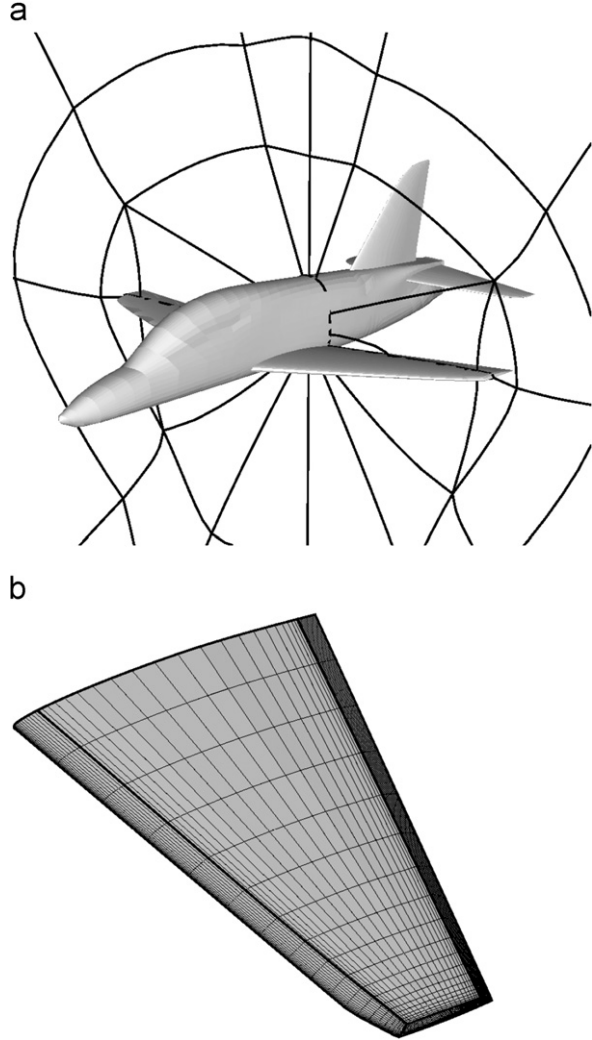


Fig. 50. View of O-grid topologies around fuselage and on wing [102]: (a) topology around fuselage; (b) surface grid on wing.

to benchmark predictions against linear results. A detailed grid and time step refinement study was reported in [102] and showed that the medium grid and 50 steps per flutter cycle give converged dynamic results. The flutter boundary for the wing only case is shown in Fig. 51. Important features of these results are:

- medium and fine grid predictions agree closely;
- CFD based and linear (Nastran) predictions agree at low Mach numbers;
- there is only a shallow transonic dip since the Hawk has a very rigid structure.

The structural model was artificially weakened and the flutter boundary retraced. These results are

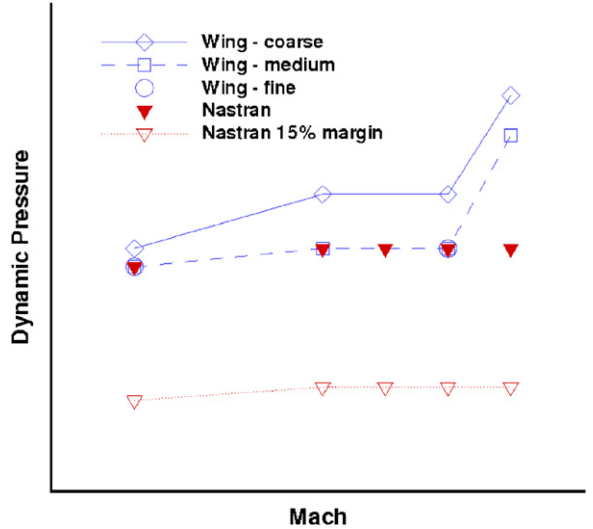


Fig. 51. Comparison between the flutter boundaries predicted using the linear method and the wing-only configurations for the original structural model [102].

shown in Fig. 52 and show the occurrence of a transonic dip where the CFD results dip below the linear predictions.

For each time-domain calculation, the CPU times were 1 h on a single processor, 9 h on a single processor and 16 h on eight processors on the sparse, medium and fine grids, respectively. These results demonstrated feasibility and built the confidence for further studies.

Direct calculations and damping responses using the methods described in Section 27 for the Hawk wing were reported in [148]. The time-domain stability boundary was reproduced, the reduced damping model was developed and compared with the full order results. At 98% of the flutter speed in the transonic range the response is already heavily damped. The damping model agrees very closely with the full order predictions, as shown in Fig. 53. However, by 95% of the flutter speed the critical eigenvalue has crossed over with another one, and the damping model predictions are no longer reliable. A full order time-domain calculation took around 10 h in this case whereas the equivalent reduced order calculation takes less than 20 s.

6.2.5. Combat flap

Wing bending-torsion flutter is unlikely to be a concern for an aircraft since this is precluded by strength requirements. Problems are more likely to involve the behaviour of a control surface, store or nacelle. A combat flap is included on the wing to

increase the realism and exercise the control surface treatment. The flap in the combat configuration is deflected 12.5° about an axis below the wing. In linear aeroelastic simulations the combat flap configuration cannot be modelled easily. This is because of the requirement of the linear unsteady method (Nastran Aeroelastic Analysis) that the flow be in the x -direction at all times. This means that a wing or a flap cannot have an angle of incidence. Thus a second geometry was constructed

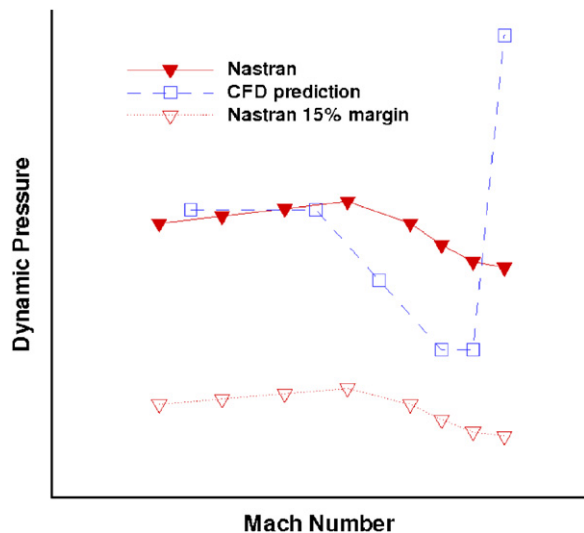


Fig. 52. Comparison between the flutter boundaries predicted using the linear method and the wing-only configurations for the weakened structural model [102].

with the flap at 0° deflection. CFD based aeroelastic analysis is performed for these two cases and compared with results from Nastran. The combat flap configuration on the aircraft is deployed in certain manoeuvres only and has constraints on the flight speeds within which it can be deployed. These flight speeds are limited to subsonic Mach numbers and shock induced instabilities on the combat flap configuration in transonic flows are of academic interest only.

A blended flap is used for the simulation of the wing with flap at 0° . It was illustrated in Section 4.5.3 that the aeroelastic predictions of blended flaps are comparable to a flap with free edges, however, they slightly underpredict the flutter velocity due to the larger aerodynamic surface area of the blended region. As the aircraft flies with the flaps undeployed at the full range of Mach numbers the aeroelastic predictions on this case are of practical interest.

Finally simulation is performed using the blended flap grid but excluding the flap structural nodes. This is done by mapping the aerodynamic nodes of the flap to the wing structural grid. This can be done by switching the two level transformation to a one level transformation where all the aerodynamic nodes are driven by the wing structural model alone. Practically this has the same effect as excluding the flap rotation from the aeroelastic calculations, although the structural influence of the flap modes on the wing motion will still be present.

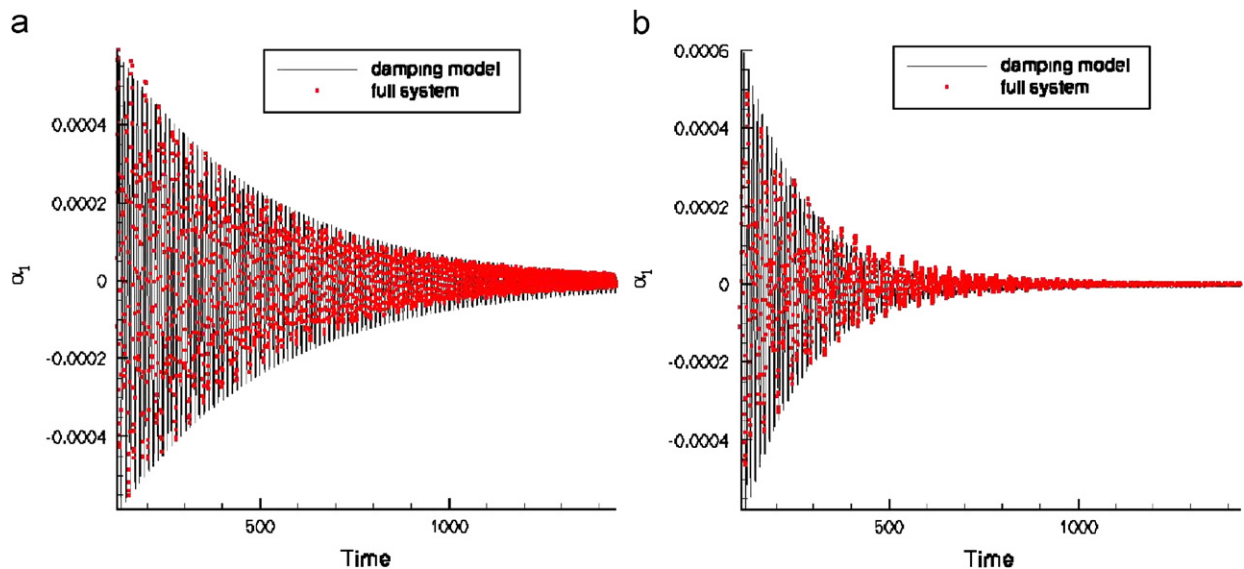


Fig. 53. Comparison of damped responses predicted by the full order system and the reduced (2 DoF) model at the bottom of the transonic dip [148]: (a) 98% of flutter speed; (b) 95% of flutter speed.

The purpose of analysing this case is to measure the increase in the flutter velocity when the control surface rotation is excluded.

The geometry of the Hawk wing with a combat flap was constructed by merging two geometries using the EZ-Cad package of ICEMCFD. First all the components from the complete aircraft CAD model were deleted except the wing, which was left intact. Then the combat flap, obtained separately from BAE SYSTEMS in the form of a large number of coordinates, was imported into EZ-Cad as points. A space for the flap to live inside the wing was created by cutting out the sections of the wing around the flap. A gap of approximately 2% of the flap span was left between the flap edge and the wing. A small groove was created ahead of the flap leading edge to conform to the original geometry which has a similar cavity. CFD simulations have shown that a twin vortex system sits inside this cavity. Discussions with engineers from BAE SYSTEMS established that aerodynamically this cavity does not have much influence on the flow over the flap and can be completely eliminated for current purposes. However, for the purpose of maintaining a smooth grid over the flap leading edge a shallow cavity was retained.

A C-H blocking over the wing and a separate C-H block over the flap ensures a smooth grid over the entire geometry. A three-block strategy is used on the wingtip and the inner edge of the wing in the wing-flap gap. This type of blocking avoids grid singularities on geometries where a plane collapses into a line or a point. The grid has 827,300 points and a coarse grid was extracted by removing every alternate point in the three directions, and has 117,800 points. There are 22,000 points on the wing and flap surface on the fine level and 5500 on the coarse level. A wall spacing of $10^{-3}c$, where c is the Hawk wing root chord, is used for the simulations.

For the case with the flap at 0° the blocking used is similar to the one used for the wing alone case. Additional flap blocks are added to define the flap edges over the wing. The flap edges are assumed to be blended with the wing. There are 3255 points on the wing and flap surface and 119,808 in the volume grid on the coarse level.

The structural model used here has been derived from the Hawk structural model described above. The wing root is constrained in all of the six degrees of freedom to isolate the wing and the flap modes from the rest of the aircraft structure. The flaps and the aileron are attached to the wing though only the

flap nodes are used in the simulation. The deformation in the aileron mode is not confined purely to the aileron. The wing and the flap deform also in this mode but not to the same magnitude as the aileron. Hence, even though aileron structural nodes are excluded from the mapping, the aileron mode itself is included. The first six modes are used for the analysis which includes the first wing bending, the first wing torsion and the flap rotation mode. For the sake of simplicity higher frequency modes have been excluded from the calculations.

The flap is attached to the wing at three hinge points. One of the hinges is spring loaded, representing the actuator stiffness which is assumed constant. Due to the smaller dimensions of the control surfaces as compared to the major components of the aircraft the control surface deformation modes have relatively higher frequencies. However, the control surface rotation modes depend on the hinge spring stiffness and are important for aero-elastic instabilities. The flap and the wing structural nodes are mapped to the flap and wing fluid nodes using a two-level mapping.

The flight envelope within which the combat flap configuration is deployed is limited to subsonic Mach numbers and the results presented here for transonic Mach numbers are purely of academic interest. The simulated flight conditions are outside the flight envelope and the results are not applicable to the real aircraft. The objective here is to simulate the shock induced effects on a deployed flap and to assess the effect of the deployed flap on the flutter boundary. Fig. 54 shows the flutter boundaries for the combat flap configuration predicted using Nastran and CFD. The comparison is reasonable at subsonic Mach numbers. At a certain transonic Mach number the CFD prediction shows a large drop in the flutter velocity which is due to a small amplitude LCO of the flap. In contrast Nastran predicts a peak in the flutter velocity at this Mach number. Moreover, the Nastran method breaks down at low supersonic Mach numbers due to the limitations of the linearised supersonic aerodynamic theory. The amplitude of the oscillations in the CFD based simulation depends on the dynamic pressure. However, the decrease in the amplitude, is asymptotic and a finite amplitude exists even at very low values of the dynamic pressure (see Fig. 55).

A cross section through the wing-flap shows a well defined shock standing at the wing trailing edge inducing a strong separation over the entire flap surface (see Fig. 56). The unsteady separated flow

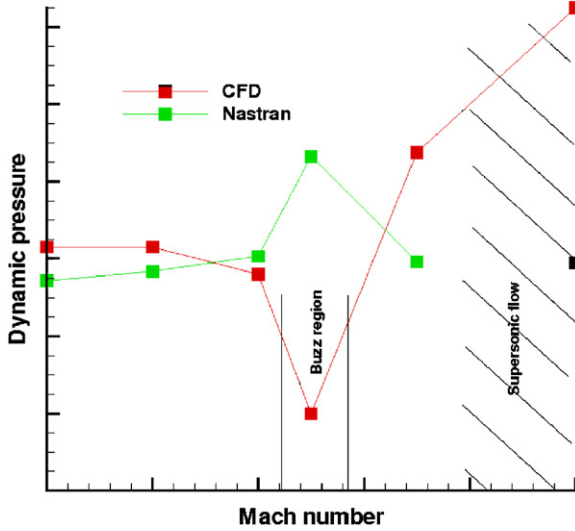


Fig. 54. Flutter boundaries for the Hawk wing combat flap configuration using linear and CFD methods.

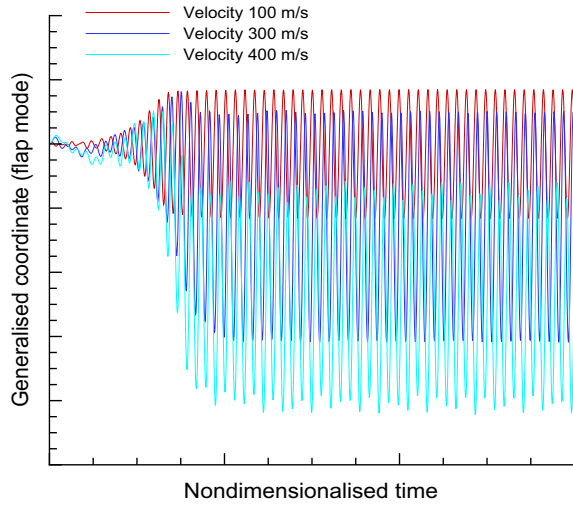


Fig. 55. Limit cycle oscillations of the combat flap configuration on the Hawk wing at a transonic Mach number.

over the flap drives the flap to result in a LCO. The frequency of the oscillations was found to be very high suggesting that the instability is driven mainly by the unsteadiness in the flow. For matched conditions at transonic Mach numbers the frequency of oscillations was twice the natural frequency of the flap oscillations. The shock here stands ahead of the flap hinge hence according to Lambourne's classification it can be termed as a Type A buzz. In the current case the separation is caused by a combination of the sharp trailing edge of the wing, a strong shock and the deflected flap.

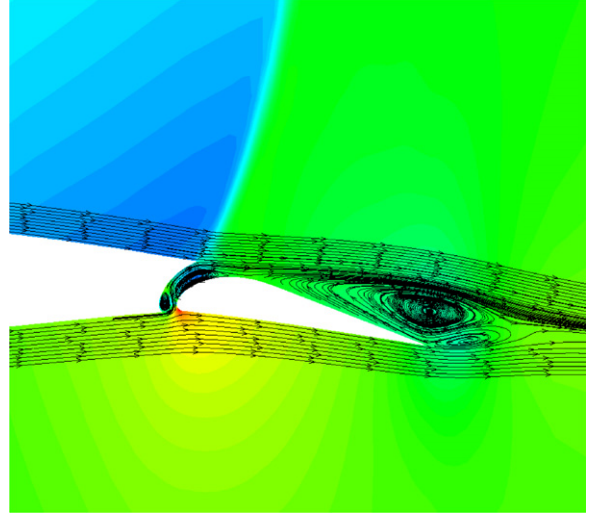


Fig. 56. Shock induced separation at the flap hinge at transonic Mach number.

Separation of the boundary layer is not involved. It is seen here, that like the simulation of the non-classical buzz for the SST described above, a qualitative evaluation of classical buzz is possible using the Euler equations. However, for accurate results with regards to amplitude of oscillations and frequencies modelling of the viscous effects is necessary. Once again it should be stressed that the aircraft does not fly at transonic Mach numbers with a combat flap configuration due to the structural constraints.

Fig. 57 shows the flutter boundary for the wing with flap at 0° deflection. The linear boundary here is the same as for the combat flap configuration. It is seen that the buzz instability is absent from the CFD results. It is also seen that there is no shock induced separation on the flap hinge observed in the combat flap configuration (see Fig. 58). Absence of a separation bubble together with the fact that no LCO was observed in the case with 0° flap deflection at transonic Mach numbers suggests that a mean flap angle greater than 0° is necessary for the Type A buzz to occur. The flutter boundary compares reasonably with the linear results in the subsonic region. The CFD analysis predicts a shallow transonic dip which is not present in the Nastran results. As in all cases analysed so far the linear method predicts a large drop in the flutter velocity at low supersonic Mach numbers.

Finally Fig. 59 shows the flutter boundary for the case when the flap structural nodes and hence the flap rotation is excluded from the analysis. The

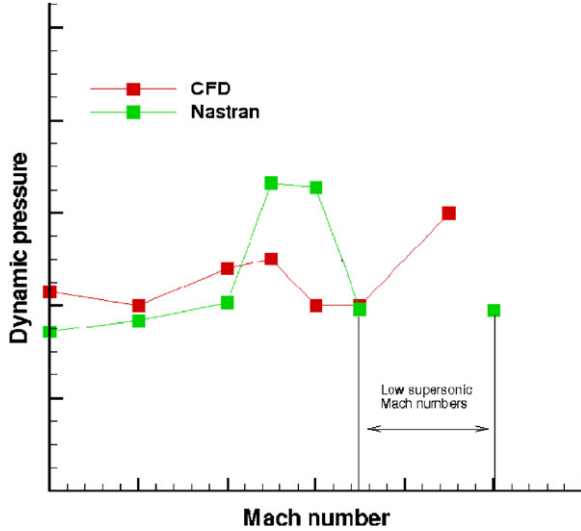


Fig. 57. Flutter boundaries of the Hawk wing with flap at 0° using linear and CFD methods.

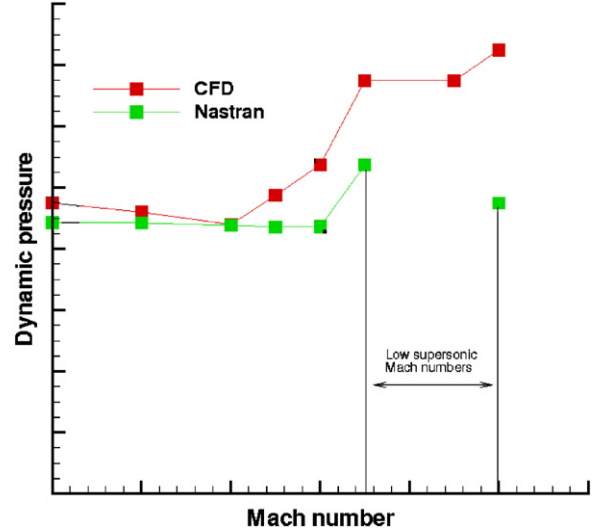


Fig. 59. Flutter boundaries using linear and CFD methods of the Hawk wing with the flap and aileron aero-structural relations replaced by a full planform wing arrangement.

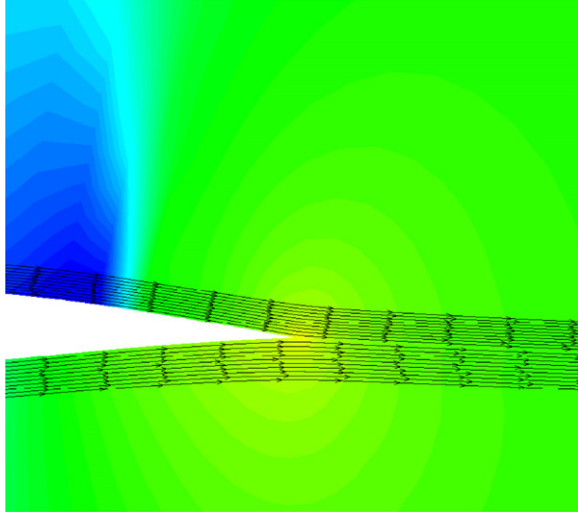


Fig. 58. Attached flow all along the flap at transonic Mach number when the flap is undeployed.

flutter velocity increases to almost twice when compared to the flap cases. The transonic dip seen in the case with the flap is absent here as in the wing alone case. This is due to the fact that the modes and the structural behaviour are similar to the wing alone case. The general increase in the flutter velocities as seen in Fig. 60 for all Mach number underscores the importance of the control surface modes to the aeroelastic response. The difference in the flutter velocities for the case without the flap and the cases with flap is due to the differences in the structure model. The flap cases have the flap

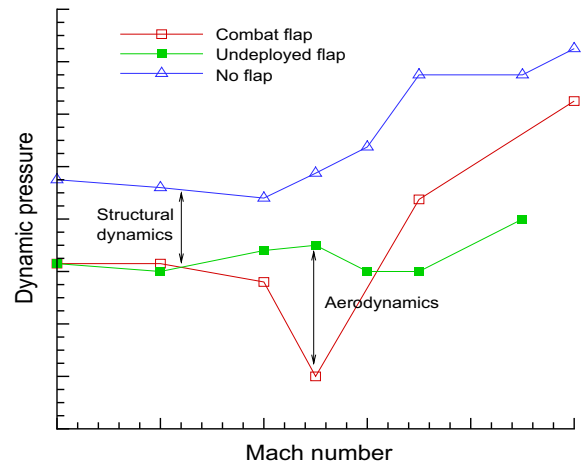


Fig. 60. Comparison of the flutter boundaries for the Hawk combat flap case, the Hawk wing with 0° flap deflection and the Hawk wing with the full planform wing replacing the separate flap grid using CFD.

rotation mode which is absent in the wing alone case. The transonic dip due to the shock induced LCO in the combat flap configuration is absent in the case with flap at 0° . The differences in the predicted aeroelastic response between these two cases at transonic Mach numbers are due to the different aerodynamics.

6.2.6. Rudder buzz

The dynamic simulation of rudder buzz was reported in [182]. Fuglsang [183] reported on rudder

oscillations for the T-45A Goshawk which arose at Mach 0.95 and 20,000 feet altitude during a development flight test program. He used steady state RANS simulations to investigate this for a configuration involving only the fuselage, fin and rudder (i.e. no wings or tailplane). Strong shocks were seen to go onto the rudder at the conditions of buzz and it was therefore concluded that this was the cause of the buzz. Based on this conclusion shock strips were then designed to resolve the buzz.

The study reported in [182] investigated the simplified configuration, found a very similar shock structure on the fin and predicted buzz through time marching simulations. However, it then went on to investigate a more complete configuration, including the wings and tailplane, and the buzz onset was shifted to higher Mach numbers. This was attributed to the shock on the wing changing the flow seen by the fin, and thereby changing the flow pattern on the fin.

6.2.7. Perspective

The objective of transferring methods to BAE SYSTEMS was met. A library of grids was generated and mapped to a standard structural grid. This allowed different configurations to be studied through modifications to the structural modes only. This approach is typical of production (linear) flutter investigation and allowed progress to be made. Careful numerical tests and comparison with linear predictions in the subsonic regime provided confidence in the new methods.

The remaining challenge is to make the treatment routine of different geometries in the CFD simulation. Plans to achieve this centre on the BAE SYSTEMS developed grid generator SOLAR [15]. This software has made the generation of grids around very complex geometries far more routine. The grid around the configuration shown in Fig. 61 was generated from the CAD model in a day. The grid features large areas of hexahedra, but also has polyhedral cells. The CVT transformation does not rely on the multiblock structure and will generalise straight away to SOLAR grids. New methods will be required for the grid movement, which cannot now be based on TFI. Finally, the methods of section 27 rely on the calculation of Jacobians and the solution of sparse linear systems. The grid type will influence the sparsity pattern of matrix, but not fundamentally the algorithms.

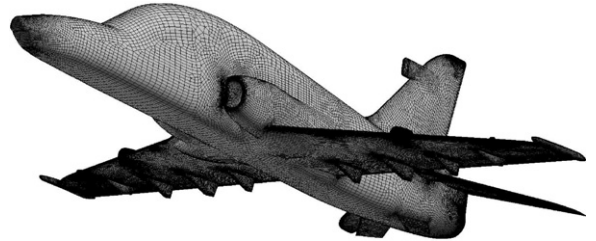


Fig. 61. SOLAR grid.

6.3. MDO analysis

The various time domain and fast flutter methods discussed in the previous sections were all tested against the AGARD445.6 wing. As has been described, this test case is widely used, but also is not very representative of real world aircraft designs. A more demanding test case bearing a greater resemblance to modern transonic design is available through the MDO aircraft design. This aircraft was designed in a Brite-Euram project to establish design methodology for future large commercial aircraft. As a part of this project, the wing alone was extracted from the rest of the vehicle, and structural and aerodynamic interactions studied. The MDO wing is typical of modern, transonic design, and was used in the unsteady flow in the context of fluid–structure interaction (UNSI) project as a test case for coupled CFD–CSD simulations. Comparison of the results achieved by the various methods employed by the partners in the project can be found in several Refs. [80,81,184]. This previous work provided a suitable background data set against which the time-domain and fast flutter methods discussed elsewhere in this paper could be compared, on a test case providing many of the challenges in terms of structural interactions common in current and future industrial practise.

6.3.1. Time-domain methods

Results from the UNSI group fell into three main sets; steady deflections, pressure distributions around sections at various spanwise locations, and dynamic responses to the excitation of the first structural mode. All of these sets were examined for three test cases corresponding to different parts of the flight envelope (an extra case, Case 4 in Table 10, was devised specifically for the PUMA DARP project). In total, eight different solution techniques were compared, ranging from fully coupled Euler-FE analysis to transonic perturbation

methods coupled to modal structural representations. Notable differences were produced by the various methodologies utilised, even for the relatively simple steady response cases. Various possible explanations were proposed, ranging from the accuracy with which the flow solution method calculates the load, the accuracy and effectiveness

of the interpolation method, in terms of displacement and force transfer, and the structural representation itself. Results for various conditions produced by RANSMB and PMB are shown in Figs. 62 and 63, compared to results from SAAB and ONERA from the UNSI project (these latter were selected as they had the greatest similarity to RANSMB and PMB, as they used Euler-modal solution).

In general it was found that; agreement between PMB and RANSMB was generally excellent, and closer than had been achieved during the UNSI programme. This is despite the fact that the solver methodologies differ in several significant areas—for instance RANSMB employs central differencing, whereas PMB is upwind. However, the areas of similarity lie most significantly with the mesh

Table 10
Conditions for MDO test cases

	Case 1	Case 2	Case 3	Case 4
Mach number	0.85	0.88	0.88	0.3
Lift coefficient	0.4581	0.3263	0.1686	0.4581
Aircraft mass (tons)	371	537	537	—
Altitude (km)	11.27	7	2	11.27

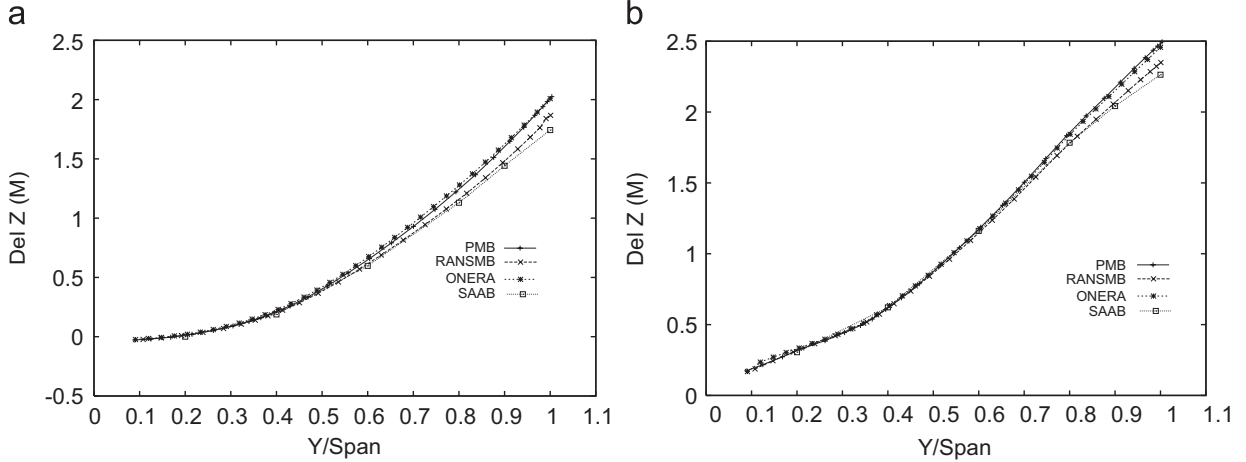


Fig. 62. Tip deflections, MDO Case 3: (a) leading; (b) trailing.

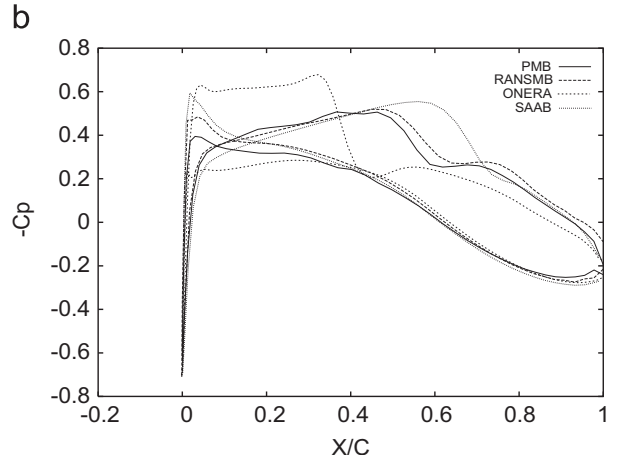
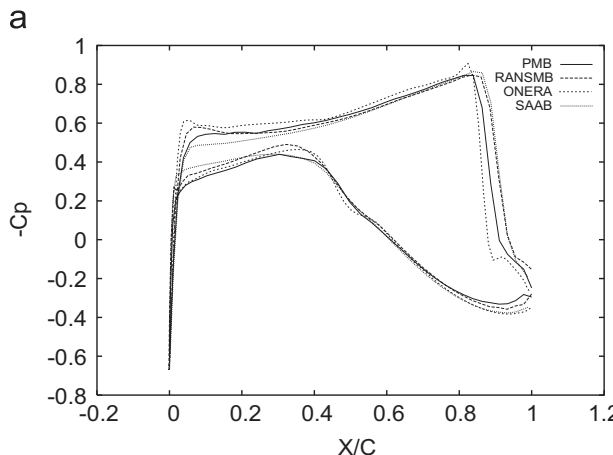


Fig. 63. Pressure distributions, MDO Case 2: (a) 40% span; (b) 90% span.

motion schemes—both employ moving meshes, and both employ CVT based interpolations (there are some slight differences in implementation, but the schemes are substantively similar). This suggests that the most important issue in generating consistent results between different methods is the intergrid transfer method. This is a significant point, as it is believed that this is the answer to the question posed in the UNSI work.

PMB and RANSMB were then used to generate flutter boundaries for the MDO wing, assuming zero incidence initial conditions and an atmospheric density of 1.006 kg m^{-3} . The results are shown in Fig. 64. Unfortunately, due to the virtual nature of the MDO design, no experimental data exists for comparison. However, the good agreement demonstrated between the two codes again here does add to the general point that accurate mesh motion and intergrid transfer of loads and deflections are highly important for consistency at least of disparate coding schemes in aeroelastic analysis.

Comparing commercial linearised codes with the time marching methods has revealed strengths and weaknesses of such methods. Much more rapid solution is possible, at the cost of sacrificing some accuracy, particularly at transonic Mach numbers. Although an intermediate methodology based on updating the linear solution with non-linear steady state pressure distribution goes some way to remedying this, due to the limitations associated with small disturbance solutions, this cannot in itself resolve the problems in their entirety. Furthermore, any phenomena which involves larger scale motions (e.g. LCO prediction, etc.) cannot be modelled as a small disturbance.

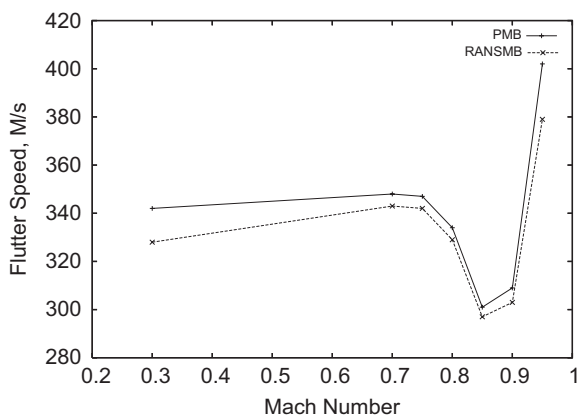


Fig. 64. Flutter boundaries, $\alpha = 0^\circ$, $\rho = 1.006 \text{ kg m}^{-3}$.

6.3.2. Fast flutter methods for the MDO civil aircraft wing

The MDO wing presents a more challenging test case for the coupled ROMSI method than the previous AGARD445.6, due to the increased complexity of the wing aerodynamics and structure (being neither thin nor symmetrical). The wing is of thick super-critical section, and as has been shown above this produces a greater variation in solution between the coupled Euler solver and conventional linearised aerodynamic theory, compared to the AGARD445.6 wing. However, in terms of the fast flutter technique, it is the lack of symmetry which is the real test.

In the previous AGARD445.6 test case the symmetrical section and zero incidence meant that variations in the dynamic pressure made no difference to the steady state position of the wing. This meant that the ROMSI assumption of dynamic linearity was independent of static pressure and hence also independent of the dynamic pressure for a fixed Mach number. For the MDO wing the steady state position, about which the dynamic linearity assumption is made, is dependent on the pressure because of the asymmetry of the wing. This means that the ROMSIs created about a steady solution at a particular pressure may not be valid for perturbations about the steady solution at a different pressure. Formally, the ROMSI would only be equivalent to the non-linear model for flutter prediction if the dynamic pressure of flutter were known *a priori* and used to form the steady coupled solution. In practice ROMSI flutter prediction becomes an approximation which remains accurate for as long as the dynamic linearity holds as a good approximation.

The flutter boundary for the full non-linear Euler equations is plotted in Fig. 65. Also plotted on this figure are a number of typical ROMSI flutter boundaries. These show the variation in flutter boundary location for differing numbers of time steps (N) used to create the ROMSI and differing rank (M) of ROMSI retained. It was found that the flutter boundary did not change until less than 20 time steps were used to generate the ROM. Using 20 or less time steps meant that the flutter boundary became more sensitive to the rank of the ROMSI used. Also shown in Fig. 65 is the freestream pressure used to generate the steady coupled solution about which the ROMSIs are generated, this is approximately 15% higher than the actual flutter boundary. Fig. 65 demonstrates that the

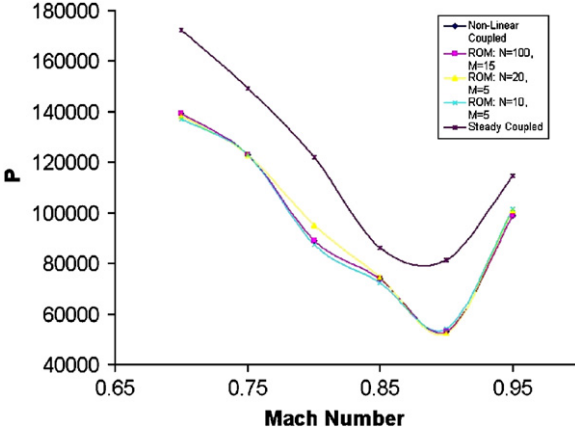


Fig. 65. Flutter boundary variation for ROMSI with number of time steps used (N) and the number of aerodynamic modes retained (M). Q used for static calculation also shown.

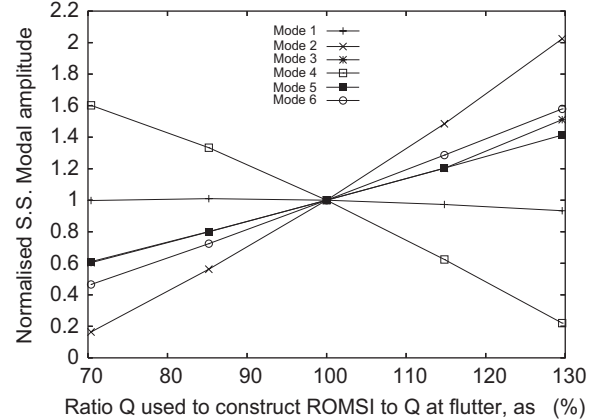


Fig. 67. Steady state modal displacement for the first six modes against Q , freestream Mach number is 0.85. Modal displacements normalised against the displacements at the flutter Q , Q shown as a percentage of Q flutter.

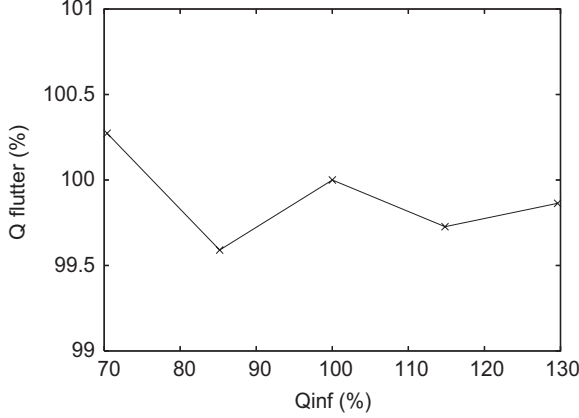


Fig. 66. Variation of Q for flutter against Q used to define the steady state for a freestream Mach number of 0.85.

flutter boundary for the MDO wing seems insensitive to the correct identification of the steady coupled solution. This is further investigated at the design Mach number of 0.85.

Fig. 66 plots the dynamic pressure of flutter against the dynamic pressure which gives the steady coupled calculation used in ROM construction. Dynamic pressures are normalised using the flutter value calculated from the full non-linear time histories. It can be seen that variations in the dynamic pressure used to calculate the steady solution, of up to 30%, make less than 0.5% difference to the predicted flutter boundary. Initially it was unclear whether the insensitivity of the ROMSI flutter boundary was due an insensitivity

of the steady modal displacement to the dynamic pressure. To demonstrate the steady coupled behaviour of the wing, the modal displacements are plotted against the dynamic pressure used for the steady coupled solution in Fig. 67. The modal displacements and dynamic pressure are normalised by the values at the flutter boundary. Fig. 67 demonstrates significant variation in the mean displacement and therefore suggests that, at least for the MDO case, the flutter is insensitive to a reasonably selected dynamic pressure used for ROMSI construction.

7. Summary and general conclusions

We draw some general conclusions from the work above concerning the maturity of the methods and the practicalities of their deployment within industry. Technical conclusions about individual methods and/or approaches have been made in the relevant sections of this paper. The need for non-linear aeroelastic prediction has been established and various approaches researched to meet that need. It has been our intention throughout to identify practical approaches that are applicable to real problems, guided by the PUMA objectives (Section 1.1). These can be summarised as the development of usable methodologies evaluated for real aircraft problems, and to investigate the effects of non-linearities as they affect the flutter qualification process. It must always be borne in mind that the term usable is not restricted to validity, accuracy, etc., but in this case is strongly

linked to affordability. This is determined by the stage within the overall qualification process (Fig. 2) within which the method in question is being applied. In stage 1 (See Fig. 2), where the aerodynamic data may be reasonably accurate, but the structural data are still under development, then fast methods to examine a wide range of cases in support of the design are required. The general rule has been that absolute accuracy may be compromised in relation to speed of calculation at this stage. Essentially the methods are needed to identify potential problem ‘cases’ and give guidance on the constraints that aeroelastics may impose on the design. In the past, the identification of problem case has been severely limited by the linear nature of the methods employed. More accurate methods are applicable at stage 2, where the structural data are more reliable and detailed calculations may also be required for specific conditions. At stage 3, accurate calculations may be needed to explore unexpected results, but ideally the prediction at stages 1 and 2 should have been sufficient to ensure that there are no ‘unexpected’ results. In a sense, this discussion indicates the method and process improvements required. Methods that enable more reliable identification of potential problem cases early in the design cycle are needed, and the inclusion of non-linear capability is an important step in that direction. Efficient methods for detailed calculation at problem condition, with appropriate interrogative capability to allow the problems to be thoroughly understood and hence solved are also required. These capabilities will allow improved designs through earlier consideration of aeroelastic constraints and hence design to minimise these constraints. To accompany the research and method development, we have established a set of test cases chosen to exercise the methods against different challenges: aerodynamics non-linearity, structural non-linearity, geometric complexity, and whole aircraft capability. This included the challenges associated with flap movement, which is an important consideration given that a significant proportion of flutter incidents are associated with control surfaces. The focus of this programme has, however, been biased towards aerodynamic non-linearity and an extension of this work should incorporate more structural and/or FCS non-linearity. Time-domain methods (coupled CFD-CSM) have already enjoyed some limited use in industry, but the work reported here tackles

some important questions and constraints concerning grid movement and accurate coupling schemes. Within the multiblock approach adopted we found that a combination of spring analogy for block boundaries and TFI within the blocks was the most reliable approach and significant component movement was achieved using this. The methods were extended to allow control surface movement and our conclusion was that although a sliding plane approach offers slightly greater accuracy, the blended mesh provides efficiency gains that outweigh the slight accuracy differences. For transformation the CVT scheme has been established as reliable and accurate. Although the work to enhance the CVT method for cases where the simplified structural model exhibits detrimental behaviours for coupled calculations might seem slightly superfluous, in fact it is very important in terms of industrial exploitation of the method. An obvious solution to the problem of the simplified structural models seems, at first sight, to be simply a detailed structural model, but a pragmatic approach that acknowledges the cost of updating legacy models has been found to be advantageous. Through detailed comparisons of the time-domain results for the MDO test case, we have established that differences observed in previous studies [80,81] were due to different approaches to fluid–structure coupling, rather than differences in the CFD predictions. This is important because it demonstrates clearly the importance of the coupling scheme and the need to isolate the role of this part of the method in any validation exercise. Overall, the advances reported herein for the time-domain methods represent good steps forward in terms of their usability for aeroelastic prediction within industry. The calculation of the Hawk aircraft, using PMB, is thought to be the first UK calculation of this complexity, using this approach, and the code has now been successfully deployed into industry, with appropriate training provided to the engineers by the academic development team. Despite significant improvements in the efficiency of the time domain methods, they still remain about two orders of magnitude too slow for routine use in stage 1 as a means of including non-linearity within a parametric sweep to determine the flutter boundary. It was this need that originally motivated the work on the methods we have terms ‘fast’ methods that include non-linearity. During the programme those fast methods which make an *a priori* assumption about the nature of the aeroelastic instability

(i.e. Hopf and ROMSI) have been developed to the level of maturity where large DOF calculations are possible. The agreement between these results and the full time-domain solutions has been consistently good and the calculation times indicate that these methods can realistically be used for flutter prediction in the design/qualification environment. This makes the inclusion of non-linearity in the early design stages a realistic possibility. The Hopf bifurcation based method is now being deployed on real aircraft problems, so that a usable methodology that incorporates non-linearity is now feasible. This has reached a sufficient maturity for it to be used within research activities, if not yet design, in the industrial environment. Both the Hopf based and ROMSI methods require efficient time-domain solutions to be generated as a starting point for the procedure. PMB and RANSMB codes adequately fulfil this role and the extension to unstructured grids, that are now more appropriate to industrial practice, is underway. Clearly, the realisation of fast methods, in which no *a priori* assumption of the nature of the instability is necessary, represents the ultimate goal of this work. This capability would provide a highly versatile design tool that allowed aeroelastic considerations to be accounted for accurately from the very beginning of the design activity, essentially removing the need for substantial safety margins due to non-linearity. So far, these methods (HOHB and continuation) have only been used for cases with few DOFs, and these methods are probably some years from industrial exploitation. Nevertheless, our work has indicated that the continuation method offers the more likely route to many DOFs, realistic configuration cases. It is important to view the combination of the time-domain methods, fast methods, and the existing linear tools not as a set of competing methods, but as a set of complementary tools that the engineer can deploy within the overall design and qualification process. These provide the quick ‘look and see’ methods through to the detailed calculation of problem or unexplained cases on complex configurations. The suite of methods developed here have been used to investigate the nature of non-linearity, though more extensive work is required, which is an important aspect of the ability to solve aeroelastic problems as such insights enable the development of design solutions. Overall the objectives of the PUMA aeroelastics programme have been achieved and industrial exploitation of the methods researched

and developed has begun. The areas requiring further research are:

- application of methods to a greater range of structural non-linearities;
- inclusion of FCS within the methods so that aeroservoelastic problems may be tackled;
- extension of the fast methods to real aircraft problems;
- application of the methods in the context of using aeroelastics positively (e.g. morphing wings, active aeroelastic surfaces, etc.).

In terms of the qualification process, in which this project was anchored, the progress has been sufficient for the consideration of non-linearity to be based on a more sophisticated premise than a conservative safety margin. But for the full benefits to be realised, the next step must be engagement of the standards community in order that the standards are developed beyond the linear assumptions currently embodied within them.

Acknowledgments

This work was supported by BAE SYSTEMS, Airbus UK, Engineering and Physical Sciences Research Council, Department of Trade and Industry and Ministry of Defence, and is part of the work programme of the Partnership for Unsteady Methods in Aerodynamics (PUMA) Defence and Aerospace Research Partnership (DARP). We are very grateful for the technical support and guidance provided by Prof. J.T. Cansdale, of DSTL, throughout this research.

References

- [1] Lanchester FW. Torsional vibrations of the tail of an aeroplane. Selected reprint series, Aerodynamic flutter. vol. V, New York: AIAA; 1969. p. 12–5.
- [2] Keynes IW. Private papers.
- [3] Haase W, Selmin V, Winzell B (editors.). Progress in computational flow-structure interaction: results of the project UNSI supported by the European Union 1998–2000. Notes on numerical fluid mechanics and multidisciplinary design, vol. 81, New York: Springer; 2002.
- [4] Farhat C, Geuzaine P, Brown G. Application of a three-field nonlinear fluid-structure formulation to the prediction of the aeroelastic parameters of an F-16 fighter. Comput Fluids 2002;32(3):3–29.
- [5] Bisplinghoff RL, Ashley H, Halfman RL. Aeroelasticity. New York: Dover Publications; 1955.
- [6] Fung Y. An introduction to the theory of aeroelasticity. New York: Dover; 1969.

- [7] Collar A. The first 50 years of aeroelasticity. *Aerospace* 1978; 12–20.
- [8] Garrick IE, Read WH. Historical development of aircraft flutter. *J Aircr* 1981;18(11):897–912.
- [9] Friedmann PP. Renaissance of aeroelasticity and its future. *J Aircr* 1999;36(1):105–21.
- [10] Bhatia KG. Airplane aeroelasticity: practice and potential. *J Aircr* 2003;40(6):1010–8.
- [11] Livne E. Future of airplane aeroelasticity. *J Aircr* 2003; 40(6):1066–92.
- [12] Dowell EH, Hall KC. Modelling of fluid-structure interaction. *Ann Rev Fluid Mech* 2001;33:445–90.
- [13] Keynes IW. Review of aeroelasticity in the UK. Internal Report, QinetiQ; 2001.
- [14] Ashley H. Role of shocks in the sub-transonic flutter phenomena. *J Aircr* 1980;17:187–97.
- [15] Shaw J, Stokes S, Lucking M. The rapid and robust generation of efficient hybrid grids for RANS simulations over complete aircraft. *Int J Numer Meth Fluids* 2003;43(6).
- [16] Ministry of Defence Standard 00-970 Design and Airworthiness Requirements for Service Aircraft, UK Defence Standardization.
- [17] Military Specification Airplane Strength and Rigidity Mil-A.
- [18] Certification Standards For Large Aeroplanes CS-25, European Aviation Safety Agency.
- [19] Part 25—Airworthiness Standards, Transport Category Airplanes, Federal Aviation Administration Department of Transportation.
- [20] Bairstow L, Fage A. Oscillations of the tailplane and body of an aircraft in flight. *ARC R&M* 1916;276(2).
- [21] Yates EC. Modified strip analysis method for predicting wing flutter at subsonic to hypersonic speeds. *J Aircr* 1966; 3(1):25–9.
- [22] Katz J, Plotkin A. Low speed aerodynamics. 2nd ed. Cambridge, MA: Cambridge University Press; 2001.
- [23] Albino E, Rodden WP. A doublet-lattice method for calculating lift distributions on oscillating surfaces in subsonic flows. *AIAA J* 1969;7(2):279–85.
- [24] Yurkovitch R. Status of unsteady aerodynamic prediction for flutter of high performance aircraft. *J Aircr* 2003;40(5): 832–42.
- [25] Hassig HJ. An approximate true damping solution of the flutter equation by determinant iteration. *J Aircr* 1971; 8(11):885–9.
- [26] Blair M. A compilation of the mathematics leading to the doublet lattice method. WI-tr-95-3022, Air Force Wright Laboratory, 1994.
- [27] Dowell EH, Tang D. Nonlinear aeroelasticity and unsteady aerodynamics. *AIAA J* 2002;40(9):1697–1707.
- [28] Dowell EH, Edwards J, Strganac T. Nonlinear aeroelasticity. *J Aircr* 2003;40(5):857–74.
- [29] Conner MD, Tang DM, Dowell EH, Virgin L. Nonlinear behaviour of a typical airfoil section with control surface freeplay: a numerical and experimental study. *J Fluids Struct* 1997;11:89–109.
- [30] Holden M, Brazier R, Cal A. Effects of structural nonlinearities on a tailplane flutter model. In: International forum on aeroelasticity and structural dynamics, no. 60, 1995.
- [31] Denegri CM. Limit cycle oscillation flight test results of a fighter with external stores. *J Aircr* 2000;37(5):761–9.
- [32] Chen PC, Sulaeman E, Lui DD, Denegri CM. Influence of external store aerodynamics on flutter/LCO of a fighter aircraft. In: Proceedings of the (43rd AIAA/ASME/ASCE/AHS/ASC structures, structural dynamics & materials conference. Colorado: Denver; 2002.
- [33] Dunn SA, Farrell PA, Budd PJ, Arms PB, Hardie CA, Rendo CJ. F/A-18A flight flutter testing limit cycle oscillation or flutter? In: International forum of aeroelasticity and structural dynamics, 2001. p. 193–204.
- [34] Tang D, Attar P, Dowell EH. Flutter/limit cycle oscillation analysis and experiment for wing-store model. *AIAA J* 2006;44:1662–75.
- [35] Dawson KS, Maxwell DL. Limit cycle oscillation prediction using analytic eigenvector descriptors in artificial neural networks. In: International forum on aeroelasticity and structural dynamics. Munich, Germany, 2005.
- [36] Denegri CM, Johnson MR. Comparison of static and dynamics neural networks for limit cycle oscillation prediction. *J Aircr* 2003;40(1):194–203.
- [37] Dawson KS, Maxwell DL. Limit cycle oscillation prediction of asymmetric external store configurations using neural networks. In: Proceedings of the 47th AIAA/ASME/ASCE/AHS/ASC structures, structural dynamics & materials conference, Newport, RI, 2006.
- [38] Dawson KS, Maxwell DL. Limit cycle oscillation flight test results for asymmetric store configurations. *J Aircr* 2005; 42(6):1589–96.
- [39] Parker GH, Maple RC, Beran PS. Analysis of store effects on limit cycle oscillations. In: Proceedings of the 47th AIAA/ASME/ASCE/AHS/ASC structures, structural dynamics & materials conference, Newport, RI, 2006.
- [40] Janardhan S, Grandhi RV, Eastep F, Sanders B. Design studies of transonic flutter and limit cycle oscillation of an aircraft wing/tip store. In: 44th AIAA/ASME/ASCE/AHS/ASC Structures, Structural Dynamics & Materials Conference, Norfolk, VA, 2003.
- [41] Beran P, Khot N, Eastep F, Snyder R, Zweber J. Numerical analysis of store induced limit cycle oscillation. *J Aircr* 2004;41(6):1315–26.
- [42] Kim K, Nichkawde C, Strganac T. Effect of external store on nonlinear aeroelastic responses. In: Proceedings of the 45th AIAA/ASME/ASCE/AHS/ASC structures, structural dynamics & materials conference, Palm Springs, California, 2004.
- [43] Kim K, Strganac T. Nonlinear responses of a cantilever wing with an external store. In: Proceedings of the 44th AIAA/ASME/ASCE/AHS/ASC structures, structural dynamics & materials conference, Norfolk, Virginia, 2003.
- [44] Melville R. Nonlinear simulation of F-16 aeroelastic instability. In: 39th aerospace sciences meeting and exhibit, Reno, Nevada, 2001.
- [45] Pranata BB, Kok JC, Spekreijse SP, Hounjet MHL, Meijer JJ. Simulation of limit cycle oscillation of fighter aircraft at moderate angle of attack. Technical Report NLR-TP-2003-526, National Aerospace Laboratory, Amsterdam, Holland; 2006.
- [46] Goura GSL, Badcock KJ, Woodgate MA, Richards BE. Implicit method for the time marching analysis of flutter. *Aeronaut J* 2001;105(1046):199–214.
- [47] Romanowski MC. Reduced order unsteady aerodynamic and aeroelastic models using Karhunen-Loeve eigenmodes. In: 6th symposium on multidisciplinary analysis and optimization, Bellevue, WA, 1996.
- [48] Romanowski MC, Dowell EH. Reduced order Euler equations for unsteady aerodynamic flows: numerical

- techniques. In: 34th aerospace sciences meeting and exhibit, Reno, Nevada, 1996.
- [49] Hall KC, Thomas JP, Dowell EH. Reduced-order modelling of unsteady small disturbance flows using a frequency domain proper orthogonal decomposition technique. In: 37th aerospace sciences meeting and exhibit, Reno, Nevada, 1999.
- [50] Hall KC, Thomas JP, Dowell EH. Proper orthogonal decomposition technique for transonic unsteady aerodynamic flows. *AIAA J* 2000;38(10):1853–62.
- [51] Willcox K, Peraire J. Balanced model reduction via proper orthogonal decomposition. In: 15th AIAA computational fluid dynamics conference, Anaheim, CA, 2001.
- [52] Schmidt R, Glauser M. Improvements in low dimensional tools for flow structure interaction problems using global POD. In: 42nd AIAA aerospace sciences meeting and exhibit, Reno, Nevada, 2004.
- [53] Lieu T, Farhat C. POD-based aeroelastic analysis of a complete F-16 configuration: ROM adaptation and demonstration. In: Proceedings of the 46th AIAA/ASME/ASCE/AHS/ASC structures, structural dynamics & materials conference, Austin, Texas, 2005.
- [54] Silva W, Stroganac T, Hajj M. Higher-order spectral analysis of a nonlinear pitch and plunge apparatus. In: Proceedings of the 46th AIAA/ASME/ASCE/AHS/ASC structures, structural dynamics & materials conference, Austin, Texas, 2005.
- [55] Silva W, Dunn S. Higher-order spectral analysis of F-18 flight flutter data. In: Proceedings of the 46th AIAA/ASME/ASCE/AHS/ASC structures, structural dynamics & materials conference, Austin, Texas, 2005.
- [56] Thomas J, Dowell EH, Hall K, Denegri C. Modelling limit cycle oscillation behavior of the F-16 fighter using a harmonic balance approach. In: Proceedings of the 45th AIAA/ASME/ASCE/AHS/ASC structures, structural dynamics & materials conference, Palm Springs, California, 2004.
- [57] Liu L, Dowell EH, Thomas J. Higher order harmonic balance analysis for limit cycle oscillations in an airfoil with cubic restoring forces. In: Proceedings of the 46th AIAA/ASME/ASCE/AHS/ASC structures, structural dynamics & materials conference, Austin, Texas, 2005.
- [58] Baldelli D, Chen P, Liu D, Lind R, Brenner M. Nonlinear aeroelastic modeling by block-oriented identification. In: Proceedings of the 45th AIAA/ASME/ASCE/AHS/ASC structures, structural dynamics & materials conference, Palm Springs, California, 2004.
- [59] Richards C, Brenner M, Singh R. Identification of a nonlinear aeroelastic aircraft wing model. In: Proceedings of the 45th AIAA/ASME/ASCE/AHS/ASC structures, structural dynamics & materials conference, Palm Springs, California, 2004.
- [60] Popescu C, Wong Y, Lee B. System identification for nonlinear aeroelastic models. In: Proceedings of the 46th AIAA/ASME/ASCE/AHS/ASC structures, structural dynamics & materials conference, Austin, Texas, 2005.
- [61] Lind R, Prazenica R, Brenner M. Identifying parameter-dependent Volterra kernels to predict aeroelastic instabilities. In: Proceedings of the 45th AIAA/ASME/ASCE/AHS/ASC structures, structural dynamics & materials conference, Palm Springs, California, 2004.
- [62] Chabalko C, Hajj M, Silva W. Time/frequency analysis of the flutter of the flexible HSCT semispan model. In: Proceedings of the 45th AIAA/ASME/ASCE/AHS/ASC structures, structural dynamics & materials conference, Palm Springs, California, 2004.
- [63] Raveh DE. Reduced-order models for nonlinear unsteady aerodynamics. *AIAA J* 2001;39(8):1417–29.
- [64] Silva WA. Discrete-time linear and nonlinear aerodynamic impulse responses for efficient CFD analyses. PhD thesis, College of William and Mary, Virginia, USA; 1997.
- [65] Munteanu S, Rajadas J, Nam C, Chathopadhyay A. An efficient approach for solving nonlinear aeroelastic phenomenon using reduced-order modelling. In: Proceedings of the 45th AIAA/ASME/ASCE/AHS/ASC structures, structural dynamics & materials conference, Palm Springs, California, 2004.
- [66] Munteanu S, Rajadas J, Nam C, Chathopadhyay A. Reduced-order-model approach for aeroelastic analysis involving aerodynamic and structural nonlinearities. *AIAA J* 2005;43(3):560–71.
- [67] Prazenica AKR, Reisenthel P, Brenner M. Volterra kernel identification and extrapolation for the F/A-18 active aeroelastic wing. In: Proceedings of the 45th AIAA/ASME/ASCE/AHS/ASC structures, structural dynamics & materials conference, Palm Springs, California, 2004.
- [68] Pettit C, Beran P. Polynomial chaos expansion applied to airfoil limit cycle oscillations. In: Proceedings of the 45th AIAA/ASME/ASCE/AHS/ASC structures, structural dynamics & materials conference, Palm Springs, California, 2004.
- [69] Beran P, Pettit C. A direct method for quantifying limit-cycle oscillation response characteristics in the presence of uncertainties. In: Proceedings of the 45th AIAA/ASME/ASCE/AHS/ASC structures, structural dynamics & materials conference, Palm Springs, California, 2004.
- [70] Pettit C, Beran P. Wiener-Haar expansion of airfoil limit cycle oscillations. In: Proceedings of the 46th AIAA/ASME/ASCE/AHS/ASC structures, structural dynamics & materials conference, Austin, Texas, 2005.
- [71] Attar P, Dowell EH. A stochastic analysis of the limit cycle behavior of a nonlinear aeroelastic model using the response surface method. In: Proceedings of the 46th AIAA/ASME/ASCE/AHS/ASC structures, structural dynamics & materials conference, Austin, Texas, 2005.
- [72] Marzocca P, Librescu L, Kim D-H, Lee I, Coppotelli G. Unified analytical/CFD approach of linear/nonlinear aeroelastic response and flutter via aerodynamic indicial function concept. In: International forum on aeroelasticity and structural dynamics, Munich, Germany, 2005.
- [73] Marzocca P, Librescu L, Kim D, Lee I. Supersonic flutter and LCO of airfoils via CFD/analytical combined approach. In: Proceedings of the 46th AIAA/ASME/ASCE/AHS/ASC structures, structural dynamics & materials conference, Austin, Texas, 2005.
- [74] Kim D, Lee I, Marzocca P. Linear/nonlinear aeroelastic computation of 2-D lifting surfaces using a combined CFD/analytical approach. In: Proceedings of the 45th AIAA/ASME/ASCE/AHS/ASC structures, structural dynamics & materials conference, Palm Springs, California, 2004.
- [75] Rodden WP, Harder RL, Bellinger ED. Aeroelastic additions to NASTRAN. Technical Report Contractor Report 3094, NASA; 1979.
- [76] Rodden WP, Johnson EH. MSC/NASTRAN aeroelastic analysis user's guide, version 68. Technical Report, The MacNeal Schwendler Corporation; 2004.

- [77] Lucia DJ, Beran PS, Silva WA. Reduced-order modelling: new approaches for computational physics. *Progr Aerosp Sci* 2004;40(1–2):51–117.
- [78] Allwright S. MDO process and specification for the primary sensitivity study. Technical Report D.2.4.S., MDO/SPEC/BAE/SA960430; 1996.
- [79] Allwright S. Reference aircraft performance and primary sensitivities. Technical Report D.3.12.R., MDO/TR/BAE/SA970530/1; 1997.
- [80] Girodroux-Lavigne P, Grisval JP, Guillemot S, Henshaw M, Karlsson A, Selmin V et al. Comparative study of advanced fluid-structure interaction methods in the case of a highly flexible wing (results from the UNSI program). In: International forum on aeroelasticity and structural dynamics, Madrid, Spain, 2001.
- [81] Girodroux-Lavigne P, Grisval JP, Guillemot S, Henshaw M, Karlsson A, Selmin V, et al. Comparison of static ad dynamic fluid–structure interaction solutions in the case of a highly flexible modern transport aircraft wing. *J Aerosp Sci Technol* 2003;7:121–33.
- [82] Yates EC. AGARD standard aeroelastics configurations for dynamic response 1: Wing 445.6. Technical Report 765, AGARD; 1988.
- [83] Bennett RM, Scott RC, Wieseman CD. Test cases for the benchmark active controls model: spoiler and control surface oscillations and flutter. Technical Report RTO-TR-26 AC/323(AVT)TP/19, 8E, RTO; 2000.
- [84] Scott RC, Hoadley ST, Wieseman CD, Durham MH. The benchmark active controls technology model aerodynamic data. In: 35th aerospace sciences meeting and exhibit. Reno, NV: AIAA; 1997.
- [85] Waszak MR. Modelling the benchmark active control technology wind-tunnel model for application to flutter suppression. In: Atmospheric flight mechanics conference. San Diego, CA: AIAA; 1996.
- [86] Tamayama M, Saitoh K, Matsushita J, Nakamichi NAL. SST arrow wing with oscillating flap. In: Verification and validation data for computational unsteady aerodynamics. RTO Technical Report-26; 2000. p. 295–318.
- [87] Tamayama M, Miwa H, Nakamichi J. Unsteady aerodynamics measurements on an elastic wing model of SST. In: 35th Aerosp Sci Meeting and Exhibit, Reno, NV, 1997.
- [88] Tamayama M, Saitoh K, Matsushita H. Measurements of unsteady pressure distributions and dynamic deformations on an SST elastic wing model. In: CEAS international forum on aeroelasticity and structural dynamics, vol. 3, Rome, Italy, 1997. p. 231–8.
- [89] Chen PC, Jadic I. Interfacing of fluid and structural models via innovative structural boundary element method. *AIAA J* 1998;36(2):282–7.
- [90] Chen PC, Hill LR. A three dimensional boundary element method for CFD/CSD grid interfacing. In: 40th AIAA/ASME/ASCE/AHS/ASC structures, structural dynamics, and materials conference and exhibit, vol. 1, St. Louis, MO, 1999.
- [91] Jones DP. Force transfer in aeroelastic calculations. Technical Report, Department of Aerospace Engineering Report AE046, University of Bristol; 2002.
- [92] Smith MJ, Hodges DH, Cesnik CES. An evaluation of computational algorithms to interface between CFD and CSD methodologies. Technical Report WL-TR-3055, Wright Laboratory; November 1995.
- [93] Cebral JR, Lohner R. Conservative load projection and tracking for fluid–structure problems. *AIAA J* 1997;35(9):687–92.
- [94] Maman N, Farhat C. Matching fluid and structure meshes for aeroelastic computations: a parallel approach. *Comput Struct* 1995;54(4):779–85.
- [95] Jiao X, Heath MT. Common-refinement-based data transfer between non-matching meshes in multiphysics simulations. *Int J Numer Methods Eng* 2004;61:2402–27.
- [96] Badcock KJ, Richards BE, Woodgate MA. Elements of computational fluid dynamics on block structured grids using implicit solvers. *Progr Aerosp Sci* 2000;36:351–92.
- [97] Haase W, Brandsma E, Elsholz E, Leschziner M, Schwaborn D, editors. Notes on numerical fluid mechanics, vol. 42. Friedr, Vieweg & Sohn; 1992.
- [98] Vlachos N. Aero-structural coupling in transonic flow; comparison of strong and weak coupling schemes. Technical Report DERA/ASF/3662U-AERO.RK5615, DERA; 1999.
- [99] Taylor NV, Allen CB, Gaitonde AL, Jones DP, Hill GFJ. Investigation of structural modelling methods for aeroelastic calculations. In: Proceedings AIAA 22nd applied aerodynamics conference, Rhode Island, 2004.
- [101] Goura GSL. Time marching analysis of flutter using computational fluid dynamics. PhD thesis, University of Glasgow, Glasgow, UK; November 2001.
- [102] Woodgate MA, Badcock KJ, Rampurawala AM, Richards BE, Nardini C, Henshaw MJ. Aeroelastic calculations for the hawk aircraft using the Euler equations. *J Aircr* 2005;40(4):1005–12.
- [103] Goura GSL, Badcock KJ, Woodgate MA, Richards BE. A data-exchange method for fluid-structure interaction problems. *Aeronaut J* 2001; 199–214.
- [104] Rampurawala AM. An assessment of inter-grid transformation for a whole aircraft. Master's thesis, University of Glasgow, Glasgow, UK; 2002.
- [105] Duchon J. Splines minimising rotation-invariant semi-norms in sobolev spaces. Constructive theory of functions of several variables, Germany: Springer; 1976.
- [106] Frank R. Scattered data interpolation: test of some methods. *J Math Comput* 1982;38:181–99.
- [107] Gaitonde AL, Fiddes SP. A three-dimensional moving mesh method for the calculation of unsteady transonic flows. *Aeronaut J* 1995;99(984):150–60.
- [108] Gaitonde AL. A dual time method for the solution of the 2D unsteady Navier–Stokes equations on structured moving meshes. In: Proceedings of the 13th AIAA applied aerodynamics conference, San Diego, USA, 1995.
- [109] Batina JT. Unsteady Euler aerofoil solutions using unstructured dynamic meshes. *AIAA J* 1990;28(8):1381–1388.
- [110] Jones DP, Gaitonde AL, Fiddes SP. Moving mesh generation for deforming complex configurations using a multiblock method. In: Comput Fluid Dyn J—Japan Society of CFD (Special Issue).: The proceedings (II) of ISCFD'99, vol. 9, Bremen, 1999. p. 287–96.
- [111] Press WH, Teukolsky SA, Vetterling WT, Flannery BP. Numerical recipes in fortran: the art of scientific computing. 2nd ed. Cambridge, MA: Cambridge University Press; 1992.
- [112] Lee-Rausch EM, Batina JT. Wing flutter boundary prediction using unsteady Euler aerodynamic method. *J Aircr* 1995;32(2):416–22.

- [113] Gordnier RE, Melville RB. Transonic flutter simulations using an implicit aeroelastic solver. *J Aircr* 2000;37(5):872–9.
- [114] Fenwick CL. Consideration of control surfaces in time-domain aeroelastic simulations. Technical Report, Department of Aerospace Engineering Report AE045, University of Bristol; 2003.
- [115] Rampurawala AM. Aeroelastic analysis of aircraft with control surfaces using CFD. PhD thesis, University of Glasgow, Glasgow, UK; June 2006.
- [116] Benek JA, Steger JL, Dougherty FC. A flexible grid embedding technique with application to the Euler equations. In: 6th computational fluid dynamics conference, 1983.
- [117] Rampurawala AM, Badcock KJ. Response of a flexible arrow wing in transonic flow to flap motions. *J Aircr*, accepted for publication.
- [118] Rampurawala AM, Badcock KJ. Treatment of forced flap motions for aeroelastic simulations of an arrow wing. In: 23rd AIAA applied aerodynamics conference, Toronto, Ontario, 2005.
- [119] Rampurawala AM, Badcock KJ. Buzz prediction on an arrow wing configuration using computational fluid dynamics. *Aerosp Sci Technol*, submitted for publication.
- [120] Rampurawala AM, Badcock KJ. Buzz simulation for a supersonic transport configuration. In: International forum on aeroelasticity and structural dynamics, Munich, Germany, 2005.
- [121] Tang HS, Zhou T. On nonconservative algorithms for grid interfaces. *SIAM J Numer Anal* 1999;37(1):173–93.
- [122] Berger MJ. On conservation at grid interfaces. *SIAM J Numer Anal* 1987;24(5):967–84.
- [123] Rai MM. A relaxation approach to patched-grid calculations with the Euler equations. In: 23rd Aerosp Sci Meeting, Reno, NV, 1985.
- [124] Rai MM. A conservative treatment of zonal boundaries for Euler equation calculations. *J Comput Phys* 1986;62(2):472–503.
- [125] Lerat A, Wu Z. Stable conservative multi-domain treatments for implicit Euler solvers. *J Comput Phys* 1996;123:45–64.
- [126] Bohbot J, Grondin G, Corjon A, Darracq D. A parallel multigrid conservative patched/sliding mesh algorithm for turbulent flow computation of 3D complex aircraft configurations. In: 39th Aerospace Sciences Meeting and Exhibit, Reno, NV, 2001.
- [127] Fenwick CL, Allen CB. Development and validation of sliding and non-matching grid technology for control surface representation. *Proc inst mech eng, Part G: J Aerosp Eng* 2006;220(4):299–315.
- [128] Fenwick CL. Development of sliding grid methods for unsteady CFD with application to control surfaces in aeroservoelastic simulations. PhD thesis, University of Bristol, Bristol, UK; 2006.
- [129] Taylor NV, Gaitonde AL, Jones DP, Allen CB. Modelling the BACT wing through linear and coupled CFD-CSD moving mesh analysis. *J Aircr*, 2007, to appear.
- [130] Taylor NV, Allen CB, Gaitonde AL, Jones DP. A comparison of linear and moving mesh CFD-CSD aeroelastic modelling of the BACT wing. In: Proceedings of 24th applied aerodynamics conference, San Francisco, 2006.
- [131] Lee BHK, Price SJ, Wong YS. Nonlinear aeroelastic analysis of airfoils: bifurcation and chaos. *Progr Aerosp Sci* 1999;35:205–334.
- [132] Hancock GJ, Wright JR, Simpson A. On the teaching of the principle of wing flexure-torsion flutter, *Aeronaut J* 1985; 285–305.
- [133] Dimitriadis G. Investigation of nonlinear aeroelastic systems. PhD thesis, University of Manchester, Manchester, UK; 1999.
- [134] Juang J-N, Pappa RS. An eigensystem realization algorithm for modal parameter identification and model reduction. *J Guidance Control Dyn* 1985;8(5):620–7.
- [135] Ho BL, Kalman RE. Effective construction of linear state-variable models from input/output functions. *Regelungstechnik* 1966;12(14):545–8.
- [136] Antoulas AC, Sorensen DC, Gugercin S. A survey of model reduction methods for large systems. *Contemporary mathematics*. AMS Publications, vol. 280, 2001, p. 193–219.
- [137] Grimme EJ. Krylov projection methods for model reduction PhD thesis, University of Illinois, Urbana-Champaign, Illinois; 1997.
- [138] Willcox KE. Reduced-order aerodynamic models for aeroelastic control of turbomachines. PhD thesis, MIT; 2000.
- [139] Chen J, Kang S, Liu JZC, Schutt-Aine JE. Reduced-order modelling of weakly non-linear MEMS devices with Taylor-series expansion and Arnoldi approach. *J Microelectromech Systems* 2004;13(3):441–51.
- [140] Gaitonde AL, Jones DP. System identification and reduction from the pulse responses of a linearised Euler scheme. In: CEAS aerospace aerodynamics research conference, Cambridge, UK, 2002.
- [141] Gaitonde AL, Jones DP. Reduced order state-space models from the pulse responses of a linearised CFD scheme. *Int J Numer Meth Fluids* 2003;42(6):581–606.
- [142] Roberts I, Gaitonde AL, Jones DP, Lieven NAJ. Identification of limit-cycles for piecewise nonlinear aeroelastic systems in transonic regimes. In: CEAS aerospace aerodynamics research conference, Cambridge, UK; 2002.
- [143] Doetsch G. Guide to the application of the Laplace and Z-transforms. 2nd ed. New York: Van Nostrand Reinhold Company; 1971.
- [144] McGillem CD, Cooper GR. Continuous and discrete signal and system analysis. CBS Publishing Japan Ltd; 1984.
- [145] Aplevich JD. The essentials of linear state-space systems. New York: Wiley; 2000.
- [146] Morton SA, Beran PS. Hopf-bifurcation analysis of airfoil flutter at transonic speeds. *J Aircr* 1999;36:421–9.
- [147] Badcock KJ, Woodgate M, Richards BE. The application of sparse matrix techniques for the CFD based aeroelastic bifurcation analysis of a symmetric aerofoil. *AIAA J* 2004;42(5):883–92.
- [148] Woodgate MA, Badcock KJ. Aeroelastic damping model derived from discrete Euler equations. *AIAA J* 2006;44(11):2601–11.
- [149] Golub GH, Loan CFV. Matrix computations. Baltimore, MD: The John Hopkins University Press; 1996.
- [150] Woodgate MA, Badcock KJ. Fast prediction of transonic aeroelastic stability and limit cycles. *AIAA J* 2007;45(6):1370–1381.

- [151] Badcock KJ, Woodgate MA, Richards BE. Direct aeroelastic bifurcation analysis of a symmetric wing based on the Euler equations. *J Aircr* 2005;42(3):731–7.
- [152] Yang ZC, Zhao LC. Analysis of limit cycle flutter of an airfoil in incompressible flow. *J Sound Vibr* 1988;123(1):1–13.
- [153] Price SJ, Alighanbari H, Lee BHK. The aeroelastic behaviour of a two-dimensional airfoil with bilinear and cubic structural nonlinearities. *J Fluids Struct* 1995;9:175–93.
- [154] Lee BHK, Liu L, Chung KW. Airfoil motion in subsonic flow with strong cubic restoring forces. *J Sound Vib* 2005; 281:699–717.
- [155] Lee CL. An iterative procedure for nonlinear flutter analysis. *AIAA J* 1986;24(3):833–40.
- [156] Thomas JP, Dowell EH, Hall KC. Modelling viscous transonic limit-cycle oscillation behavior using a harmonic balance approach. *J Aircr* 2004;41(6):1266–74.
- [157] Kholodar DB, Dowell EH, Thomas JP, Hall KC. Limit-cycle oscillations of a typical airfoil in transonic flow. *J Aircr* 2004;41(5):1067–72.
- [158] Attar PJ, Dowell EH, White JR. Modelling delta wing limit-cycle oscillations using a high-fidelity structural model. *J Aircr* 2005;42(5):1209–17.
- [159] Kim D-H, Lee I, Marzocca P, Librescu L, Schober S. Nonlinear aeroelastic analysis of an airfoil using CFD-based indicial approach. *J Aircr* 2005;42(5):1340–3.
- [160] Dimitriadis G, Cooper JE. Characterization of the behaviour of a simple aeroservoelastic system with control nonlinearities. *J Fluids Struct* 2000;14(8):1173–93.
- [161] Patil MJ, Hodges DH, Cesnik CES. Nonlinear aeroelasticity and flight dynamics of high-altitude long-endurance aircraft. *J Aircr* 2001;38(1):88–94.
- [162] Ding Q, Cooper JE, Leung AYT. Application of an improved cell mapping method to bilinear stiffness aeroelastic systems. *J Fluids Struct* 2005;20(1):35–49.
- [163] Raghothama A, Narayanan S. Non-linear dynamics of a two-dimensional airfoil by incremental harmonic balance method. *J Sound Vibr* 1999;226(3):493–517.
- [164] Liu L, Wong YS, Lee BHK. Application of the centre manifold theory in non-linear aeroelasticity. *J Sound Vibr* 1999;234(4):641–59.
- [165] Vio GA, Cooper JE. Limit cycle oscillation prediction for aeroelastic systems with discrete bilinear stiffness. *Int J Appl Math Mech* 2005;3:100–19.
- [166] Roberts I, Jones DP, Lieven NAJ, Bernado MD, Champneys AR. Analysis of piecewise linear aeroelastic systems using numerical continuation. *Proc Inst Mech Eng Part G: J Aerosp Eng* 2002;216(1):1–11.
- [167] Dimitriadis G, Vio G, Cooper J. Stability and LCO amplitude prediction for aeroelastic systems with structural and aerodynamic nonlinearities using numerical continuation. In: AVT symposium on flow-induced unsteady loads and the impact on military applications, Budapest, Hungary; 2005.
- [168] Doedel EJ, Champneys AR, Fairgrieve TF, Kuznetsov YA. Continuation and bifurcation software for ordinary differential equations (with HomCont): user's guide: Technical Report, Concordia University, Montreal, Canada; 2000.
- [169] Govaerts W, Dhooge A, Kuznetsov YA. MATCONT: a Matlab package for numerical bifurcation of ODEs. *ACM Trans Math Software* 2003;29(2):141–64.
- [170] Beran PS, Strganac TW, Kim K, Nichkawde C. Studies of store-induced limit-cycle oscillations using a model with full system nonlinearities. *Nonlinear Dyn* 2004;37:323–39.
- [171] Dimitriadis G. Bifurcation analysis for subsonic nonlinear aircraft using numerical continuation, *J Aircr*, 2006; Submitted for publication.
- [172] Kuznetsov YA, Levitin VV. CONTENT: integrated environment for analysis of dynamical systems. Technical Report, CWI, Amsterdam; 1997.
- [173] Doedel E, Keller HB, Kernevez JP. Numerical analysis and control of bifurcation problems (i) bifurcation in finite dimensions. *Int J Bifurcation and Chaos* 1991;1(3): 493–520.
- [174] Beyn WJ, Champneys A, Doedel E, Govaerts W, Kuznetsov YA, Sandstede B. Numerical continuation and computation of normal forms. In: Fiedler B, editor. *Handbook of dynamical systems*, vol. 2. Amsterdam: Elsevier; 2002.
- [175] Eversman W, Tewari A. Consistent rational-function approximation for unsteady aerodynamics. *J Aircr* 1991; 28(9):545–52.
- [176] Roger KL. Airplane math modelling methods for active control design. Technical Report AGARD-CP-228, AGARD; 1977.
- [177] Snyder RD, Beran PS, Zweber JV. Predictions of store-induced limit cycle oscillations using Euler and Navier–Stokes fluid dynamics. In: Proceedings of the 44th AIAA/ASME/ASCE/AHS/ASC structures, structural dynamics & materials conference, Norfolk, Virginia; 2003.
- [178] Knot NS, Beran PS, Zweber JV, Eatsep FE. Influence of tip store mass location on wing limit-cycle oscillation. In: Proceedings of the 44th AIAA/ASME/ASCE/AHS/ASC structures, structural dynamics & materials conference, Norfolk, Virginia; 2003.
- [179] Parker GH, Maple RC, Berans PS. Analysis of store effects on limit cycle oscillation. In: Proc 47th AIAA/ASME/ASCE/AHS/ASC structures, structural dynamics & materials conference, Newport, Rhode Island; 2006.
- [180] Nissim E, Gilyard GB. Method for experimental determination of flutter speed by parameter identification. Technical Report, Technical Paper 2923, NASA; June 1989.
- [181] Lisandrin P, Carpentieri G, van Tooren M. Open issues in system identification of CFD based aerodynamic models for aeroelastic applications. In: International forum on aeroelasticity and structural dynamics, Munich, Germany, 2005.
- [182] Rampurawala A, Badcock K. Treatment of complex configurations for flutter calculations. In: Proceedings of the 47th AIAA/ASME/ASCE/AHS/ASC structures, structural dynamics and materials conference, Newport, Rhode Island; 2006.
- [183] Fuglsang DF, Brase LO, Agarwal S. A numerical study of control surface buzz using computational fluid dynamics methods. In: 10th AIAA applied aerodynamics conference, Palo Alto, CA; 1992.
- [184] Haase W, Selmin V, Winzell B., editors., Notes on numerical fluid and multidisciplinary design. *Progress in computational flow–structure interaction*, Springer, Berlin; 2003.